UC Riverside
UC Riverside Electronic Theses and Dissertations

Title

Carbon Nanomaterial-Based Chemiresistive Biosensors for Detection of Secretory Protein Biomarkers of Citrus Greening Disease

Permalink

https://escholarship.org/uc/item/7bj3x2qh

Author

Tran, Thien-Toan Huu

Publication Date

2018

Peer reviewed|Thesis/dissertation

UNIVERSITY OF CALIFORNIA
RIVERSIDE

Carbon Nanomaterial-Based Chemiresistive Biosensors for Detection of Secretory
Protein Biomarkers of Citrus Greening Disease

A Dissertation submitted in partial satisfaction
of the requirements for the degree of

Doctor of Philosophy

in

Bioengineering

by

Thien-Toan Huu Tran

September 2018

Dissertation Committee:
       Dr. Ashok Mulchandani, Chairperson
       Dr. Tsutsui Hideaki
       Dr. Jin Nam

The Dissertation of Thien-Toan Huu Tran is approved:

_____

_____

_____

Committee Chairperson

University of California, Riverside

ACKNOWLEDGEMENTS

Saucedo, Daniel Wasik, Trupti-Terse Thakoor, Mohammed Sedki, Yu Shen. You have contributed greatly to my training and personal development. Thank you to Liem Pham, Tung Pham, and Pankaj Ramnani who have been so kind in their support and uplifting attitudes as we made our PhD. journeys together.

I would like to also thank all the dedicated undergraduate student volunteers who have worked closely with me throughout the years and have been of tremendous help, especially Linh Nguyen, Brittney Shaver, Sean Esqueda, Ema Alatini, Joseph Baladad, Anthony Ramirez, and Josias Ochoa. You all have inspired me to become a better mentor, TA, and researcher.

Finally, I want to say thanks my family, relatives, and girlfriend, Mai Thuy Nguyen, for all the support and motivation they have shown throughout the years. I am forever grateful for the unconditional support and love from you. To my dear Mom and Grandpa, even though you are no longer here, I will always be grateful for you and remember the important life lessons you have taught me that have kept me grounded. I would not be here without you.

DEDICATION

To my family, friends, and loved ones

ABSTRACT OF THE DISSERTATION

Carbon Nanomaterial-Based Chemiresistive Biosensors for Detection of Secretory
Protein Biomarkers of Citrus Greening Disease

by

Thien-Toan Huu Tran

Doctor of Philosophy, Graduate Program in Bioengineering
University of California, Riverside, September 2018
Professor Ashok Mulchandani, Chairperson

Citrus greening disease, also known as Huanglongbing (HLB), is posing a
worldwide threat to the multi-billion dollars citrus industry. Currently, there are no cures
for infected plants while containment of the spread of disease is heavily dependent on early
detection of infected hosts for quarantine. The pathogen responsible for causing the disease
is the bacteria *Candidatus* Liberibacter asiaticus (*C*Las). Thus, it is imperative that disease
management strategies address current demands for accurate, timely, and robust disease
detection and diagnosis minimize the spread of disease. By adopting a novel detection
strategy targeting a recently discovered secreted protein biomarker, SDE1, which is unique
to *C*Las, we hope to overcome the challenges faced by current detection methods, such as
nucleic acid-based and symptom-based which have been found prone to false negatives

and mis-diagnoses, respectively. To do this, we have worked to procure and characterize the antibodies specific for the novel HLB biomarker. In the process of characterizing the anti-SDE1 antibodies, we have also developed a specific and sensitive enzyme-linked immunosorbent assay (ELISA) for high-throughput and point-of-laboratory analysis of citrus plant samples. With the final goal of using the anti-SDE1 antibodies to develop sensitive, facile, and specific HLB detection method, we have integrated these antibodies into nanoscale electrical biosensor platforms. Using the novel semiconducting carbon nanomaterials, reduced graphene oxide (RGO) and single-walled carbon nanotubes (SWNTs), as the electrical transducer element for our biosensors, we have developed chemiresistive biosensors that demonstrate specificity and sensitivity to the SDE1 biomarker in simple phosphate buffer and in plant extracts.

Table of Contents

List of Figures

Chapter 1

Introduction: Carbon Nanomaterial-Based Electronic Biosensor Platforms for Detection of Secretory Protein Biomarkers of Citrus Greening Disease

1.1 Overview and Significance

Citrus greening disease, also known as Huanglongbing (HLB) disease, is posing a worldwide threat to the multi-billions dollar industry [1]. The disease leads to symptoms of rapid tree decline, where fruit production by the infected tree is significantly affected. Some symptoms include small, poorly colored, lopsided and off-tasting fruit, and mottled leaves shown in figure 1.1. The pathogen responsible for HLB is the bacterium *Candidatus* Liberibacter which resides in the phloem of infected plants [1–3]. The primary mode of transmission of the pathogenic agent is through insect vectors, predominantly by the Asian and African citrus psyllids, *Diaphorina citri* and *Trioza erytreae*, respectively. There are different strains of the bacteria *Candidatus* Liberibacter: asiaticus, africanus, and americanus. The various strains are not necessarily constrained to the geographical regions based on their respective names. However, the focus of our research will be on the specific strain Candidatus liberbacter asiaticus (*C*Las), which is the most rampantly spread strain in Asia and in North America[1,4].
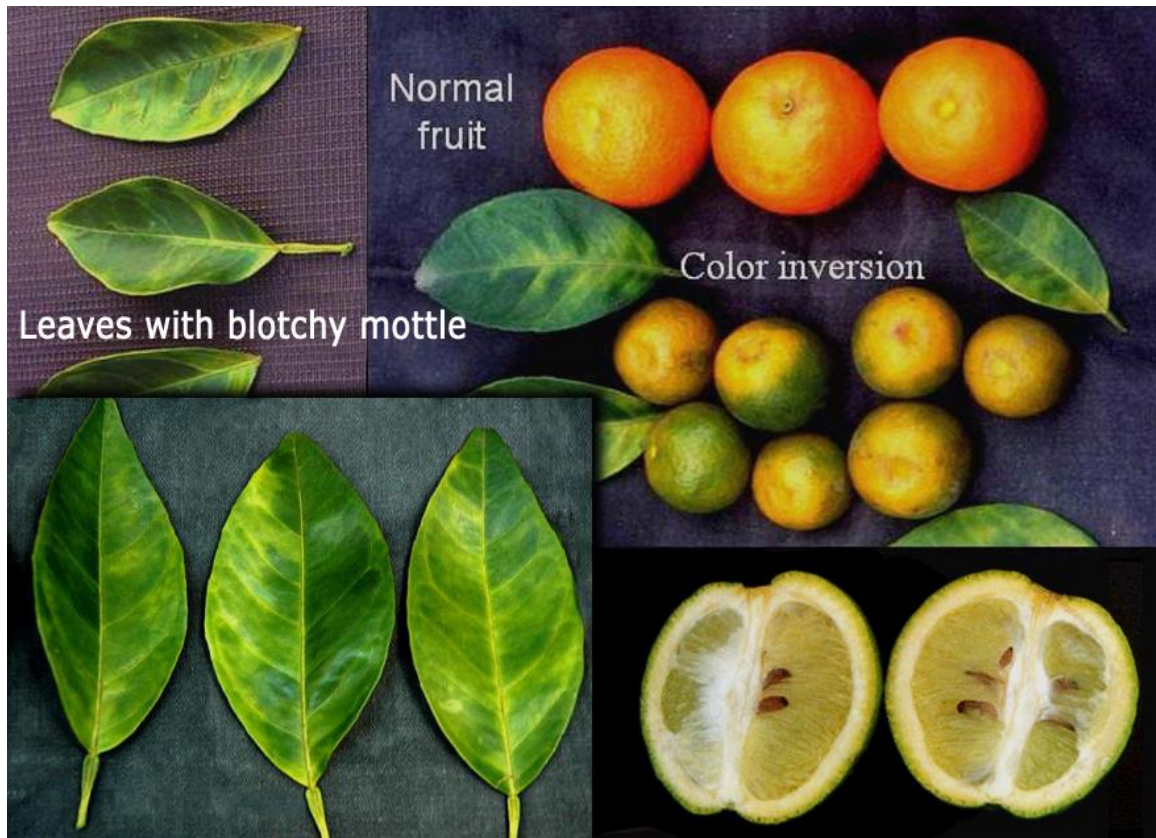
Figure 1.1: *HLB disease symptoms of rapid tree decline, where fruit production by the infected tree is significantly affected. Symptoms include small, poorly colored, lopsided and off-tasting fruit, and mottled leaves*[5].

As known to date, there are no cures for trees affected with HLB disease; therefore, management of the spread of the disease is focused on removal of the pathogens via eradication of infected trees and vectors[1,3]. Thus, timely and accurate detection of infected plants is crucial for disease management; however, detection methods based on disease symptoms and nucleic-acid assays remain unsuccessful. Symptoms-based and qualitative diagnosis of infected plants lack accuracy due to variable latency of symptoms and due to similarities of symptoms with other citrus diseases and nutrient deficiency[3]. Assays for

detection of nucleic acid-based biomarkers of *Ca*. Liberibacter suffer from high rates of false negatives due to uneven distribution of the pathogen in infected plants[2,6]. Additionally, nucleic acid-based assays suffer from complex sample preparation requirement, high costs, time-consuming processes, making these tools prohibitive for disease management, especially when multiple samples need to be tested from one tree[1]. Therefore, the detection of secreted protein-based biomarkers for the pathogen addresses the performance requirements for accuracy, speed, robustness, and portability. These secreted proteins evenly and systematically distribute throughout the infected trees and consequently eliminate the need for multiple sampling sites per tree. Uniform distribution of the biomarker further affords reliable and selective diagnosis of infected plants by reducing false negatives due to sampling challenges[4].

Since the first carbon nanotube-based field-effect transistor (CNT-FET) devices reported in 1998, these carbon nanomaterials (CNMs), such as carbon nanotubes, graphene oxide, and graphene have attracted considerable interest from the biosensor research community due to their potentials for improved sensitivity, biocompatibility, portability, and even label-free sensing[7–9]. This research will focus on utilizing the chemiresistor biosensor architecture, which is a variation of the FET device architecture and operates under those same sensing mechanims[10–12]. The design, fabrication, and operations will be reviewed in Chapter 2. Thus, using such a biomarker SDE1, discovered by our collaborator, Dr. Wenbo Ma, who also have generated custom polyclonal antibodies for immunoassay applications, we further used these anti-SDE1 antibodies in an electrical biosensor based on carbon nanomaterials as bioreceptors for specific binding to SDE1 biomarkers. Various

CNMs are investigated for use in our devices, which include semiconducting single-walled carbon nanotubes (SWNTs) and reduced graphene oxide (RGO) to develop a sensitive, facile, and robust detection system for HLB biomarkers (figure 1.2).
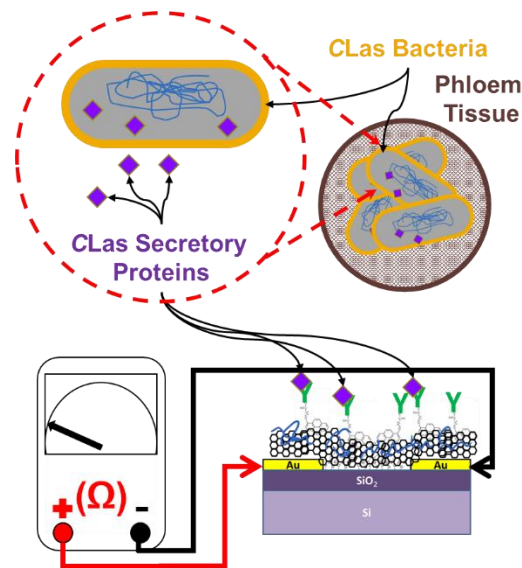
Figure 1.2*: Conceptual drawing for an HLB detection system with a chemiresistive sensor for CLas secretory protein biomarkers.*

1.2 Scope of this Research

The **goal** of this work is to develop a carbon nanomaterial-based chemiresistive biosensor for detection of an effector-based secretory protein biomarker for the detection of HLB disease through the following specific aims:

- **Specific Aim 1**: Antibody Generation, Purification, and Evaluation.

- **Specific Aim 2**: Integration of antigen and antibody reagents into SWNT/RGO based chemiresistive biosensor with device characterization and device optimization using purified antigens in buffer.

- **Specific Aim 3**: Testing and optimization of biosensors with artificially spiked plant samples and infected plant samples.

This research encompassed multiple broad aspects of biosensor development. As reported in Chapter 3, **Aim 1** focused specifically on the procurement of the antibodies for the biomarker and utilization of an independent enzyme-linked immunosorbent assay platform to further study and validate the antibody-antigen pair. We collaborated with Dr. Wenbo Ma's lab (Plant Pathology, UCR) to obtain and characterize the antigen and antisera reagents, and to procure the samples needed for Aim 1. As discussed in Chapters 4 to 5, **Aims 2** and **3** focused on integrating the antibodies obtained from Aim 1 to develop and optimize our CNM-based chemiresistive biosensor system on silicon substrates for detection of the antigen in simple and complex samples.

1.3 References

1.   Gottwald, T. R. Current Epidemiological Understanding of Citrus Huanglongbing [*]. *Annual Review of Phytopathology* **48,** 119–139 (2010).

2.   Teixeira, D. C. *et al.* Distribution and quantification of Candidatus Liberibacter americanus, agent of huanglongbing disease of citrus in São Paulo State, Brasil, in leaves of an affected sweet orange tree as determined by PCR. *Molecular and Cellular Probes* **22,** 139–150 (2008).

3.   Bové, J. M. Huanglongbing: a destructive, newly-emerging, century-old disease of citrus. *Journal of plant pathology* 7–37 (2006).

4.   Pagliaccia, D. *et al.* A Pathogen Secreted Protein as a Detection Marker for Citrus Huanglongbing. *Frontiers in Microbiology* **8,** (2017).

5.   National Research Council (U.S.) & Committee on the Strategic Planning for the Florida Citrus Industry: Addressing Citrus Greening Disease (Huanglongbing). *Strategic planning for the Florida citrus industry addressing citrus greening disease*. (National Academies Press, 2010).

6.   Irey, M. S., Gast, T. & Gottwald, T. R. Comparison of visual assessment and polymerase chain reaction assay testing to estimate the incidence of the Huanglongbing pathogen in commercial Florida citrus. in *Proc. Fla. State Hortic. Soc* **119,** 89–93 (2006).

7.   Liu, S. & Guo, X. Carbon nanomaterials field-effect-transistor-based biosensors. *NPG Asia Materials* **4,** e23 (2012).

8.   Ramnani, P., Saucedo, N. M. & Mulchandani, A. Carbon nanomaterial-based electrochemical biosensors for label-free sensing of environmental pollutants. *Chemosphere* (2015). doi:10.1016/j.chemosphere.2015.04.063

9.   Martel, R., Schmidt, T., Shea, H. R., Hertel, T. & Avouris, P. Single-and multi-wall carbon nanotube field-effect transistors. *Applied Physics Letters* **73,** 2447–2449 (1998).

10.   Tran, T.-T. & Mulchandani, A. Carbon nanotubes and graphene nano field-effect transistor-based biosensors. *TrAC Trends in Analytical Chemistry* **79,** 222–232 (2016).

11.   Das, B. K. *et al.* Single-walled carbon nanotubes chemiresistor aptasensors for small molecules: picomolar level detection of adenosine triphosphate. *Chemical Communications* **47,** 3793 (2011).

12.   García-Aljaro, C. *et al.* Carbon nanotubes-based chemiresistive biosensors for detection of microorganisms. *Biosensors and Bioelectronics* **26,** 1437–1441 (2010).

Chapter 2

Review of Carbon Nanotubes and Graphene Field-Effect Transistor-Based Biosensors

This chapter is based on Tran, T.-T. & Mulchandani, A. Carbon nanotubes and graphene nano field-effect transistor-based biosensors. *TrAC Trends in Analytical Chemistry* **79,** 222–232 (2016).

2.1 Abstract

Graphene and carbon nanotubes (CNTs) have gained major research interests as signal transducing elements in electrical biosensors for applications in biosensing of a wide range of analytes. This is mostly due to the unique physical, chemical, and electrical properties of the carbon nanomaterials. This review discusses the integration and applications of these carbon allotropes into field-effect transistor-type (FET-type) nanobiosensors. We first discuss the various properties of CNTs and graphene that make them useful and attractive for FET-type sensing, followed by methods for synthesis of CNTs and graphene nanomaterials. Additionally, the underlying sensing mechanisms of CNT- and graphene-based FET-type biosensors and the methods for fabrication of these devices are discussed. Finally, recent reports on CNT- and graphene-based FET biosensors that employed a variety of novel device configurations, fabrication techniques, and assay strategies to achieve sensitive detection of small molecules, metal ions, proteins, and nucleic acids are examined.

2.2 Introduction

Serving as analytical devices that integrate biorecognition elements with signal transduction elements to convert molecular interactions to measureable signal, biosensors are important tools for myriad fields and applications[1]. Since the first carbon nanotube field-effect transistor (CNT-FET) devices reported in 1998, carbon nanomaterials, such as carbon nanotubes and graphene, have increasingly garnered considerable interest from the biosensor research community as they offer the potential for improved sensitivity, biocompatibility, portability, and most importantly the convenience of label-free sensing[2–4]. Due to the unique chemical, electrical, and physical properties of these carbon allotropes, these nanomaterials have been of particular interest in applications for field-effect transistor-based (FET) biosensors[2,5,6].

2.3 Carbon nanomaterials:

2.3.1 Carbon Nanotubes:

2.3.1.1 Properties of CNTs:

The carbon nanotube (CNT), which can be considered a 1-dimensional (1D) allotrope of carbon, can be described as a ribbon of graphene comprising sp^2 hybridized carbon atoms with a hexagonal lattice seamlessly rolled into a cylindrical tube[7,8]. CNTs can further be categorized based on the number of graphene layers forming the cylindrical tube. Single-walled carbon nanotubes (SWCNTs) have one single layer of sp^2 carbon atoms forming the nanotube (i.e. one graphene sheet), while multi-walled carbon nanotubes (MWCNTs) consist of two or more layers of graphene sheets that form concentric

cylinders[7,9]. Depending on the synthesis method used, SWCNTs and MWCNTs have diameters that vary between 0.43-2.0 nm and up to more than 10 nm, respectively, with lengths ranging from hundreds of nanometers to hundreds of microns[10,11]. While MWCNTs have metallic electronic properties, SWCNTs can have either semiconducting or metallic electronic properties depending on their chirality and diameter [12]. Furthermore, SWCNT bandgap energies vary inversely with the diameter.

Despite sharing similar sp^2 chemical properties to 2D graphene sheets, the tube curvature of CNTs and quantum confinement in the circumferential direction result in unique electronic properties that are different from those of graphene sheets. Most relevant to FET-based biosensors are semiconducting SWCNTs which are inherently p-type semiconductors with holes as the main charge carriers. Semiconducting SWCNTs are consequently used as the semiconducting channel between the source (S) electrode and the drain (D) electrode[12,13].

1.1.1.1 Carbon Nanotube Synthesis:

There are three major methods for CNT synthesis: arc-discharge [7], laser-ablation (vaporization) [14], and catalyst-assisted vapor chemical deposition (CVD) [11]. Arc discharge synthesis of CNTs requires the use of two graphite electrodes to produce a direct current electric arc discharge in an inert environment, where the CNTs are collected in the soot material [7]. SWCNT synthesis via this method further requires a metal catalyst such as cobalt, whereas MWCNT synthesis do not require a metal catalyst [15]. CNT growth by laser ablation uses intense laser pulses to ablate a carbon target, which contains 0.5 percent

atomic concentration of cobalt and nickel, in a tube furnace at 1200°C under inert environment [11]. Both arc discharge and laser ablation methods yield high quantity and high quality CNTs. In CVD growth of CNTs, a catalyst material is heated to high temperatures in a tube furnace while the precursor hydrocarbon gas is flowed through the tube for a duration of time [16]. The hydrocarbons and catalyst material used, as well as the growth temperature are essential parameters to CVD synthesis of CNTs. Typical catalysts for this method are iron, nickel, or cobalt nanoparticles. The catalyst layer is typically patterned on a silicon substrate with an SiO_2 insulating layer [17].

Significant efforts have been underway to optimize these methods to yield defect-free crystalline CNTs and to control for the types of CNTs grown. Since these synthesis methods result in a mixture of metallic and semiconducting CNTs of varying dimensions, that have varying degrees of amorphous carbon contaminations, and may contain bundles of CNTs, isolation and purification of semiconducting SWCNTs are needed. Various purification methods have been developed as summarized by Ramnani et al. to yield the desired defect-free semiconducting SWCNTs [3]. Thanks to the development effort for scaled-up synthesis of CNTs, commercial sources for purified CNTs are readily available.

1.2 Graphene

1.2.1.1 Properties of Graphene:

Graphene is described as a planar 2-dimensional monolayer of sp^2 hybridized carbon atoms packed in a honeycomb lattice [6,18]. It is considered to be the building block for other carbon structures of other dimensionalities [6]. Graphene can be wrapped up into

zero-dimensional fullerenes, rolled up into 1D CNTs, and vertically stacked to obtain 3D graphite. Free-standing pristine graphene was first isolated and electrically characterized in 2004. Graphene is a zero-bandgap semiconductor that exhibits ambipolar electric field effect, where charge carriers are continuously tunable between holes and electrons in concentrations, n, ranging up to 10^{13}cm^{-2} with mobilities, μ, above 15,000 cm^{2}V^{-1}s^{-1} in ambient conditions [6,18,19]. This ambipolar characteristic suggests graphene's electrical sensitivity to both electron-donating and electron-withdrawing species. Furthermore, graphene's chemical stability allows the material to resist oxidation in solution under low voltage, eliminating the need for an electrical passivation layer. Graphene's high chemical stability, its unique electrical characteristics, its sub-nanoscale thickness, and large surface area suggests the nanomaterial's potential in FET-based biosensing [2].

2.1.1.1 Synthesis and Variations in Graphitic properties:

Single layer graphene was first isolated from highly oriented pyrolytic graphite (HOPG) by Novoselov and Geim in 2004 via mechanical exfoliation [18]. This was achieved by repeated peeling of π-stacked graphene layers from the bulk graphite with scotch tape [18]. Mechanical exfoliation provides higher quality graphene with minimal chemical defects, but the method suffers from low yield and lacks scalability. An alternative method for mechanical exfoliation utilizes sonication of graphite in liquid phase (in organic solvent or water) while using ionic surfactants to maintain colloidal stability of the exfoliated graphene sheets to prevent aggregation [20,21]. Centrifugation of the dispersed graphene solution allows for further separation of single layer and few-layer graphene. Liquid phase

mechanical exfoliation of graphite is scalable for higher yield of graphene that have minimal defects. Dispersed graphene solution can be conveniently used to deposit graphene flakes onto desired substrates via spray coating and drop-casting [22]. However, heat treatment of deposited graphene flakes may be required to ensure complete removal of chemical contaminants such as residual solvents or surfactants.

Epitaxial growth of graphene via thermal decomposition on the (0001) surface of single-crystal Si-6H substrate is another alternative for graphene synthesis that yields graphene with few defects [23,24]. Graphene synthesis via this method is carried out under ultrahigh vacuum and at high temperatures. Si atoms desorb from the surface of the SiC substrate while carbon atoms remain, undergoing surface rearrangement and re-bonding to form graphene layers [25]. This method yields graphene on a semi-insulating SiC substrate, which eliminates the need for the transfer of graphene onto another insulating substrate, allowing for *in situ* use. However, the intrinsic thickness of the SiC substrate only allows for top-gating and liquid-gating—and not bottom-gating—of the graphene which will be discussed later in the review [26].

One popular synthesis method for graphene is chemical vapor deposition of carbon precursor gas on metal catalysts such as copper or nickel [27,28]. CVD grown graphene enjoy minimal defects. In a tube-furnace, hydrocarbons are thermally decomposed to yield carbon atoms which undergo diffusion into the metal surface, whereby upon cooling of the metal-carbon solid solution, the carbon atoms precipitate out and segregate on catalytic metal surfaces, which form graphene. CVD graphene synthesis using copper foil is of particular interest as it yields large-area and high quality graphene films [28]. By controlling

synthesis parameters such as the type of metal catalyst, the hydrocarbons, growth temperatures, and growth duration, various qualities of graphene film can be controlled, such as the number of layers and the size of individual graphene crystals. Graphene grown on metal catalyst substrates allow for transfer of the graphene film onto the desired substrate by securing the graphene film with a polymer (e.g. poly(methyl methacrylate) or (PMMA)) support layer followed by etching away the metal layer. Wafer-scale synthesis of graphene using CVD method followed by transfer of graphene films have been previously demonstrated highlighting the method's potential for large-scale synthesis [29].

Graphene can also be synthesized through reduction of graphene oxide. For this, bulk graphite is chemically oxidized via Hummer's method to produce graphite oxide and then exfoliated by sonication to yield graphene oxide flakes [30,31]. Briefly, graphite is treated with potassium permanganate, sodium nitrate, and concentrated sulfuric acid to introduce polar oxygen-containing functional groups, such as carboxyl, epoxide, hydroxyl, and carbonyl, to introduce hydrophilicity into the layers of the material [30,32]. These highly oxygenated layers in graphite oxide can be mechanically exfoliated via sonication from the bulk material to form stable colloidal dispersions of single-layer and few-layer graphene oxide (GO) in various organic solvents and even water. Similar to mechanically exfoliated graphene solutions stabilized in surfactant, GO flakes can be applied onto the desired substrates via spray coating and drop casting. The electrical properties of exfoliated GO, however, are drastically compromised compared to pristine graphene due to the various chemical defects and loss of crystallinity. Restoration of the electrical properties requires reduction to remove chemical oxide groups and sp^3 defects while restoring sp^2 bond

structures [32]. GO can be reduced chemically using reducing agents (e.g. hydrazine), electrochemically by directly applying a reducing potential on the GO surface, or thermally at elevated temperatures [3,33]. Depending on the methods of reduction, the quality of reduced GO (rGO) will vary. Since not all defects are removed in rGO compared to pristine graphene, only partial electrical characteristics are restored depending on the extent and method of reduction. While chemical and structural defects in GO lead to insulator behavior, removal of these defects via reduction restores semiconductor properties to rGO for applications in electronics, especially for FET-based biosensing [34]. Singh et al. reported the tuning of electrical properties and bandgap of rGO by variation of temperatures for thermal reduction of GO [34].

1.3 Operating principle and sensing mechanism of FET-based biosensor using carbon nanomaterials

Field-effect transistor (FET) devices generally consist of a source, a drain, and a gate terminal where current in the semiconducting channel between the source and drain (I_D) terminals is modulated by the electric field generated by the voltage of the gate (V_G) terminal and the voltage applied between the source and drain (V_{SD}) terminals [35]. The gate voltage, V_G, can be applied via bottom-gating (back-gating) or top-gating. For SWCNT and graphene FET biosensors fabricated on SiO_2/Si substrates, the source and drain electrodes and the semiconducting channels are fabricated on top of the insulating SiO_2 layer. The degenerately doped semiconducting Si layer is then used as the bottom-gate. In FET biosensors in which assays are performed in the liquid solution on top of the device

(typically in the presence of some electrolytes), top-gating is achieved through the use of a reference electrode (e.g. Ag/AgCl) submerged into the liquid phase. Top-gating in this environment is also referred to as liquid-gating or electrolyte-gating if electrolytes are present in the solution.

Both options for back-gating and top-gating (or liquid-gating) operations allow for the observation of the ambipolar electric-field effect of a graphene FET. The back-gating operation requires measurements to be performed without any liquid on the device as well as a gate-voltage range greater than ±20 V to observe the full ambipolar electric field-effect [5,36]. Top-gating operation, however, allows for the use of phosphate buffer and require a much smaller gate-voltage range between ±0.1 V; therefore, transconductance, calculated as the slope of the I_D-V_G curve on either side of the Dirac point, is more than two orders of magnitude greater for liquid-gating operations compared to back-gating [5]. Thus, compared to back-gating, there are several advantages to liquid-gating, which allows for the direct electrical measurements of the FET biosensor without requiring removal of the solution in which analyte detection is taking place and smaller gate-voltages [5].

Depending on the type of semiconducting channel material used, modulation of the gate voltage can generate an electric field which controls the number of charge carriers (holes and electrons) in the channel, thereby affecting the conductance/resistance of the channel. Thus, biosensors employing an FET architecture and operation differ from the conventional electrochemical biosensors' three-electrode setup and operation, which consists of a working electrode, a reference electrode and a counter electrode [1,37]. Specifically, conventional three-electrode setup is utilized for measurement modes such as

15

amperometry and potentiometry which require electroactive species or biocatalytic elements to generate electrical signals, respectively [1,35]. FET-based biosensors, on the other hand, yield electrical responses upon affinity-based binding or adsorption of charged biomolecules with the semiconducting (transducer) channel which result in modulation of the number of charge carriers in the channel, thus changing the observed conductance or resistance of the channel. This characteristic highlights the potential of this biosensor architecture for label-free and affinity-based sensing. The electric field generated by charged biomolecules—in the case where SWCNT or graphene nanomaterials are used as semiconducting channels—near the interface of the semiconducting material provides gating effects on the channel that are similar to effects from applying a voltage potential is to the gate terminal.

A chemiresistor-type biosensor is a variation of the FET-biosensor configuration, which omits the gate electrode, allowing the modulation of device conductance by same mechanisms as in traditional FET-based biosensors [38,39]. Electrical characterization of chemiresistor-type biosensor is performed via I_D-V_S (or simply I-V) measurements from which resistance can be calculated. Changes in conductance or resistance of the device indicate physical and chemical alterations ofpe the surface properties of the carbon nanomaterials [40].

In both SWCNT and graphene FET-based biosensors, the single-layer surface atoms of the carbon nanomaterials are directly exposed to the environment, such that small alterations at the interface result in large changes in electrical properties of the nanomaterials [2]. This confers high sensitivity for biosensing. Upon intermolecular

interactions with the biomolecules near the interface of the carbon nanomaterials and the environment, one or more of the following mechanisms cause the observed changes in electrical properties (i.e. measured electrical responses) of SWCNT and graphene nanomaterials in FET biosensors: (1) surface charge-induced gating effect or electrostatic gating, (2) charge transfer between the biomolecules and the carbon nanomaterials, (3) charge scattering across the carbon nanomaterials, and (4) Schottky barrier modification occurring between the carbon nanomaterials and metal electrodes [2,5,41–43].

Through series of controlled experiments, Heller et al. verified that the change in conductance of semiconducting SWCNTs in FET biosensors primarily occurs via the two mechanisms, electrostatic gating and Schottky barrier modulation (Figure 2.1) [42]. Electrostatic gating occurs upon adsorption of charged biomolecules on the bulk of SWCNTs which induces doping in the SWCNTs causing shifts in Fermi level that is observed as the horizontal shifts of the I_D-V_G transfer curve along the V_G axis (Figure 2.1A). Adsorption of charged biomolecules at the contact regions modulate the metal work function which modulates the width of the Schottky barriers, and in turn affects the current across the nanotube and metal contact [41,42,44]. When analyzing device characteristics, Schottky barrier effects can be observed by the asymmetric change in slope (i.e. conductance) of the p- and n- branches of the transfer curve since the Schottky barrier height changes in opposite directions for hole (p) and electron (n) transport (Figure 2.1B) [42]. Byon and Choi have taken advantage of the Schottky barrier effect in SWCNT-FET biosensor by maximizing the Schottky contact area to increase the sensitivity of their devices for protein detection in the picomolar (pM) range [43]. Metal contacts were

fabricated to extend the contact regions of semiconducting SWCNTs and source-drain electrodes.
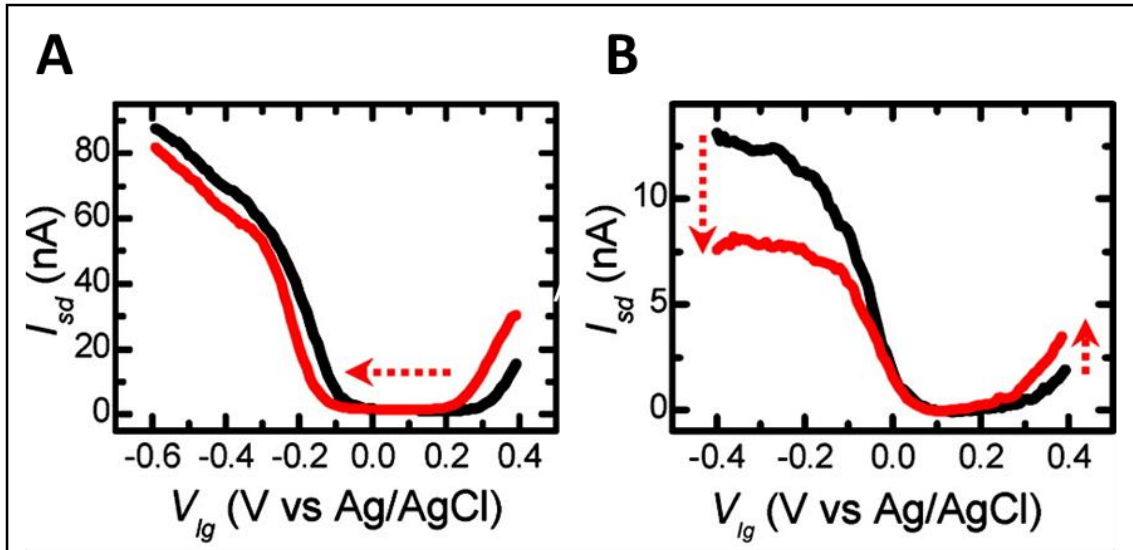
Figure 2.1: *Example of modulation of SWCNT-FET transfer characteristic due to strong electrostatic gating (A) and strong Schottky barrier effect (B). Adapted from* [42].

On the other hand, for a graphene FET device, current is primarily limited by diffusive transport in the graphene channel instead of Schottky barriers at the metal-semiconductor contacts [44]. Therefore, the gate influences conductance through changing the quantity (doping) and mobility of charge carriers. Graphically, on an I_D-V_G curve (a.k.a. transfer curve), of a graphene FET biosensor, the minimum of conductance corresponds to a minimum of charge carriers near the neutrality point, or the Dirac point (Figure 2.2A) [5,44]. To the left of the neutrality point, the majority carriers are holes, while to the right, the major charge carriers are electrons. The shift in Fermi level is observed by the lateral shift of the transfer curve—and consequently the shift in the neutrality point—along the V_G axis (Figure 2.2B) [42,44].

The mechanism of electrostatic gating effect can be observed for the case where the semiconducting SWCNT or graphene channel experiences a negative surface charge from a biomolecule or ion near, but external to the semiconducting channel at the liquid interface. The negative surface charge attracts mobile positive charges to the semiconductor-liquid interface, making the interfacial microenvironment charge-neutral. The attracted mobile positive charges consist of both positive ions from the liquid phase (in the electrical double layer) and the positive charges (holes) in the semiconductor. Screening of the original negative surface charge from the biomolecule occurs due to the mobilization of positive ions in the electrical double layer, which compete to reduce the fraction of positive charges in the SWCNT/graphene surface. The positive charges induced in the SWCNT or graphene essentially p-dopes the material—increasing the number of hole carriers—which is graphically observed in the shift of the I_{DS}-V_G transfer curve towards positive gate voltages [5,44].
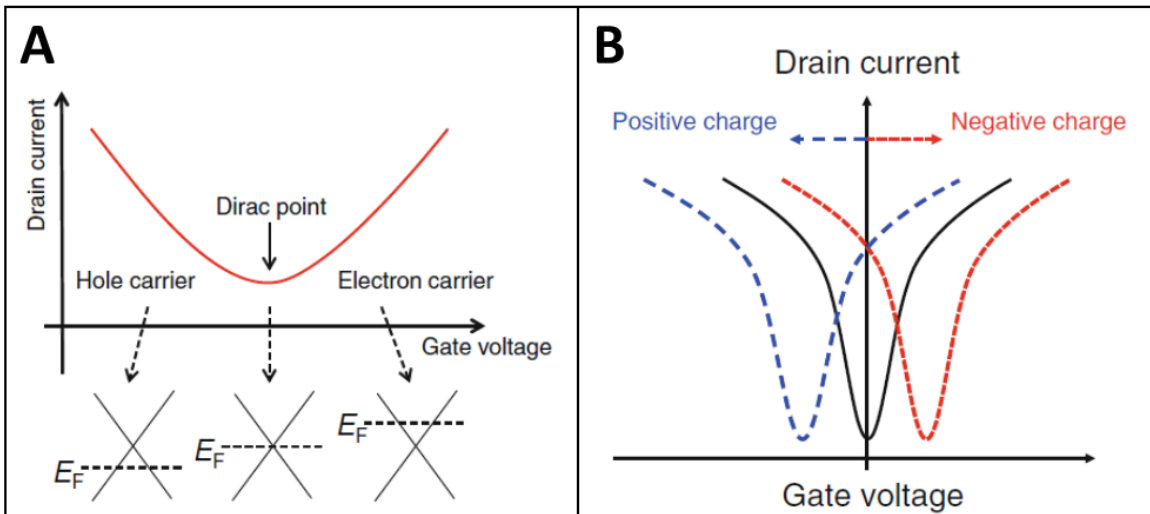
Figure 2.2: Schematic for (A) graphene FET transfer characteristic with the band structures for each regime and (B) changes in transfer characteristic due electrostatic gating by charged analytes. Adapted from [5].

19

Charge screening effect from the double layer capacitance offsets the surface potential—from a charged analyte or biomolecule—experienced by the SWCNT or graphene by neutralizing the surface potential of the surface charge at the semiconductor-liquid interface. Therefore, a solution with higher ionic strength causes a compression of the electrical double layer, leading to a reduction in the Debye length, and reduces the field effect of the surface charge of the biomolecule, which reduces the overall sensitivity of the device [5,44].

Thus, based on the above sensing mechanisms, detection of analytes by SWCNTs and graphene FET biosensors can be achieved through monitoring the device resistance/conductance, threshold gate voltage shift or transconductance.

1.4 Fabrication and Functionalization of SWCNT and Graphene FET biosensors:

1.4.1.1 Fabrication of SWCNT and Graphene FET Biosensors

As previously described, SWCNT and graphene-based FET biosensor configuration have source and drain terminals that are bridged by a semiconducting channel, which consists of the semiconducting carbon nanomaterials. Although device dimensions may vary from one study to another, typical electrode and channel dimensions can range between few millimeters to micrometers and even nanometers. Microfabrication and nanofabrication techniques, such as photolithography and electron beam lithography, are typically used for patterning the source and drain metal electrodes onto a substrate, typically SiO_2/Si wafer [2,3]. The back-gate voltage can be applied directly to the

semiconducting Si layer of the wafer whereas a top-gate voltage requires the additional use of a third reference electrode—usually an Ag/AgCl reference electrode as shown in Figure 2.3 [44,45].
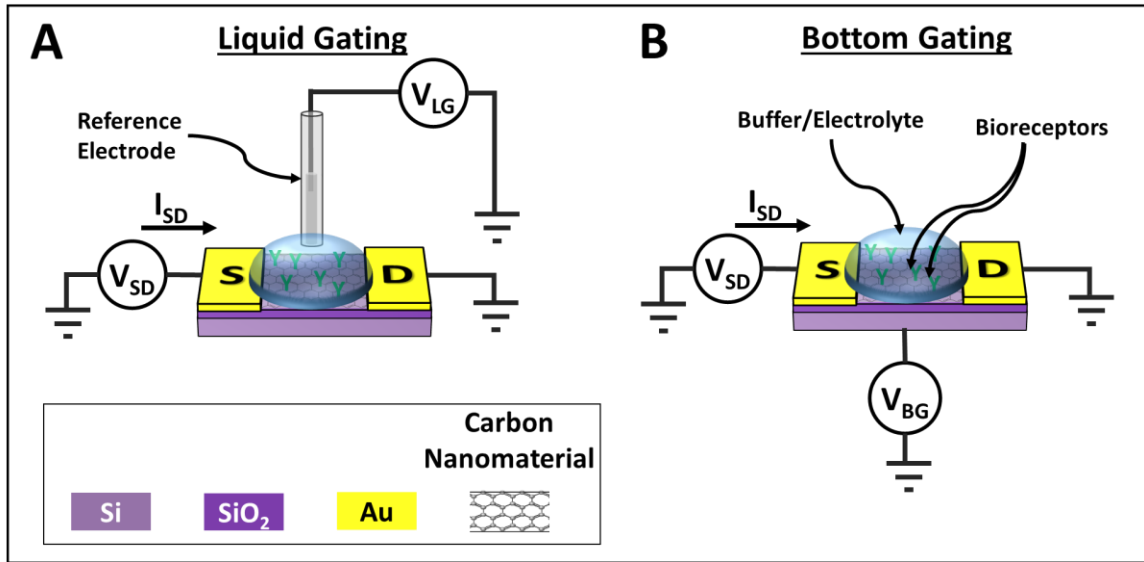
Figure 2.3*: General FET-based biosensor configuration for (A) liquid-gated and (B) bottom-gated devices.*

Diverse methods used for synthesizing and preparing SWCNTs, graphene, and rGO yields these products in various forms, such as colloidal suspensions, solid powders, or thin films which dictate the methods that can be used to integrate these carbon nanomaterials into FET biosensors. Nevertheless, in one fabrication approach, carbon nanomaterials are first deposited or grown directly onto the substrate of the FET device, followed by patterning of metal electrodes [26,43,46,47]. For example, CNTs can be directly grown onto SiO_2/Si substrates using CVD synthesis method [17,43]. Also, graphene grown directly on SiC substrates can be immediately patterned with metal electrodes [26]. In top-down fabrication, deposition of CNTs, graphene, or reduced/unreduced graphene oxide dispersed

21

in a colloidal suspension can be performed via direct application of the solution onto the substrate using methods such as drop casting, spray coating, spin coating, and AC dielectrophoresis [3]. A simple method for preparing dense CNT networks or GO films onto the device surface is the use of (3-aminopropyl)triethoxysilane (APTES) to functionalize SiO_2 surfaces prior to deposition of the carbon nanomaterials [48–50]. Modification of the substrate surface with APTES (or similar derivatives) enhanced electrostatic attraction of CNTs and GO flakes onto the aminated substrate surface. Prior to deposition onto the desired substrate, solid powders of carbon nanomaterials can be re-suspended into various organic solvents as well as surfactant-containing solutions, usually assisted by sonication [32,51]. This method reproducibly produces a uniformly distributed high density network semiconducting channel.

CVD grown graphene film can be transferred onto the desired substrate by first depositing a supporting polymer coating—usually poly(methyl methacrylate)—to protect the graphene film from damage and disintegration during the transfer step. The metal catalyst is removed from underneath the protected graphene film by chemical etchants. For graphene grown on copper foils, ferric chloride ($FeCl_3$) solution is used for etching away the copper foil [28,29].

1.4.1.2 Functionalization of CNTs and graphene with bioreceptor molecules.

In order to achieve specific detection of analyte molecules, the carbon nanomaterial transducer element requires functionalization with the biorecognition elements (e.g. antibodies, enzymes, aptamers, and other binding peptides, etc.). Conjugation of CNT and

graphene with the biorecognition molecules is achieved through various chemical means that can be categorized as direct covalent conjugation to the carbon nanostructure or through non-covalent conjugation to the nanostructure as illustrated in Figure 2.4 [52,53].

Covalent chemical functionalization of CNTs can be categorized into two strategies: (1) End-cap and defect-site chemistry, and (2) functionalization of pristine CNT side-wall [53]. End-cap and defect-site chemistry takes advantage of the more reactive end-caps of CNTs and localized defects in the nanotube lattice—containing oxygenated groups such as carboxyl groups. Covalent chemical functionalization of the pristine CNT side-walls utilizes a multitude of chemistries such as ozonation, fluorination, and oxidation to yield a variety of new functional groups, such as amines (Figure 2.4B). Carboxyl and amine groups are common chemical targets for further conjugation of biorecognition molecules via EDC/NHS and aldehyde-activated coupling chemistries, respectively.

Similarly, covalent chemical functionalization of pristine graphene and graphene oxide has been extensively studied and comprehensively reviewed by Georgakilas et al. [54,55]. Covalent functionalization of pristine graphene capitalizes on the reactivity of C=C bonds to free radicals and dienophile to introduce new organic functional groups that can be used for further covalent conjugation with biomolecules (Figure 2.4C). Since GO and rGO already contain oxygenated groups, such as carboxyl and epoxide groups, further chemical functionalization and conjugation of biomolecules can be performed using common bioconjugation chemistries like EDC/NHS conjugation method.

One major disadvantage of covalent functionalization of CNTs and graphene is the alteration of electronic structure and properties of the nanotubes due to disruption of carbon

sp^2 bonds [53,54]. Thus, non-covalent conjugation strategies provide attractive alternatives. Non-covalent conjugation of biomolecules onto CNT and graphene sp^2 carbon surfaces typically uses bi-functional linker molecules, such as 1-pyrenebutanoic acid succinimidyl ester (PBASE). The π-electron-rich pyrenyl group π-stacks with the carbon nanostructure while the succinimidyl ester group specifically reacts with amine groups on the biorecognition molecule to form an amide bond (Figure 2.4A). Alternatively, non-covalent conjugation of biomolecules onto CNT and graphene is performed by simple physical adsorption of the biomolecules onto the surface of the carbon nanomaterials [56,57]. After functionalizing the carbon nanomaterials with the desired biorecognition molecules, unreacted chemical moieties and carbon surfaces are chemically quenched and physically blocked—with surfactants, amphipathic polymers, or nonspecific protein, respectively [3]. Chemical quenching and blocking minimize non-specific binding during sensing procedure. In biosensing applications, the preferred method for conjugation of SWCNT and graphene surfaces with biorecognition molecules is through the non-covalent functionalization approach as discussed in the following examples of recent development of CNT and graphene FET-based biosensors.
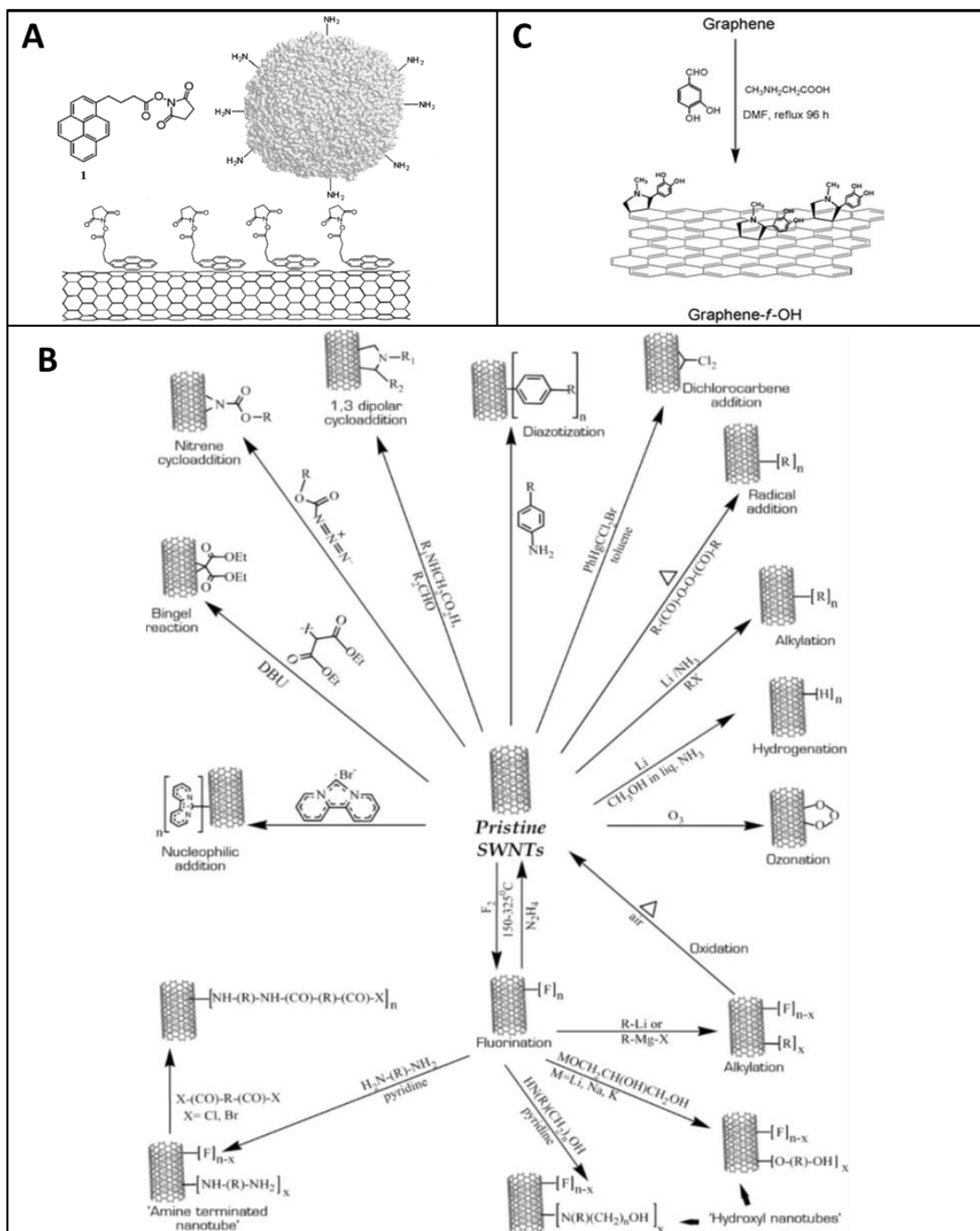
Figure 2.4: Functionalization strategies for SWCNT and graphene: (A) Noncovalent functionalization of SWCNT sidewalls using PBASE linkers, adapted from [57]; (B) Covalent functionalization chemistries for pristine SWCNT sidewalls, adapted from [53]; (C) Covalent chemical functionalization of pristine graphene sheet using 1,3 dipolar cycloaddition of azomethine ylide, adapted from [54].

1.5 Carbon Nanomaterial-based Nano FET Biosensors

1.5.1 Specific detection of proteins and DNA

SWCNT and graphene-based FET biosensors for detection of proteins and nucleic acid-based analytes have been demonstrated using a wide range of detection strategies as well as device configuration and fabrication strategies as summarized in Table 2.1 [5,45,50,58–61]. In one example, a solution-gated rGO-based FET biosensor was developed for detection of the prostate cancer biomarker, prostate-specific antigen complexed with α_1-antichymotrypsin (PSA-ACT) [50]. Using rGO functionalized (via PBASE linkers) with monoclonal antibodies against PSA-ACT, the device was able to quantitatively detect concentrations of PSA-ACT antigens in human serum in the femtomolar range.

There is significant effort invested into developing methods for improving performance of these biosensors, such as sensitivity and real-time detection capability. For example, to enhance sensitivity of electrical detection of PSA-ACT with monoclonal antibodies against PSA-ACT as the bioreceptor element, Kim et al. employed a functionalization strategy that minimized the effects of charge screening by the electrical double layer. Specifically, by increasing the spacing between antibody receptors, the charged antigens are able to more easily approach the SWCNT surface within the distance of the Debye length to affect the conductance of the SWCNT. Mixtures at different molar ratios of PBASE linkers and 1-pyrenebutanol (PB) spacer molecules were investigated to demonstrate the effects of density of antibody functionalization on device sensitivity shown in Figure 2.5. Thus, devices using a 1:3 ratio of PBASE linker to PB spacers for antibody

functionalization were found to achieve a much lower LOD of 1.0 ng/mL compared to devices that used only PBASE linkers (LOD ~ 500 ng/mL).

While antibodies are popular protein-based biorecognition molecules, aptamers—a class of nucleic acid-based synthetic biorecognition molecules—offer another alternative for specific analyte detection. Upon binding of larger analytes to the smaller-sized aptamer functionalized on the surface of carbon nanomaterials, the effects of charge screening can be reduced as the analytes are physically closer to the transducer surface within the distance of the Debye length [62]. Another similar strategy to allow bound analytes to approach the transducer surface within the Debye length is to use antibody fragments, such as immunoglobulin Fabs or F(ab')2 fragments. Antibodies, specifically of immunoglobulin-G (IgG) isotype, can be enzymatically cleaved using papain to yield the univalent antigen-binding Fab fragments which are approximately 3-5 nm in the largest dimension compared to the whole IgG molecule which are 10-15 nm. This strategy was demonstrated on a solution-gated graphene-based FET biosensor using Fabs receptor molecules to detect for heat-shock proteins (HSPs) [59]. The biosensor used mechanically exfoliated single-layer graphene (via repeated peeling of graphite) as the transducer. The Fabs were functionalized onto graphene using PBASE linkers. The biosensor achieved an LOD of 100 pM for the HSP analyte with a dynamic range of hundreds of pM to hundreds of nM.
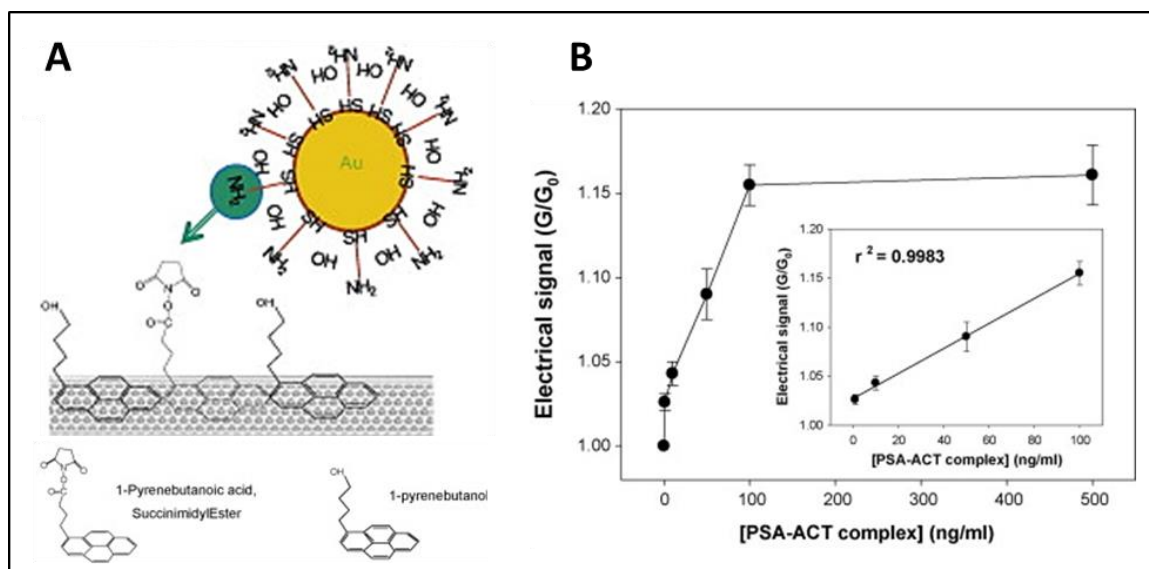
Figure 2.5: *(A) Schematic diagram of PBASE linkers and PB spacers non-covalently attached to SWCNT surface, where amines on the gold nanoparticle only react with PBASE linkers. (B) Calibration curve for immuno-detection of PSA-ACT complexes using CNT-FET devices modified with 1:3 ratio of PBASE to PB. Adapted from* [58].

Detection of nucleic acid-based analytes, such as DNAs and microRNAs, has also been shown to be feasible by various groups using CNT and graphene-based FET biosensors, albeit with some variations in assay strategy and sensing mechanisms in comparison to detection of proteins due to the chemical and structural differences between these analytes. More specifically, DNA detection via sequence-specific hybridization is a common assay strategy for ensuring specificity in biosensing. A general design for FET biosensors that utilized a DNA hybridization strategy is to functionalize the complementary DNA/RNA strand onto the transducer surface, whereby complementary binding of the target strand leads to a detectable electrical response. Demonstrating this detection scheme, Star et al. developed a label-free SWCNT-based FET biosensor for the detection of complementary DNA (cDNA) strands capable of discriminating single-nucleotide

28

polymorphisms (SNP) [61]. Single-stranded DNA (ssDNA) molecules were non-covalently

attached to the SWCNT sidewalls simply by allowing the ssDNA to wrap around individual

SWCNTs via π- stacking interactions between the nucleotide bases and SWCNT sidewalls.

Complementary DNA strands can subsequently be hybridized with the immobilized

ssDNA on SWCNT sidewalls, which were observed in changes of the device conductance

(inverse of resistance).   Hybridization experiments with fully complementary 12-mer

oligonucleotides resulted in decreased conductance while completely mismatched DNA

oligonucleotides resulted in significantly smaller changes in conductance. Similarly, in

SNP discrimination experiments, the biosensor showed significant decrease in conductance

only for fully matched DNA target strands. The biosensor was able to detect 100 pM of

the target DNA in the presence of 10^4-fold molar excess of nonhomologous DNA. The

authors further employed another chemical strategy, where counterions such as Mg^{2+} were

used during incubation steps, which enhanced the efficiency of DNA hybridization, and

consequently conferred a 1000-fold increase (from 1 nM to 1 pM) in sensitivity to the

biosensor system [61].   Similarly, DNA detection by hybridization of complementary

oligonucleotides have also been shown in other CNT-based FET biosensors, with

variations in device architecture, functionalization strategy, and performance

characteristics [63,64].

FET biosensors for specific and label-free detection of DNA hybridization have

been developed using both RGO and CVD graphene [65–68]. Using chemically reduced GO

as the semiconducting channel in a solution-gated FET biosensor architecture, Stein et al.

showed that real-time detection of DNA hybridization was feasible with their device [65].

The aminated ssDNA probe strand was functionalized onto RGO surfaces by covalent conjugation method. The GO surface was first aminated with ethylenediamine (EDA) prior to chemical reduction. After chemical reduction of GO using hydrazine vapor, the amine functional groups from the EDA-functionalized RGO was further reacted with glutaraldehyde (a homo-bifunctional linker) to introduce reactive aldehyde groups for further conjugation with aminated-ssDNA probe strands. Real-time detection was enabled by integrating the biosensor chip into a flow cell which allowed for controlled injections of samples at specific times. The biosensing system comprised two FET biosensors—one was functionalized with the complementary ssDNA probe for sensing while the other was functionalized with non-complementary ssDNAs for use as a reference. This approach allowed for a signal processing step of subtracting the electrical signals between the sensing and reference devices to remove background noise caused by nonspecific binding of non-complementary DNA onto RGO surfaces. The final biosensor achieved an estimated LOD of ~2 nM for target DNA strands.

In another study, Zheng et al. developed an FET biosensor using CVD grown single layer graphene (SLG) as the transducer to detect specific DNA hybridization [67]. Using a PBASE linker, the SLG channel was non-covalently functionalized with peptide nucleic acid (PNA), the probe molecule. An advantage in using PNA as a probe molecule versus DNA is minimization of electrostatic repulsion between two hybridized strands because the negatively charged deoxyribose phosphate backbone in DNA is replaced by the charge neutral peptide backbone in PNA [68]. Hybridization of the PNA with complementary target DNA produced a left-shift of the Dirac point of the device characteristic, which was

suggested to be caused by n-doping of graphene by the electron-rich nucleobases of the bound DNA strand. This sensing mechanism for DNA and nucleic acid-based analytes have been previously reported, as well. Non-complementary and one-base-mismatched DNA (at various concentrations) tested on the biosensor yielded negligible and significantly lower changes in transfer characteristics of the device, respectively, compared to incubations with complementary target DNA. The label-free SLG-FET biosensor system achieved a detection limit of 10 fM.

MicroRNAs (miRNAs) are emerging as a useful class of biomarkers in disease diagnostics. Efforts have been made to develop carbon nanomaterial-based FET-type biosensors for detection of these types of biomarkers that would provide viable and highly sensitive alternatives to traditional molecular diagnostic modalities such as reverse transcriptase-polymerase chain reaction [69]. For example, Ramnani et al. devised an SWCNT-based chemiresistor in which a combined assay strategy was employed for quantitative detection of miRNA-122a, a 21 nucleotide-long single-stranded (ss)-RNA biomarker linked to lipid metabolism, homeostasis, and hepatitis C viral replication in the liver [69]. This combined assay strategy first made use of sequence-specific hybridization of the target ss-miRNA-122a strand with a complementary probe strand at an elevated temperature of 37°C. Next, the duplexed miRNA was incubated with SWCNTs functionalized/modified with p19 RNA-binding protein. The 19kDa RNA-binding protein, p19 from Carnation Italian ringspot virus, has specific affinity to 21-23 nucleotide-long double-stranded RNA in a size-dependent and sequence-independent manner. Thus, device conductance/resistance was proportionately modulated upon binding of hybridized miRNA-122a strands to the

p19-functionalized SWCNT channel. The SWCNT-based chemiresistor system achieved

linear detection of miRNA-122a in the 1 attomolar (aM) to 10 fM range, with a responsivity

of 0.42 per decade of molar concentration of miRNA-122a even in the presence of excess

yeast RNA at 10 µg. This biosensor demonstrates the feasibility for a hybrid approach for

label-free and sequence-specific detection of small nucleotide strands using nucleotide-

based probes and protein-based bioreceptors specific to the hybridized target-probe

strands.

Analyte Type	Carbon Nanomaterial & Device Configuration	Target Analyte(s)	Bioreceptor(s)	Limit of Detection	Sensitivity	References
Protein-Based Molecules	SWCNT Chemiresistor	Protective Antigen toxin, Anthrax	ssDNA Aptamer	1 nM	0.11 nM^{-1}	[70]
		Salivary α-amylase	IgG anti-α-amylase	6 µg/mL	2.4×10^{-4} mL/µg	[51]
		Cardiac Troponin I (cTnI)	IgG anti-cTnI	0.001 ng/mL	0.02 /log[ng/mL]	[71]
		Cardiac Myoglobin (cMb)	IgG anti-cMb	24.2 pg/mL	11.1 /log[µg/mL]	[72]
	SWCNT-FET	Prostate specific antigen/ α1-antichymotrypsin (PSA-ACT)	IgG anti-PSA-ACT complex	1.0 ng/mL	Not Reported	[58]

		complex			
		H63D mutation in the HFE gene	ssDNA probe	1 pM	Not Reported	61
		Immunoglobulin E (IgE)	DNA Aptamer anti-IgE	250 pM	Not Reported	62
	Chemically reduced GO-FET	Prostate specific antigen/ α1-antichymotrypsin (PSA-ACT) complex	IgG anti PSA-ACT complex	100 fg/ml (~1.1 fM)	Not Reported	50
	Thermally reduced GO-FET/Chemiresistor	Human IgG	Gold-labeled goat IgG anti-Human IgG	0.2 ng/mL	Not Reported	33
	Exfoliated graphene-FET	Heat-shock proteins (HSPs)	Fab anti-HSP	100 pM	Not Reported	59
		Bovine serum albumin (BSA)	None (i.e. nonspecific adsorption)	0.3 nM	Not Reported	60
Nucleic Acid-Based Molecules	SWCNT-FET	12-mer target ssRNA	Aminated 12-mer PNA	Not Reported	Not Reported	63
	Single-SWCNT FET	10-mer target ssDNA	10-mer ssDNA probe	Single molecule of ssDNA target	Not Reported	64

	SWCNT Chemiresistor	microRNA-122a	p19 protein	1 aM	0.41 /log[M]	69
	Chemically reduced GO-FET	24-mer target ssDNA	24-mer aminated SSDNA probe	2 nM	Not Reported	65
		22-mer target ssDNA	22-mer peptide nucleic acid probe	100 fM	Not Reported	68
	Thermally reduced and Pt-decorated GO-FET	22-mer target ssDNA	Thiolated 33-mer ssDNA probe	2.4 nM	Not Reported	66
	CVD graphene-FET	22-mer target ssDNA	22-mer peptide nucleic acid probe	10 fM	Not Reported	67
Pathogens	SWCNT Chemiresistor	E. coli	IgG Anti-E. coli O157:H7	10^3 CFU/mL	0.124 mL/CFU	73
		T7 bacteriophage	IgG anti-T7	10^3 PFU/mL	0.142 mL/PFU	

Table 2.1: Recent reports on FET-based biosensors using carbon nanomaterials for detection of protein-based molecules, nucleic acid-based molecules, and pathogens.

1.5.2 Small molecule detection

Small biomolecules, metabolites, and biologically relevant metal ions pose several inherent challenges to conventional FET-based detection methods. Sensitive detection of small biomolecules at low concentrations via CNT or graphene-based FET method is challenging due to the reduced electric field-effect of the smaller-size and fewer-charge

analyte on the carbon nanomaterial transducer element. When compared to larger protein-based analytes, the reduced size of the smaller biomolecules suggests fewer surface charges available on each molecule which reduces the electrostatic gating effect on the semiconducting channel by each analyte's upon binding to an immobilized bioreceptor. For small, uncharged analytes, this reduction in gating effect is even more pronounced. Small analytes that only provide a single binding site or epitope for affinity-based assays pose an additional physical restriction to signal amplification via sandwich-type assay formats. Nevertheless, a novel strategy for overcoming these challenges was demonstrated in several studies using SWCNT-based FET biosensors [74–76]. This strategy applies the principle of competitive displacement of biorecognition molecules (e.g. antibodies) bound to transducer-immobilized analytes by unbounded analytes in the sample. In this format, the biosensor the semiconducting transducer channel of the transducer is functionalized with the small-molecule antigens, followed by specific binding of the immobilized antigens with the corresponding biorecognition molecules. Upon incubation of the biosensor with the sample (containing the unbounded antigens) the specifically bound significantly large biorecognition molecule is displaced. The proportional displacement of the significantly larger biorecognition molecules by the smaller analytes in the sample leads to larger physical and, consequently larger electrical changes, at the transducer-solution interface.

Cella et al. first demonstrated this competitive displacement strategy in the development of a label-free SWCNT-based FET affinity sensor with a chemiresistor configuration for the detection of a monosaccharide, glucose (MW of 180.16 Da) in human plasma [74]. The biosensor consisted of dielectrophoretically aligned semiconducting

SWCNTs deposited between 3-µm spaced gold source and drain electrodes as the electrical transducer element (Figure 2.6A). The SWCNTs were non-covalently functionalized with hydrophobic dextran polysaccharide derivatives, which are chemical analogs of glucose, followed by blocking with Tween-20 surfactants. The bioreceptor used was Concanavalin A (Con A), a metalloprotein with four carbohydrate binding sites. ConA reversibly binds to glucose and dextran, although the protein has lower affinity to dextran than to glucose. The binding of ConA to the carbohydrates, and specifically to dextrans functionalized on SWCNTs, leads to conformational changes to the protein which consequently increases the isoelectric point of the protein and increases positive charge accumulation. Sensing experiments were conducted by first incubating the dextran-functionalized SWCNT chemiresistor with ConA to form dextran-ConA complexes at the SWCNT surfaces, which led to a large increase in device resistance. Then, various concentrations of glucose was incubated with the device followed by washing the displaced ConA and excess analytes from the device, and performing I_D-V_{DS} measurements to determine the corresponding resistance/conductance signals. With increasing concentrations of glucose, the biosensors showed decreasing resistance, as expected with the displacement of ConA receptors from the SWCNT surface that, when previously bound, led to increased device resistance (Figure 2.6B). The biosensor achieved a detection limit of 1 picomolar (pM), a sensitivity of 0.039 per pM glucose, and showed high binding selectivity for glucose when tested

against galactose, another monosaccharide. This biosensing strategy demonstrated feasibility of small-molecule detection and even detection of uncharged molecule [74].
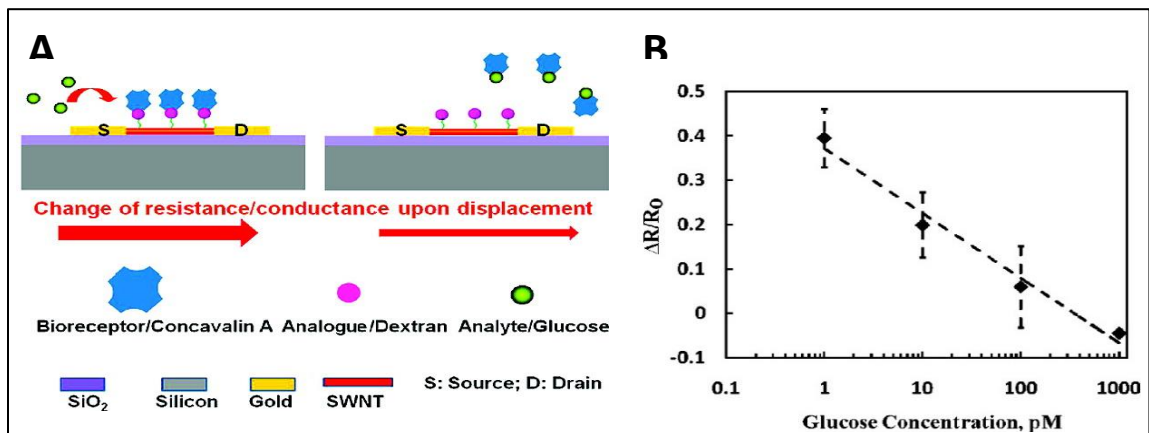
Figure 2.6*: Schematic (A) for SWCNT chemiresistor and glucose detection results (B) in human plasma , adapted from [74].*

Detection of small biomolecules has also been recently demonstrated in an FET biosensor with rGO as the electrical transducer [77]. Yu et al. developed a solution-gated rGO-based FET biosensor, where the rGO surface was non-covalently modified with a pyrene derivative (py-diIM-py) which contains two cationic imidazole groups for enhanced electrostatic binding to the anionic triphosphate groups of adenosine-5'-triphosphate (ATP) and guanosine-5′-triphosphate (GTP). The biosensor configuration consisted of micropattered strips of chemically reduced GO channels on a glass substrate bridging the source and drain electrodes, and a platinum electrode as the gate electrode. Devices functionalized with pyrene derivative achieved detection limit of 400 nM for both ATP and GTP. Interestingly, the authors proposed the signal transduction mechanism of the rGO-based system for sensing of ATP and GTP to be mainly attributed to electron transfer from the nucleosides to rGO (n-doping) rather than electrostatic gating as observed by the

37

negative shift of the Dirac point upon ATP/GTP binding. More specifically, the negatively

charged triphosphate group is electrostatically attracted and bound to the positively charged

imidazole groups of the pyrene derivative molecules at the rGO surface, which causes a

surface localization of the ATP or GTP analyte. The localization of the ATP/GTP allows

for the extension of the electron-rich and aromatic bases (adenine and guanine) of the

nucleotide to undergo π-stacking interaction with the rGO surface, which facilitates

electron transfer to rGO which causes n-doping effects [77]. This study suggests the

dependence of signal transduction mechanism(s) for graphene-based FET biosensors on

the type(s) of analyte and the physical orientation of the analyte at the surface.

Electrical detection of the metal ions Ca^{2+}, Ni^{2+}, Mg^{2+}, Hg^{2+}, and Cd^{2+}, was

demonstrated on a liquid-gated FET biosensor system using micro-patterned rGO channels

functionalized with analyte-specific protein-based receptors by Sudibya et al. [78].

Calmodulin (CaM), a Ca^{2+}-binding protein, was functionalized onto rGO via a PBASE

linker to confer specificity for Ca^{2+} and Mg^{2+} detection, albeit CaM has lower affinity to

Mg^{2+} than Ca^{2+}. The CaM-modified rGO FET biosensor was able to quantitatively detect

both Ca^{2+} (LOD ~ 1 µM, signal-to-noise ratio (SNR) ~20 to 30) and Mg^{2+} while unmodified

rGO FET devices did not detect either metal ions, confirming the specificity due to CaM

receptors. Similarly, for specific detection of Hg^{2+} and Cd^{2+} metal ions, the metallothionein

type II protein (MT-II) receptor was functionalized onto rGO. Sensing experiments

showed that rGO FET biosensors functionalized with MT-II achieved specific and sensitive

detection of both Hg^{2+} (LOD ~ 1 nM, SNR of 25 to 30) and Cd^{2+} (LOD 1 nM, SNR of 15

to 20). Electrical measurements of the sensors in p-type region (V_G = -600 mV) and n-type

region (V_G = 600 mV) for all four metal ions were expected to show similar trends due to electrostatic gating effects since the metal ions Ca^{2+}, Mg^{2+}, Hg^{2+}, and Cd^{2+} were all equally charged. However, the electrical responses for detection of Ca^{2+} and Mg^{2+} on CaM-modified biosensors compared to detection Hg^{2+} and Cd^{2+} with MT-II-modified biosensors showed electrical responses of opposite polarity. The authors explained that Ca^{2+} and Mg^{2+} binding to CaM-functionalized rGO surface is primarily attributed to the direct field effect induced by the bound metal ions, which n-dopes rGO. Conversely, they proposed that Hg^{2+} and Cd^{2+} heavy metals binding to MT-II-functionalized rGO primarily induces conformational changes in the highly negatively charged MT-II receptor such that surface interactions between MT-II molecules and rGO increases, leading to the increased p-doping effect [78]. Sensitive detection of other small biomolecules and metal ions using CNT- and graphene-based FET biosensors have also been demonstrated as exemplified in these recent reports listed in Table 2.2.

Analyte Type	Carbon Nanomaterial & Device Configuration	Target Analyte(s)	Bioreceptor(s)	Limit of Detection	Sensitivity	References
Small Molecules	SWCNT Chemiresistor	MCLR	IgG anti-MCLR	0.6 ng/mL	0.175 /log[g/L]	[76]
		ATP	ssDNA aptamer	1 pM	$1.3\ nM^{-1}$	[79]
		Glucose	Concanavalin A	1 pM	$0.039\ pM^{-1}$	[74]
		Cortisol	IgG anti-cortisol	1 pg/mL	13.97 mL/ng	[40]
Metal and Heavy Metal Ions	SWCNT Chemiresistor	Hg^{2+}	ssDNA aptamer	100 nM	$6.72 \times 10^{-3}\ nM^{-1}$	[80]
		Ni^{2+}	Hexa-histidine	Not Reported	Not Reported	[79]
	Chemically reduced GO-FET	Ca^{2+}, Mg^{2+}, Hg^{2+}, and Cd^{2+}	•Calmodulin (CaM) for detection of Ca^{2+} and Mg^{2+} •Metallothionein type II protein (MT-II) for detection of Hg^{2+} and Cd^{2+}	• Ca^{2+}: ~ 1 µM • Mg^{2+}: Not Reported • Hg^{2+}: ~ 1 nM • Cd^{2+}: ~ 1 nM	Not Reported	[78]

Table 2.2: *Recent reports on FET-based biosensors using carbon nanomaterials for small molecules and metal ions.*

1.6 Conclusion

Considerable efforts have been invested into development of carbon nanomaterial-based FET-type biosensor systems, as seen in the previously discussed examples. Design and fabrication of FET biosensors using these carbon nanomaterials are dependent on the specific physical, chemical, and electrical properties of the materials as well as the synthesis methods of the materials. Detection strategies for these biosensors further depend on the type of analytes, testing environment, and bioreceptor molecules used. While the different sensing mechanisms of CNTs and graphene-based FET biosensors have been generally discussed in this review, it is interesting to note that the sensing mechanisms that lead to the changes in electrical responses and device characteristics vary upon the types of analytes detected, biorecognition molecules used, and device configurations. In some cases, integration of the biosensing elements into a fluid control system can provide additional functionalities, such as real-time detection, and enhance other sensor performance characteristics, such as reproducibility. Thus, incorporating fluidic or microfluidic elements into a biosensor for lab-on-chip applications is an attractive design strategy to leverage the label-free sensing capability and sensitivity of FET biosensors using carbon nanomaterials.

For more specific applications and wider commercialization of FET-based biosensors in the medical field or in the environmental monitoring, these biosensors must also have high tolerance to potential interfering substances in the samples being tested. For example, for measuring glucose levels in a complex medium, such as blood, serum, or even urine, a glucose FET-based biosensor must have a biorecognition element that will

specifically bind only glucose molecules and not other glucose analogs, as well as a signal transduction element that is impervious to the high concentrations of ions in the sample. Additionally, of importance for purposes of medical diagnoses, the biosensor system must be designed to have a detection range that is within the clinically relevant range for the specific analyte of interest.

A desirable characteristic for any biosensor system is portability which is achievable for FET-based biosensors composed of nanometer- to millimeter-sized features. Furthermore, since signal outputs of FET-based biosensors are directly measured as electrical current, measuring instruments for these devices can be less cumbersome, less expensive, and more portable compared to measuring instruments for other types of transducer platforms, such as optical biosensors which require optical components and photodetectors. Demonstrated by the examples in this review, label-free sensing capability is another major advantage of FET-based biosensors using carbon nanomaterials over some optical biosensor platforms which may require fluorescent labels or other photoactive probes.

While carbon nanomaterials, like CVD graphene and SWNTs, have increased in commercial availability, FET-type biosensors using these carbon nanomaterials have yet to reach the same level of commercial availability, especially for analyte-specific applications. For commercial application of these biosensors, scalability of manufacturing these devices is an important design factor. Thus, highly scalable synthesis methods, such as CVD synthesis, of these carbon nanomaterials, coupled with micro- and nanofabrication

technologies adopted from the semiconductor industry make the prospects of commercialization of carbon nanomaterial-based FET biosensors more promising.

1.7 References

1.   Thévenot, D. R., Toth, K., Durst, R. A. & Wilson, G. S. Electrochemical biosensors: recommended definitions and classification. *Biosensors and Bioelectronics* **16,** 121–131 (2001).

2.   Liu, S. & Guo, X. Carbon nanomaterials field-effect-transistor-based biosensors. *NPG Asia Materials* **4,** e23 (2012).

3.   Ramnani, P., Saucedo, N. M. & Mulchandani, A. Carbon nanomaterial-based electrochemical biosensors for label-free sensing of environmental pollutants. *Chemosphere* (2015). doi:10.1016/j.chemosphere.2015.04.063

4.   Martel, R., Schmidt, T., Shea, H. R., Hertel, T. & Avouris, P. Single-and multi-wall carbon nanotube field-effect transistors. *Applied Physics Letters* **73,** 2447–2449 (1998).

5.   Ohno, Y., Maehashi, K. & Matsumoto, K. Graphene Biosensor. in *Frontiers of Graphene and Carbon Nanotubes* (ed. Matsumoto, K.) 91–103 (Springer Japan, 2015).

6.   Geim, A. K. & Novoselov, K. S. The rise of graphene. *Nat Mater* **6,** 183–191 (2007).

7.   Iijima, S. Helical microtubules of graphitic carbon. *Nature* **354,** 56–58 (1991).

8.   Watson, T. J. Carbon-based electronics. *Nature Nanotechnology* **2,** (2007).

9.   Odom, T. W., Huang, J.-L., Kim, P. & Lieber, C. M. Atomic structure and electronic properties of single-walled carbon nanotubes. *Nature* **391,** 62–64 (1998).

10.   Hayashi, T. *et al.* Smallest Freestanding Single-Walled Carbon Nanotube. *Nano Letters* **3,** 887–889 (2003).

11.   *Carbon nanotubes: synthesis, structure, properties, and applications*. (Springer, 2001).

12.   Hu, P. *et al.* Carbon Nanostructure-Based Field-Effect Transistors for Label-Free Chemical/Biological Sensors. *Sensors* **10,** 5133–5159 (2010).

13.   Tans, S. J., Verschueren, A. R. M. & Dekker, C. Room-temperature transistor based on a single carbon nanotube. *Nature* **393,** 49–52 (1998).

14.   Guo, T., Nikolaev, P., Thess, A., Colbert, D. T. & Smalley, R. E. Catalytic growth of single-walled manotubes by laser vaporization. *Chemical Physics Letters* **243,** 49–54 (1995).

15.   Bethune, D. S. *et al.* Cobalt-catalysed growth of carbon nanotubes with single-atomic-layer walls. *Nature* **363,** 605–607 (1993).

16.   Kong, J., Soh, H. T., Cassell, A. M., Quate, C. F. & Dai, H. Synthesis of individual single-walled carbon nanotubes on patterned silicon wafers. *Nature* **395,** 878–881 (1998).

17.   Zhang, T., Mubeen, S., Myung, N. V. & Deshusses, M. A. Recent progress in carbon nanotube-based gas sensors. *Nanotechnology* **19,** 332001 (2008).

18.   Novoselov, K. S. *et al.* Electric field effect in atomically thin carbon films. *science* **306,** 666–669 (2004).

19.   Castro Neto, A. H., Guinea, F., Peres, N. M. R., Novoselov, K. S. & Geim, A. K. The electronic properties of graphene. *Reviews of Modern Physics* **81,** 109–162 (2009).

20.   Hernandez, Y. *et al.* High-yield production of graphene by liquid-phase exfoliation of graphite. *Nature Nanotechnology* **3,** 563–568 (2008).

21.   Lotya, M. *et al.* Liquid Phase Production of Graphene by Exfoliation of Graphite in Surfactant/Water Solutions. *Journal of the American Chemical Society* **131,** 3611–3620 (2009).

22.   Page, T. R., Hayamizu, Y., So, C. R. & Sarikaya, M. Electrical detection of biomolecular adsorption on sprayed graphene sheets. *Biosensors and Bioelectronics* **33,** 304–308 (2012).

23.   Berger, C. *et al.* Electronic confinement and coherence in patterned epitaxial graphene. *Science* **312,** 1191–1196 (2006).

24.   Berger, C. *et al.* Ultrathin Epitaxial Graphite: 2D Electron Gas Properties and a Route toward Graphene-based Nanoelectronics. *The Journal of Physical Chemistry B* **108,** 19912–19916 (2004).

25.   Avouris, P. & Dimitrakopoulos, C. Graphene: synthesis and applications. *Materials today* **15,** 86–97 (2012).

26.   Ang, P. K., Chen, W., Wee, A. T. S. & Loh, K. P. Solution-Gated Epitaxial Graphene as pH Sensor. *Journal of the American Chemical Society* **130,** 14392–14393 (2008).

27.   Reina, A. *et al.* Large Area, Few-Layer Graphene Films on Arbitrary Substrates by Chemical Vapor Deposition. *Nano Letters* **9,** 30–35 (2009).

28.   Li, X. *et al.* Large-Area Synthesis of High-Quality and Uniform Graphene Films on Copper Foils. *Science* **324,** 1312–1314 (2009).

29.   Lee, Y. *et al.* Wafer-Scale Synthesis and Transfer of Graphene Films. *Nano Letters* **10,** 490–493 (2010).

30.   Hummers Jr, W. S. & Offeman, R. E. Preparation of graphitic oxide. *Journal of the American Chemical Society* **80,** 1339–1339 (1958).

31.   Paredes, J. I., Villar-Rodil, S., Martinez-Alonso, A. & Tascon, J. M. D. Graphene oxide dispersions in organic solvents. *Langmuir* **24,** 10560–10564 (2008).

32.   Stankovich, S. *et al.* Synthesis of graphene-based nanosheets via chemical reduction of exfoliated graphite oxide. *Carbon* **45,** 1558–1565 (2007).

33.   Mao, S., Yu, K., Lu, G. & Chen, J. Highly sensitive protein sensor based on thermally-reduced graphene oxide field-effect transistor. *Nano Research* **4,** 921–930 (2011).

34.   Singh, M., Yadav, A., Kumar, S. & Agarwal, P. Annealing induced electrical conduction and band gap variation in thermally reduced graphene oxide films with different sp2/sp3 fraction. *Applied Surface Science* **326,** 236–242 (2015).

35.   Lee, C.-S., Kim, S. K. & Kim, M. Ion-Sensitive Field-Effect Transistor for Biological Sensing. *Sensors* **9,** 7111–7131 (2009).

36.   Kakatkar, A., Abhilash, T. S., Alba, R. D., Parpia, J. M. & Craighead, H. G. Detection of DNA and poly-l-lysine using CVD graphene-channel FET biosensors. *Nanotechnology* **26,** 125502 (2015).

37.   Balasubramanian, K. & Burghard, M. Biosensors based on carbon nanotubes. *Analytical and Bioanalytical Chemistry* **385,** 452–468 (2006).

38.   He, Q., Wu, S., Yin, Z. & Zhang, H. Graphene-based electronic sensors. *Chemical Science* **3,** 1764 (2012).

39.   Katz, H. Chemically Sensitive Field-Effect Transistors and Chemiresistors: New Materials and Device Structures. *Electroanalysis* **16,** 1837–1842 (2004).

40.   Tlili, C., Myung, N. V., Shetty, V. & Mulchandani, A. Label-free, chemiresistor immunosensor for stress biomarker cortisol in saliva. *Biosensors and Bioelectronics* **26,** 4382–4386 (2011).

41.   Chen, Z., Appenzeller, J., Knoch, J., Lin, Y. & Avouris, P. The Role of Metal−Nanotube Contact in the Performance of Carbon Nanotube Field-Effect Transistors. *Nano Letters* **5,** 1497–1502 (2005).

42.   Heller, I. *et al.* Identifying the Mechanism of Biosensing with Carbon Nanotube Transistors. *Nano Letters* **8,** 591–595 (2008).

43.   Byon, H. R. & Choi, H. C. Network Single-Walled Carbon Nanotube-Field Effect Transistors (SWNT-FETs) with Increased Schottky Contact Area for Highly Sensitive Biosensor Applications. *Journal of the American Chemical Society* **128,** 2188–2189 (2006).

44.   Heller, I. *et al.* Influence of Electrolyte Composition on Liquid-Gated Carbon Nanotube and Graphene Transistors. *Journal of the American Chemical Society* **132,** 17149–17156 (2010).

45.   Ohno, Y., Maehashi, K. & Matsumoto, K. Graphene field-effect transistors for label-free chemical and biological sensors. in (eds. George, T., Islam, M. S. & Dutta, A. K.) 803121-803121–6 (2011). doi:10.1117/12.882859

46.   Besteman, K., Lee, J.-O., Wiertz, F. G. M., Heering, H. A. & Dekker, C. Enzyme-Coated Carbon Nanotubes as Single-Molecule Biosensors. *Nano Letters* **3,** 727–730 (2003).

47.   Li, Y.-L., Kinloch, I. A. & Windle, A. H. Direct Spinning of Carbon Nanotube Fibers from Chemical Vapor Deposition Synthesis. *Science* **304,** 276–278 (2004).

48.   Hu, P. *et al.* Self-assembled nanotube field-effect transistors for label-free protein biosensors. *Journal of Applied Physics* **104,** 074310 (2008).

49.   Tlili, C., Badhulika, S., Tran, T.-T., Lee, I. & Mulchandani, A. Affinity chemiresistor sensor for sugars. *Talanta* **128,** 473–479 (2014).

50.   Kim, D.-J. *et al.* Reduced graphene oxide field-effect transistor for label-free femtomolar protein detection. *Biosensors and Bioelectronics* **41,** 621–626 (2013).

51.   Tlili, C., Cella, L. N., Myung, N. V., Shetty, V. & Mulchandani, A. Single-walled carbon nanotube chemoresistive label-free immunosensor for salivary stress biomarkers. *The Analyst* **135,** 2637 (2010).

52.   Sun, Y.-P., Fu, K., Lin, Y. & Huang, W. Functionalized Carbon Nanotubes: Properties and Applications. *Accounts of Chemical Research* **35,** 1096–1104 (2002).

53.   Banerjee, S., Hemraj-Benny, T. & Wong, S. S. Covalent Surface Chemistry of Single-Walled Carbon Nanotubes. *Advanced Materials* **17,** 17–29 (2005).

54.   Georgakilas, V. *et al.* Functionalization of Graphene: Covalent and Non-Covalent Approaches, Derivatives and Applications. *Chemical Reviews* **112,** 6156–6214 (2012).

55.   Georgakilas, V. *et al.* Organic functionalisation of graphenes. *Chemical Communications* **46,** 1766 (2010).

56.   Choi, E.-Y. *et al.* Noncovalent functionalization of graphene with end-functional polymers. *Journal of Materials Chemistry* **20,** 1907 (2010).

57.   Chen, R. J., Zhang, Y., Wang, D. & Dai, H. Noncovalent Sidewall Functionalization of Single-Walled Carbon Nanotubes for Protein Immobilization. *Journal of the American Chemical Society* **123,** 3838–3839 (2001).

58.   Kim, J. P., Lee, B. Y., Lee, J., Hong, S. & Sim, S. J. Enhancement of sensitivity and specificity by surface modification of carbon nanotubes in diagnosis of prostate cancer based on carbon nanotube field effect transistors. *Biosensors and Bioelectronics* **24,** 3372–3378 (2009).

59.   Okamoto, S., Ohno, Y., Maehashi, K., Inoue, K. & Matsumoto, K. Immunosensors Based on Graphene Field-Effect Transistors Fabricated Using Antigen-Binding Fragment. *Japanese Journal of Applied Physics* **51,** 06FD08 (2012).

60.   Ohno, Y., Maehashi, K., Yamashiro, Y. & Matsumoto, K. Electrolyte-Gated Graphene Field-Effect Transistors for Detecting pH and Protein Adsorption. *Nano Letters* **9,** 3318–3322 (2009).

61.   Star, A. *et al.* Label-free detection of DNA hybridization using carbon nanotube network field-effect transistors. *Proceedings of the National Academy of Sciences of the United States of America* **103,** 921–926 (2006).

62.   Maehashi, K. *et al.* Label-Free Protein Biosensor Based on Aptamer-Modified Carbon Nanotube Field-Effect Transistors. *Analytical Chemistry* **79,** 782–787 (2007).

63.   Martínez, M. T. *et al.* Label-Free DNA Biosensors Based on Functionalized Carbon Nanotube Field Effect Transistors. *Nano Letters* **9,** 530–536 (2009).

64.   Sorgenfrei, S. *et al.* Label-free single-molecule detection of DNA-hybridization kinetics with a carbon nanotube field-effect transistor. *Nature Nanotechnology* **6,** 126–132 (2011).

65.   Stine, R., Robinson, J. T., Sheehan, P. E. & Tamanaha, C. R. Real-Time DNA Detection Using Reduced Graphene Oxide Field Effect Transistors. *Advanced Materials* **22,** 5297–5300 (2010).

66.   Yin, Z. *et al.* Real-time DNA detection using Pt nanoparticle-decorated reduced graphene oxide field-effect transistors. *Nanoscale* **4,** 293–297 (2012).

67.   Zheng, C. *et al.* Fabrication of Ultrasensitive Field-Effect Transistor DNA Biosensors by a Directional Transfer Technique Based on CVD-Grown Graphene. *ACS Applied Materials & Interfaces* **7,** 16953–16959 (2015).

68.   Cai, B. *et al.* Ultrasensitive Label-Free Detection of PNA–DNA Hybridization by Reduced Graphene Oxide Field-Effect Transistor Biosensor. *ACS Nano* **8,** 2632–2638 (2014).

69.   Ramnani, P., Gao, Y., Ozsoz, M. & Mulchandani, A. Electronic Detection of MicroRNA at Attomolar Level with High Specificity. *Analytical Chemistry* **85,** 8061–8064 (2013).

70.   Cella, L. N. *et al.* Nano Aptasensor for Protective Antigen Toxin of Anthrax. *Analytical Chemistry* **82,** 2042–2047 (2010).

71.   Rajesh *et al.* Label-free detection of cardiac troponin-I using gold nanoparticles functionalized single-walled carbon nanotubes based chemiresistive biosensor. *Applied Physics Letters* **103,** 203703 (2013).

72.   Puri, N., Niazi, A., Biradar, A. M., Mulchandani, A. & Rajesh. Conducting polymer functionalized single-walled carbon nanotube based chemiresistive biosensor for the detection of human cardiac myoglobin. *Applied Physics Letters* **105,** 153701 (2014).

73.   García-Aljaro, C. *et al.* Carbon nanotubes-based chemiresistive biosensors for detection of microorganisms. *Biosensors and Bioelectronics* **26,** 1437–1441 (2010).

74.   Cella, L. N., Chen, W., Myung, N. V. & Mulchandani, A. Single-Walled Carbon Nanotube-Based Chemiresistive Affinity Biosensors for Small Molecules: Ultrasensitive Glucose Detection. *Journal of the American Chemical Society* **132,** 5024–5026 (2010).

75.   Park, M., Cella, L. N., Chen, W., Myung, N. V. & Mulchandani, A. Carbon nanotubes-based chemiresistive immunosensor for small molecules: Detection of nitroaromatic explosives. *Biosensors and Bioelectronics* **26,** 1297–1301 (2010).

76.   Tan, F., Saucedo, N. M., Ramnani, P. & Mulchandani, A. Label-Free Electrical Immunosensor for Highly Sensitive and Specific Detection of Microcystin-LR in Water Samples. *Environmental Science & Technology* **49,** 9256–9263 (2015).

77.   Yu, C. *et al.* Creation of Reduced Graphene Oxide Based Field Effect Transistors and Their Utilization in the Detection and Discrimination of Nucleoside Triphosphates. *ACS Applied Materials & Interfaces* **7,** 10718–10726 (2015).

78.   Sudibya, H. G., He, Q., Zhang, H. & Chen, P. Electrical Detection of Metal Ions Using Field-Effect Transistors Based on Micropatterned Reduced Graphene Oxide Films. *ACS Nano* **5,** 1990–1994 (2011).

79.   Das, B. K. *et al.* Single-walled carbon nanotubes chemiresistor aptasensors for small molecules: picomolar level detection of adenosine triphosphate. *Chemical Communications* **47,** 3793 (2011).

80.   Gong, J.-L., Sarkar, T., Badhulika, S. & Mulchandani, A. Label-free chemiresistive biosensor for mercury (II) based on single-walled carbon nanotubes and structure-switching DNA. *Applied Physics Letters* **102,** 013701 (2013).

Chapter 3

Generation of Anti-SDE1 Antibody and Development of an Enzyme-Linked Immunosorbent Assay (ELISA) for Detection of SDE1 HLB Biomarker

3.1 Abstract

Polyclonal antibodies were generated to a secretory protein biomarker, SDE1, unique to *Candidatus* Liberibacter asiaticus (*C*Las), a bacterial pathogen responsible for citrus greening disease or Huanglongbing (HLB) disease, in rabbits. These antibodies were affinity purified from rabbit antisera for immunoassay and biosensor applications. We evaluated the purified anti-SDE1 antibodies using indirect capture and indirect competitive inhibition (ICI) enzyme-linked immunosorbent assays (ELISAs). The ELISAs developed using anti-SDE1 antibodies were further used on 10 infected grapefruit plant samples and 6 health negative controls. The ELISA platform is a valuable tool for platform-independent evaluation of biomarkers, antibodies, and other reagents for biosensor development.

3.2 Introduction

After the discovery and isolation of a 14-kDa sec-delivered effector (SDE) protein biomarker SDE1, unique to C*Las*, the Ma Lab used the recombinantly expressed antigens to immunize rabbits, to induce antibody production by the rabbits[1]. After each immunization periods, rabbit antisera were obtained. While the antisera contain the

51

antibodies specific to our biomarker, these polyclonal antibodies (pAbs) require further purification from the antisera matrix to remove undesired proteins and other molecules which will inadvertently interfere with any bioconjugation chemistries during future biosensor development[2].

Therefore, the goal of this work is to procure purified antibodies against the SDE1 HLB biomarker followed by evaluation of the antibodies' sensitivity and specificity to the biomarker by an independent detection platform. A secondary goal is to develop an orthogonal immunoassay method for comparing the future development of biosensors using the same SDE1 antigen and anti-SDE1 pAbs. Firstly, we evaluated various batches of rabbit antisera with the highest antigen binding profiles for antibody affinity purification by standard indirect capture enzyme-linked immunosorbent assays (ELISAs)[3,4]. Secondly, we performed affinity purification of polyclonal antibodies from selected antisera followed by indirect capture ELISA and sodium dodecyl sulfate polyacrylamide gel electrophoresis (SDS-PAGE) for verification of antibody activity and purification. Next, we developed an indirect competitive inhibition ELISA for initial interference and sensitivity testing to identify and address platform-independent issues and parameters, such as interference or cross-reactivity, which will then be adapted for later biosensor development[3]. Finally, we used our CI-ELISA for testing infected and healthy citrus samples.

As shown in Figure 3.1A, an indirect ELISA consists of immobilization of SDE1 antigens onto the surface of ELISA wells, which allow for specific capture of primary pAbs anti-SDE1 against the immobilized antigens. After washing unbound molecules from the ELISA wells, secondary goat-anti-Rabbit-IgG-Horseradish-peroxidase (HRP) conjugates

to bind to the captured pAbs-anti-SDE1[3–5]. Washing off unbound secondary antibody conjugates followed by incubation ABTS HRP substrates allow for optical detection of immobilized SDE1/pAb-anti-SDE1/goat-anti-rabbit-IgG-HRP complexes. We used this indirect ELISA format to determine the binding affinity and specificity of our purified pAbs-anti-SDE1. The higher the binding affinity of various pAbs, the lower concentration of pAbs is needed to generate an optical signal. Higher antibody binding affinity is desirable for our biosensors, which confer higher sensitivity to the antigens.
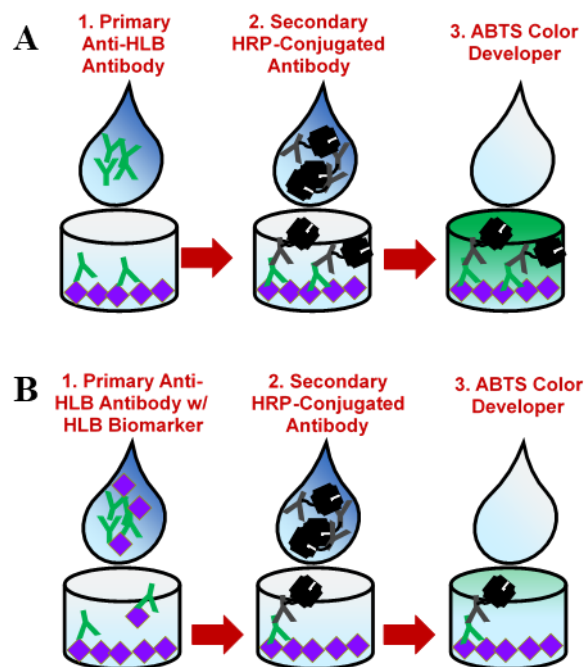
Figure 3.1: *(A) Schematic for indirect ELISAs format and (B) Indirect competitive inhibition ELISAs used.*

Utilizing the indirect ELISA format, we can further develop an independent competitive immunoassay platform as shown in figure 3.1B for detection of the HLB

biomarker SDE1. In the ICI-ELISA, we pre-incubated (in separate reaction tubes) a specific concentration of the primary pAbs-anti-SDE1 antibodies with various samples spiked with the SDE1 antigens, all the while maintaining the same final volume of the mixtures and thus the same primary antibody concentration for each sample[3,6]. A proportionate number of SDE1 antigens in each of the pAb/sample mixture bind to the same number of primary pAbs-anti-SDE1. The pAb/sample mixture will then be introduced to the ELISA wells immobilized with the SDE1 antigens. Only the remaining population of unbound pAbs-anti-SDE1 can bind to the immobilized SDE1. The population SDE1-complexed pAbs-anti-SDE1 will be inhibited from further binding to the immobilize SDE1 in the wells, which are then washed away in subsequent steps. The theoretical maximum optical absorbance for the ICI-ELISA will be when the antigen concentration in the sample is zero during the pre-incubation of the primary antibody solution with the sample where there are no inhibited pAbs-anti-SDE1. Thus, optical absorbance will decrease with increasing concentration of SDE1 antigens in the samples.

We used the aforementioned ICI-ELISA for testing the specificity of the pAb-anti-SDE1 in the presence of a complex sample matrix, namely phloem extracts of various citrus varieties. We tested samples of healthy phloem extracts (negative controls), healthy phloem extracts spiked with various concentrations of SDE1 (positive calibration samples), and phloem extracts samples of infected plants (verified by PCR). Using indirect ELISAs and ICI-ELISAs for initial interference and sensitivity testing will allow us to identify and address platform-independent issues and parameters, which will then be adapted for later biosensor development. For example, ELISAs can be used to identify any specific pre-

treatment of phloem extract samples for removal of interfering substances, while maintaining overall assay performance.

3.3 Materials and Methods

3.3.1   Materials

All materials and chemicals were purchased from Fisher Scientific unless specified otherwise. AminoLink™ Plus Coupling Resin was purchased from Thermo Fisher Scientific Inc. (United States). Affinity chromatography columns, Nonfat dry milk powder (NFDM), and polyethylene glycol sorbitan monolaurate (Tween 20) were purchased from Bio-Rad Laboratories (Hercules, CA). Prepacked PD-10 desalting/buffer exchange column with Sephadex G-25 resin were purchased from GE Healthcare Life Sciences (Pittsburgh, PA). BrandTech™ BRANDplates immunoGrade™ 96-Well Microplates (Thermo Fisher Scientific Inc., United States) were used for all ELISAs. ELISA blocking buffer was prepared with 3% NFDM in 1X PBS at pH 7.4. ELISA reaction buffer was prepared with 3% NFDM, 0.05% Tween-20 in 1X PBS at pH 7.4. ELISA wash buffer was prepared with 0.05% Tween-20 in 1X PBS pH 7.4. SDE1 recombinant proteins were provided by the Ma Lab[1].

3.3.2   Indirect ELISA for Evaluation of Antisera and Affinity Purified Antibodies

100 μL of SDE1 antigens were coated overnight at 4°C onto each ELISA well at 1 μg/mL in 1X PBS. After washing plates with ELISA wash buffer, plates were blocked with 300 μL per well with ELISA blocking buffer for 2 hours at ambient condition. Plates were then washed with ELISA wash buffer. Antisera samples or affinity purified

antibodies were serially diluted in ELISA reaction buffer and incubated with each designated ELISA well in triplicates for 1 hour at room temperature. After washing the microplate with ELISA wash buffer, we proceeded to incubate secondary goat-anti-Rabbit-IgG-HRP conjugates at 1:5000 dilution in ELISA reaction buffer onto each ELISA well for 30 minutes at room temperature. Plates were then washed with ELISA wash buffer before incubation with 100 μL of ABTS solution for color development for 15 minutes. Absorbance reading at 405 nm were obtained using a BioTek microplate reader after color development.

3.3.3   Affinity Purification of Anti-SDE1 Antibodies

Using the SDE1 recombinant antigens produced from the Ma Lab, we performed the affinity purification to obtain purified antibodies against SDE1 using the Amino-Link Plus coupling resin from ThermoFisher Scientific, Inc. Following the standard protocol for affinity purification from the manufacturer, we covalently immobilized the antigen proteins to the resin matrix, followed by incubation with the antisera for 1 hour at room temperature with end-to-end mixing to allow for the specific antibodies to bind to the immobilized SDE1 antigens in the resin column. Repeated washing of the column with 1X phosphate buffered saline (1X PBS) allows for removal of unbounded molecules while retaining specifically bound antigen-antibody complexes. Finally, we eluted the specifically bound antibodies with a 0.1 M glycine-HCl buffer (pH 3). Immediately, we neutralized the eluted antibodies with 0.5 M phosphate buffer pH 9.0, followed by concentrating the proteins a higher concentration with centrifugal concentrators. We then buffer exchanged the antibodies into 1X PBS pH 7.4 using prepacked PD-10 columns with

Sephadex G-25 resin. Next, we evaluated the purity of the antibodies using standard SDS-PAGE.

3.3.4   Citrus Plant Sample Preparation

Healthy (negative control) and real citrus plant tissue samples were provided by the Ma Lab. Briefly, stem samples from young branches were cut into small sections and grounded to fine powder following the protocols from Pagliaccia et al.[1]. Grounded tissue was then suspended in 1X PBS at 1 g/mL and vortexed to mix. We then obtained the supernatants by centrifuging the suspensions at 13,800 x g. Supernatants were diluted 1:1 in adjusted ELISA reaction buffer (6% NFDM, 0.1% Tween-20 in 1X PBS) and immediately used as samples for ELISAs.

3.3.5   Indirect Competitive Inhibition ELISA

100 µL of SDE1 antigens were coated overnight at 4°C onto each ELISA well at 1 µg/mL in 1X PBS. After washing plates with ELISA wash buffer, plates were blocked with 300 µL per well with ELISA blocking buffer for 2 hours at ambient condition. Plates were then washed with ELISA wash buffer. Antigen-spiked samples and real citrus tissue samples prepared in ELISA reaction buffers were incubated in separate reaction microtubes with 100 ng/mL of purified anti-SDE1 antibody for 1 hour. 100 µL of the sample-antibody mixture were then incubated with each designated ELISA well in triplicates for 1 hour at room temperature. After washing the microplate with ELISA wash buffer, we proceeded to incubate secondary goat-anti-Rabbit-IgG-HRP conjugates at 1:5000 dilution in ELISA reaction buffer onto each ELISA well for 30 minutes at room temperature. Plates were then washed with ELISA wash buffer before incubation with 100 µL of ABTS solution for

color development for 15 minutes. Absorbance reading at 405 nm were obtained using a BioTek microplate reader after color development.

3.4 Results and Discussion

3.4.1   Evaluation of Antisera and Affinity Purification of Anti-SDE1 Antibodies

Evaluation of multiple antisera samples by indirect ELISA showed high endpoint antibody titers between 1:125000 and 1:625000 dilution factor with absorbance values greater than blank controls as shown in figure 3.2[7,8]. Antibody endpoint titers greater than 1:100000 is considered a good sign of immune response from the animal for further antibody purification[7]. Consequently, we proceeded with pooling these bleeds for affinity antibody purification of the rabbit antisera. SDS-PAGE performed on the affinity purified antibodies showed distinct bands around 25 kDa and 50 kDa, for the light and heavy chains of the IgG molecules, respectively (Figure 3.3) which indicates adequate purity and absence of other protein-based impurities[2,9]. The purified antibodies are expected to be of the isotype immunoglobulin G (IgG)[10].
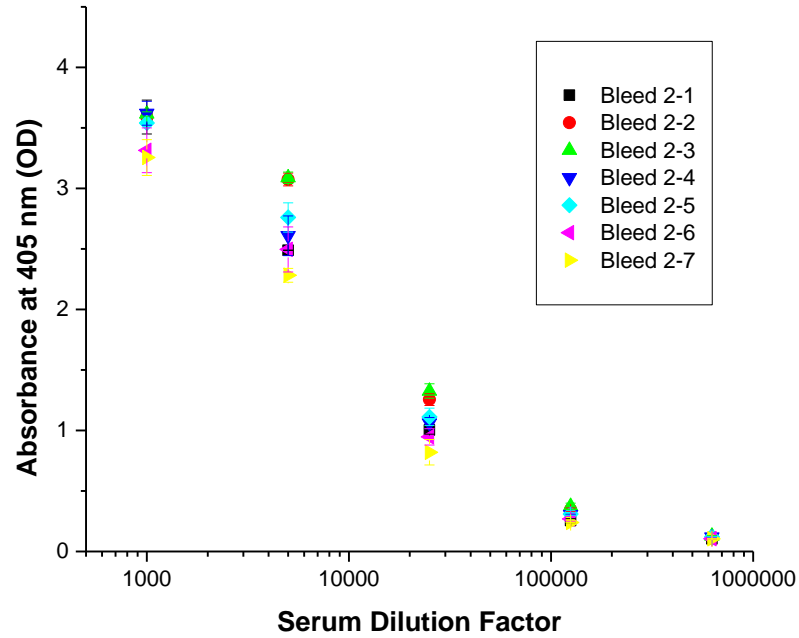
Figure 3.2*: Indirect ELISA results of antiserum samples to determine which antisera to continue affinity purification for anti-SDE1 antibodies. Antisera were diluted by 1000, 5000, 25000, 125000, and 625000 times. Results for each data point was obtained from in duplicate wells.*
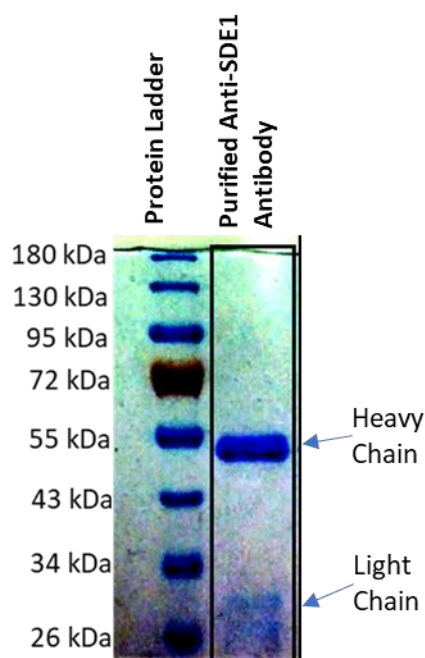
Figure 3.3*: SDS-PAGE results for affinity purified anti-SDE1 antibodies showed bands at 25 kDa and 50 kDa for the light and heavy chains of the purified IgGs, respectively.*

3.4.2 Characterization of Purified of Anti-SDE1 Antibodies by Indirect ELISA and Indirect Competitive Inhibition ELISA

Indirect ELISAs using the serially diluted concentrations of affinity purified pAbs-anti-SDE1 yielded the expected dose-response behavior for receptor-binding assays as modeled with a 4-parameter logistic regression using OriginPro 9 Software as shown in figure 3.4[11,12]. The concentration range of antibodies needed to bind to the immobilized antigen and yield the detectable signal is from around $10^1 - 10^2$ ng/mL (or $10^{-11} - 10^{-10}$ M) suggesting that the purified antibodies have high affinity to the immobilized SDE1 antigens coated onto the ELISA well. Furthermore, the response at 100 ng/mL of anti-SDE1 pAb concentration was selected as the optimum antibody concentration for further ICI-ELISAs.

As shown in Figure 3.5, ICI-ELISAs performed with pure antigens spiked into ELISA reaction buffer and preincubated with 100 ng/mL of anti-SDE1 pAbs yielded less than 1 nM detection limit of the SDE1 antigens in solution as calculated from 3 standard deviations from the blank, $A_{405} = 3.53 \pm 0.18$. The ELISA showed the expected dose-response behavior as modeled with a 4-parameter logistic regression[11,12]. Next, we performed ICI-ELISAs with artificially spiked phloem extracts with various concentrations of SDE1 from navel orange and from grapefruit citrus varieties. Results suggested some possible interference effects of the phloem extracts on the antigen-antibody interactions compared to antigens in ELISA reaction buffer only; however, the overall response curves for assays with both spiked navel orange and grapefruit retained their sigmoidal shape with a decrease in sensitivity as observed by a horizontal shift to the right relative to the response curve for antigens in ELISA reaction buffer only.

Indirect Capture ELISA for Purified Anti-SDE1 Antibody

Model	Logistic		
Equation	y = A2 + (A1-A2) /(1 + (x/x0)^p)		
Reduced Chi-Sq	0.00134		
Adj. R-Square	0.99939		
		Value	Standard Erro
	A1	0.01194	0.02003
	A2	3.95009	0.06577
	x0	164.9932	8.966
Absorbance at 405 nm	p	1.014	0.04473
	EC20	42.04557	2.28572
	EC50	164.9932	8.966
	EC80	647.4589	65.46615
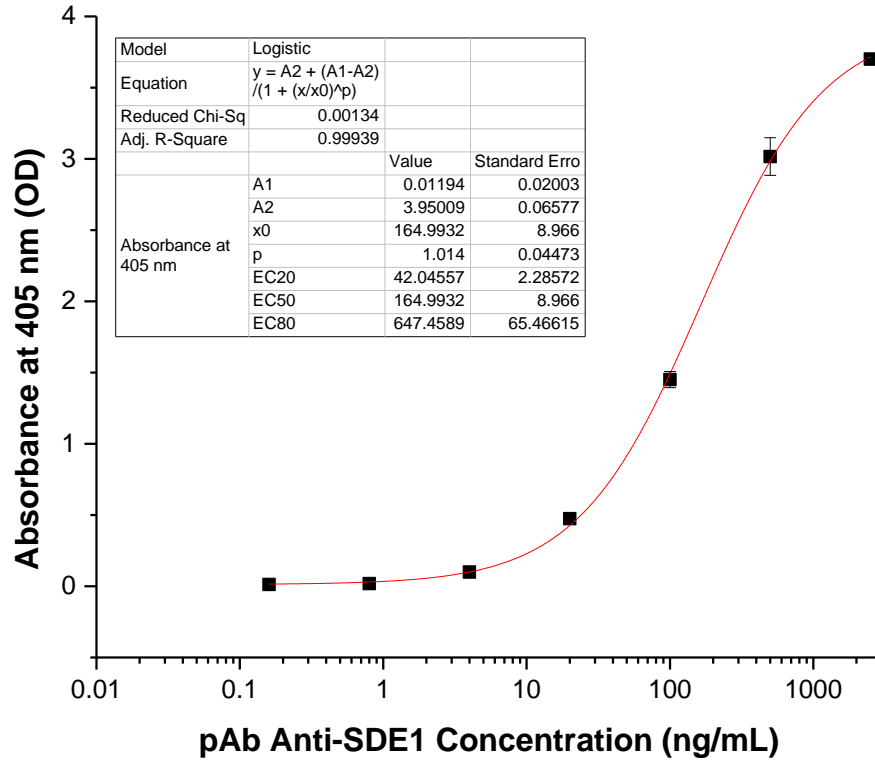
Figure 3.4*: Indirect capture ELISA for evaluating sensitivity of purified anti-SDE1 polyclonal antibodies. 4-parameter logistic model was fitted to the data as shown by the red line. Results for each data point was obtained from in triplicate wells (n =3). Inset table shows the equation and calculated variables from regression analysis.*

Indirect Competitive Inhibition ELISA for SDE1 in 1X PBS

Model	Logistic		
Equation	$y = A2 + (A1-A2)/(1 + (x/x0)^p)$		
Reduced Chi-Sqr	0.54717		
Adj. R-Square	0.99661		
		Value	Standard Error
	A1	3.42211	0.07532
	A2	0.31294	0.0661
	x0	4.05771	0.52485
Absorbance at 405 nm	p	0.91489	0.09605
	EC20	0.89168	0.18546
	EC50	4.05771	0.52485
	EC80	18.46508	3.73048

Blank: $\Delta R/R_i = 3.53 \pm 0.18$

LOD = <1 nM SDE1

At $3*SD_{Blank}$ ($\Delta R/R_i = 2.99$)

n = 3 replicates per concentration
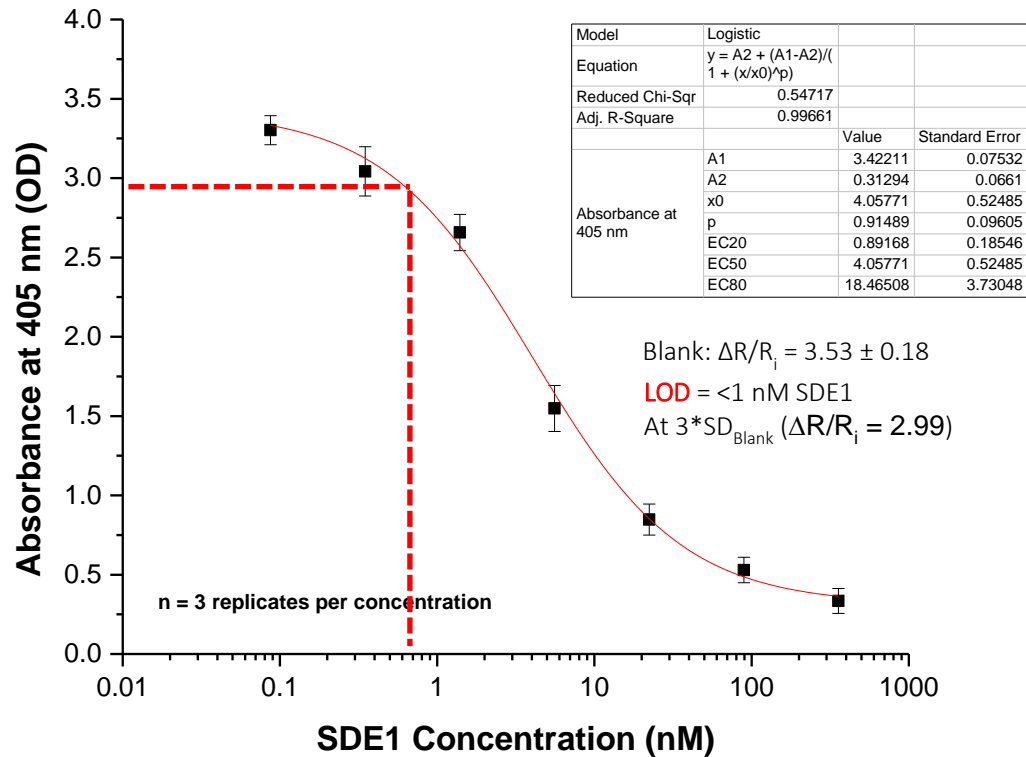
Figure 3.5*: Indirect competitive inhibition ELISA with SDE1 antigens spiked into ELISA reaction buffer. SDE1-spiked samples were pre-incubated with 100 ng/mL of anti-SDE1 antibodies before adding the mixture to ELISA well with immobilized SDE1 antigens. Results for each data point was obtained from in triplicate wells (n =3). 4-parameter logistic model was fitted to the data as shown by the red line. Inset table shows the equation and calculated variables from regression analysis.*
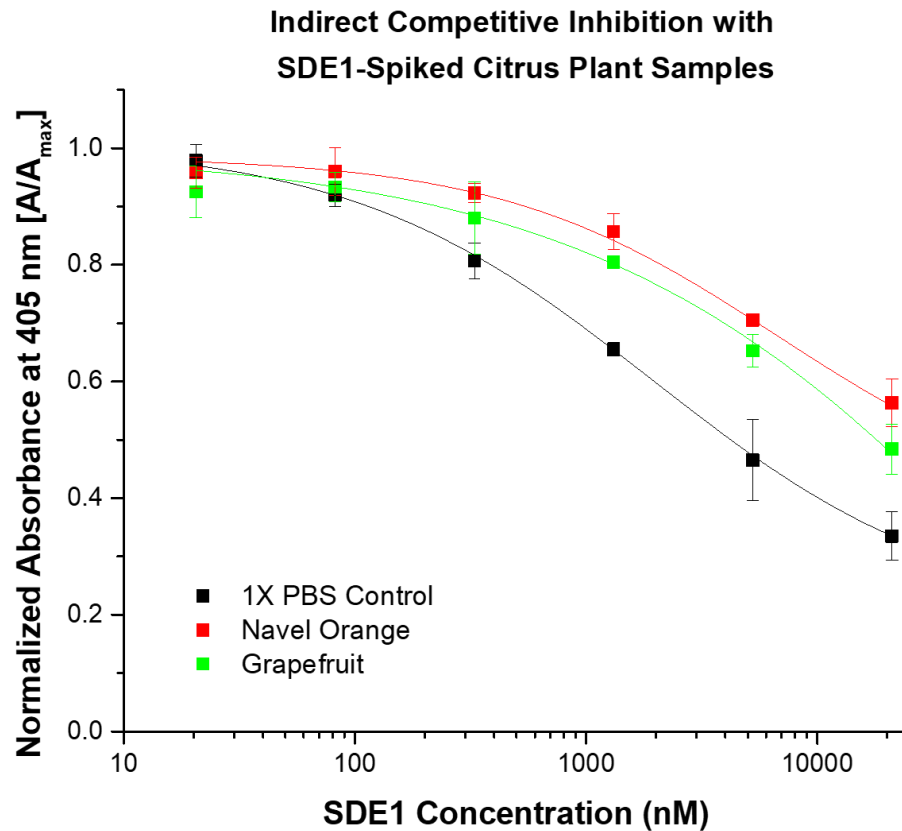
Figure 3.6: *Indirect competitive inhibition ELISA testing of samples of SDE1 spiked into healthy phloem extracts from navel orange and grapefruit varieties. SDE1-spiked samples were pre-incubated with 100 ng/mL of anti-SDE1 antibodies before adding the mixture to ELISA well with immobilized SDE1 antigens. Results for each data point was obtained from in triplicate wells (n =3). Absorbance values were normalized to the maximum absorbance for each data set. 4-parameter logistic model was fitted to the data as shown by the solid lines. Inset table shows the equation and calculated variables from regression analysis.*

3.4.3   Evaluation of Real Infected Citrus Plant Samples with Anti-SDE1 Antibodies

by ICI-ELISA

For this set of experiments, to account for batch-to-batch variation of purified anti-

SDE1 polyclonal antibodies, calibration curves were obtained by spiking SDE1 antigens

at various concentrations into ELISA reaction buffer only and into healthy grapefruit tissue

(mixed 1:1 with adjusted ELISA reaction buffer). These standards were then pre-incubated with 100 ng/mL of anti-SDE1 antibodies in separate microtubes for 1 hour prior to adding the sample-antibody mixture to designated ELISA wells (previously immobilized with SDE1 antigens). As shown in figure 3.7, both calibration curves showed dose-response behavior with decreasing absorbance as SDE1 concentration increased. Data points were also fitted to a 4-paramter logistic regression model as recommended for immunoassays[12]. We calculated the limit of detection (LOD = 3 S.D. from zero antigen concentration) using the calibration curve from the grapefruit phloem extract, to be 22 nM (Absorbance ~ 0.8 OD).

Standard Curves for SDE1

Absorbance at 405 nm (OD) (y-axis)

SDE1 Concentration (nM) (x-axis)

Legend: ■ 1X PBS ● Grapefruit

Model	Logistic		
Equation	$y = A2 + (A1-A2)/(1 + (x/x0)^p)$		
Reduced Chi-Sqr	0.40987	3.47996	
Adj. R-Square	0.99568	0.99394	
		Value	Standard Error
1X PBS Standards [Absorbance at 405 nm]	A1	1.44787	0.03807
	A2	0.18348	0.02517
	x0	39.23839	3.6593
	p	1.56547	0.19581
	EC20	16.18538	2.50405
	EC50	39.23839	3.6593
	EC80	95.12605	12.76116
Grapefruit Standards [Absorbance at 405 nm]	A1	1.25889	0.0418
	A2	0.307	0.07929
	x0	26.86621	8.46382
	p	0.87535	0.19767
	EC20	5.5133	2.27805
	EC50	26.86621	8.46382
	EC80	130.91866	69.71558

Figure 3.7*: Standard curves for SDE1 obtained by indirect competitive inhibition ELISA for SDE1 spiked into 1X PBS and healthy grapefruit plant tissue extracts. Results for each data point was obtained from in triplicate wells (n =3). 4-parameter logistic model was fitted to the data as shown by the solid lines. Inset table shows the equation and calculated variables from regression analysis.*

ICI-ELISA was performed using 6 known negative plant samples and 10 known positive samples. Samples were obtained from grapefruit trees in Texas and all experiments using real samples were conducted in the USDA-compliant Ma Lab at UCR. From the data set in Table 2.1 for known positive samples, qPCR count values did not show correlation with measured absorbance from ELISA (Correlation Coefficient, R = 0.09484). We used the modified Thompson tau technique to remove outliers from readouts of triplicate ELISA wells of each sample[13]. This method was used to minimize biased removal of outliers.

Averaged absorbance values for each set of known positives (True positives) and known negatives (True negatives) were then used in a Two-Sample Assuming Unequal Variances t-Test (alpha = 0.05, df = 8). Statistical analysis using MS-Excel showed significant difference in absorbance values between negative and positive samples (P(T<=t) one-tail = 0.007, P(T<=t) two-tail = 0.014).   Further analysis using Receiver Operating Characteristic (ROC) method was used to determine optimal cutoff range to be from 0.8 OD to 0.85 with Sensitivity = 1 and Specificity = 0.67 (as shown in figure 3.8). The area under the curve (AUC) of the ROC curve was calculated to be 0.875, which is considered acceptable based on standards from medical diagnostics perspective[14–16].

	Positive Sample ID	qPCR Results (ct)	Average Absorbance (OD)	STDEV
Known Negative Samples	**KN4 S636**	Not Provided	0.872	0.030
	KN14 S209	Not Provided	0.994	0.057
	KN2 S871	Not Provided	0.910	0.002
	KN10 S706	Not Provided	0.728	0.078
	KN18 S436	Not Provided	0.676	0.023
	KN11 S399	Not Provided	0.857	0.000
Known Positive Samples	**KP40 S011**	23.6	0.795	0.173
	KP5 S547	25.9	0.730	0.129
	KP16 S614	33	0.703	0.081
	KP6 S021	23.4	0.619	0.120
	KP17 S894	27.9	0.567	0.016
	KP6 S316	23.4	0.567	0.134
	KP14 S039	26.6	0.701	0.136
	KP31 S028	24.3	0.670	0.142
	KP9 S386	24.4	0.611	0.120
	KP32 S840	25.3	0.740	0.118

Table 2.1*: Data table of healthy and infected grapefruit plant tissue samples analyzed by qPCR and ICI-ELISAs. The modified Thompson tau technique was used to remove outliers from readouts of triplicate ELISA wells of each sample.*

t-Test: Two-Sample Assuming Unequal Variances		
	Neg. Samples	*Pos. Samples*
Mean	0.839356	0.670193
Variance	0.013928	0.005969
Observations	6	10
Hypothesized Mean Difference	0	
df	8	
t Stat	3.131396	
P(T<=t) one-tail	0.006993	
t Critical one-tail	1.859548	
P(T<=t) two-tail	0.013986	
t Critical two-tail	2.306004	

Table 2.2*: Statistical analysis of ICI-ELISA results on real infected and healthy phloem extract samples, showing significant difference in absorbance signals.*

Receiver Operating Characteristic (ROC) Curve

AUC = 0.875
Optimal Cutoff 0.80 OD to 0.825 OD
(Sensitivity = 1, Specificity = 0.67)
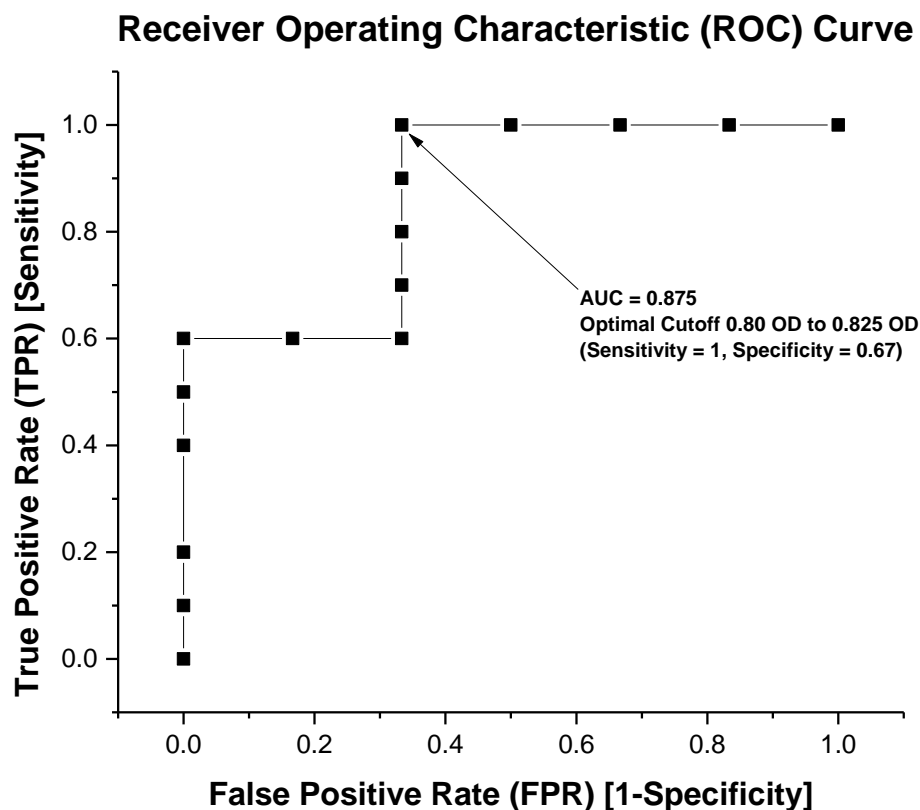
Figure 3.8: Receiver operator characteristic curve for indirect competitive inhibition ELISA performed on 10 infected grapefruit samples and 6 health negative control samples.

3.5 Conclusion

This work demonstrated the feasibility of an antibody for specific detection of SDE1 biomarkers for HLB as corroborated by our published work[1]. The strategy to select rabbit antisera with high antibody titers for further affinity antibody purification yielded polyclonal antibodies with high affinity towards the SDE1 antigen and allowed for reliable and complex immunoassays. These purified antibodies have been used in ELISAs for investigating matrix and interference effects on antigen-antibody interactions from spiked healthy plant samples. Despite some interference from plant tissue extracts, the developed

70

ICI-ELISAs based on the purified anti-SDE1 antibodies were still able to show dose-response to SDE1 antigens in plant samples. Furthermore, we demonstrated the ability of the anti-SDE1 antibodies to distinguish between 10 samples of real infected grapefruit plants and 6 (healthy) negative control samples. This ELISA platform using purified anti-SDE1 antibodies and the SDE1 antigens discovered by the Ma Lab further serves as a technique for additional efforts for validation of SDE1 biomarkers and antibodies by testing on greater numbers of real HLB-diseased plant samples using current ELISA platform. While ELISA is a cumbersome assay method requiring significant operator experience, instrumentation, and longer processing time, the method is scalable for point-of-laboratory and high-throughput testing.

Within the scope of this dissertation research, this work served to provide the necessary anti-SDE1 antibody reagents needed for the development of electronic biosensors based on carbon nanomaterials. More specifically, to confer specificity and sensitivity for our affinity-based biosensor to the HLB protein biomarker, the biosensor will be subsequently functionalized with biorecognition molecules such as antibodies generated against the protein biomarker[17]. The antibodies have also been tested under various simulated plant sample matrices to determine potential risks of cross-reactivity and interference effects. The ELISAs developed in this work provides the standard performance criteria for comparison with our biosensor system in the future works.

3.6 References

1.   Pagliaccia, D. *et al.* A Pathogen Secreted Protein as a Detection Marker for Citrus Huanglongbing. *Frontiers in Microbiology* **8,** (2017).

2.   Ayyar, B. V., Arora, S., Murphy, C. & O'Kennedy, R. Affinity chromatography as a tool for antibody purification. *Methods* **56,** 116–129 (2012).

3.   Aydin, S. A short history, principles, and types of ELISA, and our laboratory experience with peptide/protein analyses using ELISA. *Peptides* **72,** 4–15 (2015).

4.   Gan, S. D. & Patel, K. R. Enzyme Immunoassay and Enzyme-Linked Immunosorbent Assay. *Journal of Investigative Dermatology* **133,** 1–3 (2013).

5.   Watanabe, E., Miyake, S. & Yogo, Y. Review of Enzyme-Linked Immunosorbent Assays (ELISAs) for Analyses of Neonicotinoid Insecticides in Agro-environments. *J. Agric. Food Chem.* **61,** 12459–12472 (2013).

6.   Overview of ELISA. Available at: http://www.piercenet.com/method/overview-elisa. (Accessed: 5th November 2014)

7.   Frey, A., Di Canzio, J. & Zurakowski, D. A statistically defined endpoint titer determination method for immunoassays. *Journal of Immunological Methods* **221,** 35–41 (1998).

8.   Miura, K. *et al.* Development and Characterization of a Standardized ELISA Including a Reference Serum on Each Plate to Detect Antibodies Induced by Experimental Malaria Vaccines. *Vaccine* **26,** 193 (2008).

9.   Charles A Janeway, J., Travers, P., Walport, M. & Shlomchik, M. J. The structure of a typical antibody molecule. *Immunobiology: The Immune System in Health and Disease. 5th edition* (2001).

10.   Schroeder, H. W. & Cavacini, L. Structure and function of immunoglobulins. *Journal of Allergy and Clinical Immunology* **125,** S41–S52 (2010).

11.   Findlay, J. W. A. & Dillard, R. F. Appropriate calibration curve fitting in ligand binding assays. *AAPS J* **9,** E260–E267 (2007).

12.   O'Connell, M. A., Belanger, B. A. & Haaland, P. D. Calibration and assay development using the four-parameter logistic model. *Chemometrics and Intelligent Laboratory Systems* **20,** 97–114 (1993).

13.   Shen, Q. & Yang, R. Thompson-Tau Outlier Detection Method for Detecting Abnormal Data of Listed Pharmaceutical Companies in China. in *2015 8th International Symposium on Computational Intelligence and Design (ISCID)* **1,** 379–382 (2015).

14.   Hajian-Tilaki, K. Receiver Operating Characteristic (ROC) Curve Analysis for Medical Diagnostic Test Evaluation. *Caspian Journal of Internal Medicine* **4,** 627 (2013).

15.   Obuchowski, N. A. & Bullen, J. A. Receiver operating characteristic (ROC) curves: review of methods with applications in diagnostic medicine. *Phys. Med. Biol.* **63,** 07TR01 (2018).

16.   Zou, K. H., O'Malley, A. J. & Mauri, L. Receiver-Operating Characteristic Analysis for Evaluating Diagnostic Tests and Predictive Models. *Circulation* **115,** 654–657 (2007).

17.   Tran, T.-T. & Mulchandani, A. Carbon nanotubes and graphene nano field-effect transistor-based biosensors. *TrAC Trends in Analytical Chemistry* **79,** 222–232 (2016).

Chapter 4

A Reduced Graphene Oxide-Based Chemiresistive Biosensor for Detection of Secreted Protein Biomarker for Citrus Greening Disease

4.1 Abstract

Citrus greening disease, also known as Huanglongbing (HLB), is posing a worldwide threat to the multi-billion dollars citrus industry. Currently, there are no cures for infected plants while containment of the spread of disease is heavily dependent on early detection of infected hosts for quarantine. The pathogen responsible for causing the disease is the bacteria *Candidatus* Liberibacter. Here, we report a label-free chemiresistive biosensor based on carbon nanomaterials for quantitative detection of HLB biomarkers through detection of targeted proteins secreted by *Ca*. Liberibacter. These secreted proteins can systematically distribute in the infected trees, which affords reliable and selective diagnosis of infected plants. Using these biomarkers, we have generated custom polyclonal antibodies which were then used to functionalize our biosensors for specific detection of HLB biomarkers. The nanobiosensor is a chemiresistor, which takes advantage of the semiconducting properties of reduced graphene oxide (RGO) platelets. Binding of analytes to the antibodies immobilized on the surface of RGO platelets lead to changes in the local electrostatic environment and consequently leads to proportionate modulation of electrical resistance/conductance of the nanomaterials and the sensing device.

4.2 Introduction

Citrus greening disease, also known as Huanglongbing (HLB) disease, is posing a worldwide threat to the multi-billions dollar industry[1]. The pathogens responsible for HLB are believed to be attributed to three *Candidatus* Liberibacter species: *Candidatus* Liberibacter asiaticus (*C*Las), *Candidatus* Liberibacter africanus (*C*Laf), and *Candidatus* Liberibacter americanus (*C*Lam) which reside in the phloem of infected plants upon inoculation by insect vectors[1,2]. *Ca*. Liberibacter spp. is primarily transmitted by phloem-feeding Asian citrus psyllids, *Diaphorina citri* Kuwayama[1–3]. The focus of this work on detection of the *C*Las species since *C*Las is the only species with global distribution, especially in major citrus growing areas[1,2]

Since there are no cures for trees affected with HLB disease, management of the spread of the disease is focused on removal of the pathogens via eradication of infected trees and vectors[3]. Thus, timely and accurate detection of infected plants is crucial for disease management; however, detection methods based on disease symptoms and nucleic-acid assays remain unsuccessful. Symptoms-based and qualitative diagnosis of infected plants lack accuracy due to variable latency of symptoms and due to similarities of symptoms with other citrus diseases and nutrient deficiency[2].

Assays for detection of nucleic acid-based biomarkers of *Ca*. Liberibacter suffer from high rates of false negatives due to uneven distribution of the pathogen in infected plants[4,5]. Additionally, nucleic acid-based assays suffer from complex sample preparation requirement, high costs, time-consuming processes, making these tools prohibitive for disease management, especially when multiple samples need to be tested from one tree[2].

Therefore, detection of secreted protein-based biomarkers, SDE1, for *C*Las addresses the performance requirements for accuracy, speed, robustness, and portability. Compared to the *C*Las bacteria, the secreted proteins are more evenly and systematically distributed throughout the infected trees and consequently eliminate the need for multiple sampling sites per tree[3]. Uniform distribution of the biomarker further affords reliable and selective diagnosis of infected plants by reducing false negatives due to sampling challenges[5]. Using SDE1 protein antigen, we have generated custom polyclonal antibodies which were then used to functionalize the reduced graphene oxide (RGO) transducing elements of our biosensors for specific detection of HLB biomarkers.

RGO is electrically semiconducting in nature making it a potential candidate as an electrical transducer for biosensing applications[6,7]. RGO sheets or platelets are graphene-based nanomaterials that have been chemically oxidized and exfoliated from highly ordered pyrolytic graphite, yielding graphene oxide (GO) flakes, which are subsequently reduced via various chemical, electrochemical, and thermal methods to RGO[8–10]. Reduction of GO to RGO is essential for restoring some of the original electrical, chemical, and structural properties found in pristine graphene sheets. For example, depending on the method(s) of reduction, RGO can regain some of the following properties found in pristine graphene sheets: (1) semiconducting nature, (2) reduction of oxide groups, and/or (3) restoration of sp2 bond structures[11]. Additionally, individual RGO platelets are considered to be 2-dimensional nanomaterials consisting of single and up to few layers of RGO sheets[7,8]. Thus, RGO produced from chemically exfoliated graphite followed by reduction

provides an attractive electrical transduction nanomaterial for biosensing applications due to the electrical, chemical, and structural properties as well as the scalability for production.

Herein, we describe the development of a chemiresistive immunosensor that takes advantage of the semiconducting properties of reduced graphene oxide (RGO) for the detection of a secreted protein biomarker, SDE1, for HLB. To our knowledge, this report is the first demonstration of a rapid assay method for the detection of a secreted protein-based biomarker for citrus greening disease. This biosensor provides a viable analytical tool for the citrus industry for management of HLB.

4.3 Materials and Methods

4.3.1   Reagents & Materials

All materials and chemicals were purchased from Fisher Scientific unless specified otherwise. Recombinant HLB biomarker, SDE1, and rabbit antisera for the antigen were obtained from Dr. Wenbo Ma's laboratory at the University of California-Riverside. Anti-HLB polyclonal antibodies were obtained by affinity- purification of antisera of rabbits that were immunized with SDE1 proteins. 95% 3-Aminopropyl)-triethoxysilane (APTES), 1-Pyrenebutyric acid N-hydroxysuccinimide ester (95%) (PBASE), anhydrous N,N-dimethylformamide (DMF), and ethanolamine were obtained from Sigma Aldrich (St. Louis, Mo, USA). Graphene oxide 5 mg/mL in water suspension was purchased from Stanford Advanced Materials (Irvine, CA, USA). Tween-20 was obtained from Bio-Rad (Irvine, CA, USA). Graphene oxide suspensions, 5 mg/mL in water, were purchased from Stanford Advanced Materials (Lake Forest, CA, USA).

4.3.2 Device Fabrication

We used photolithography and lift-off process for patterning of gold interdigitated microelectrodes onto Si/SiO$_2$ wafer in the cleanroom at the Center for Nanoscale Science and Engineering, University of California, Riverside. Briefly, we deposited 300 nm of SiO$_2$ onto p-doped Si wafer using chemical vapor deposition (CVD). Next, we used photolithography to define microelectrodes with 200 µm by 200 µm cross sectional area and 3 µm gaps as shown in figure 4.1. We then used e-beam evaporation to deposit 20 nm of a Cr adhesion layer and 180 nm of Au. Finally, we used acetone to remove excess photoresist and Cr-Au layers, leaving multiple patterns of the microelectrodes. After cutting individual chips from the wafers, we cleaned the chips with piranha solution (75 vol% H$_2$SO$_4$; 25 vol% H$_2$O$_2$) for 30 minutes, followed by rinsing with deionized (DI) water, then dried under a stream of nitrogen.
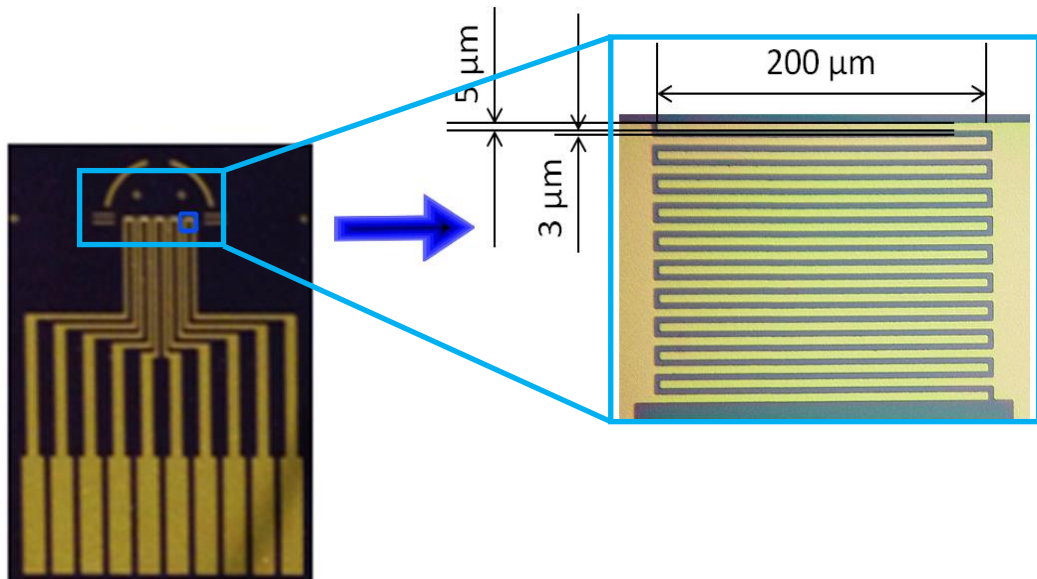
Figure 4.1: *Optical micrographs of fabricated interdigitated microelectrodes on SiO$_2$/Si substrate with 200 µm by 200 µm cross sectional area and 3 µm gaps. E-beam evaporation was used to deposit 20 nm of a Cr adhesion layer and 180 nm of Au.*

Next, we incubated the device with APTES for 1 hour followed by washing with DI H$_2$O and drying with nitrogen. We sonicated a solution of 0.05 mg/mL of GO in a water bath for 1 minute. We then drop-casted the GO solution onto the microelectrode area and incubated it for 1 hour. Excess GO was washed off with DI water, and the device was dried under nitrogen. We electrochemically reduced the GO in the microelectrode area using a three-electrode cell on the CH Instrument (CHI) with an Ag/AgCl reference electrode, a titanium counter electrode, and the source and drain electrodes connected as the working electrodes. We performed a linear voltage sweep at the working electrodes from 0 V to -1.6 V at 100 mV/s scan rate for six cycles in 1X PBS (10 mM phosphate buffer, pH 7.4, 150 mM NaCl). The device with the RGO was then washed with DI water, dried under nitrogen, and annealed in a tube furnace for 1 hour at 250°C.

To functionalize the RGO surface with anti-SDE1 antibodies, we incubated the RGO device with 3 mg/mL of PBASE linker in DMF for 1 hours. The excess PBASE linker was washed off using DMF, followed by drying with nitrogen. Next, we drop-casted 25 µL of the antibodies at 0.05 mg/mL in 10 mM phosphate buffer, pH 7.4 onto the PBASE-functionalized microelectrode area, followed by overnight incubation at 4°C. The unreacted PBASE was then quenched with 100 mM ethanolamine, pH 8.0 for 1 hour. The remaining exposed RGO surfaces was subsequently blocked by incubating the chip with 0.1% w/v Tween-20 in 10 mM phosphate buffer, pH 7.4 for 1 hour. The functionalized biosensor area was washed with 10 mM phosphate buffer.

4.3.2 Biosensing Protocol:

To perform the assays using the biosensor, we monitored the percent change in resistance 100% * $(R_f - R_i)/R_i$ of the final resistance (R_f) and the initial resistance (R_i) at each sample condition for each device by measuring the source-drain current (I_{SD}) as a function of source-drain voltage (V_{SD}) using a CHI electrochemical analyzer. The I-V curve is obtained from each set of measurement. We then took the inverse of the slope of the I-V curve to calculate the resistance values. To test the biosensor with a sample, we incubated the sensor with 25 µL of the sample for 30 minutes at room temperature, followed by washing off the excess volume with 10 mM phosphate buffer, and performing I-V measurements in 25 µL 10 mM phosphate buffer from -0.1 to 0.1 V at 100 mV/s scan rate using a CH Instrument.

4.4   Results and Discussion

We used RGO as the signal transduction element of the chemiresistor by fabricating the semiconducting channel using self-assembled RGO platelets which physically and electrically connect the source and drain electrodes. Graphene oxide (GO) was first self-assembled via electrostatic interactions with (3-Aminopropyl)trimethoxysilane-functionalized (APTES) SiO_2 surface across the source and drain electrodes. Positively charged protonated amines from APTES attract negatively charged oxide groups on GO to the device surface (Figure 4.2). We then electrochemically reduced GO to RGO using a previously reported method which allowed us to restore semiconducting property to RGO[12,13]. By functionalizing the RGO surface with antibodies for HLB biomarkers, we conferred specificity to the biosensor. The remaining exposed RGO surfaces were

physisorbed with surfactant molecules to inhibit nonspecific binding of analytes and parasitic species on the RGO transducer surface.
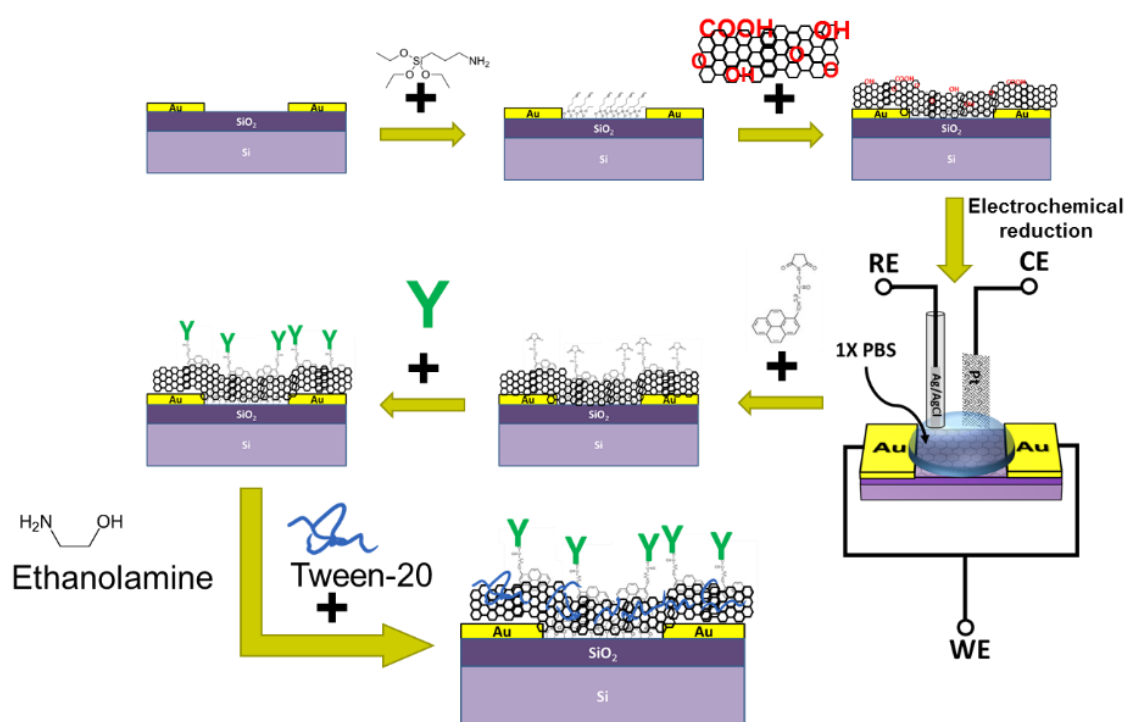
Figure 4.2*: Schematic diagram illustrating fabrication and functionalization process for rGO-based devices. Surface functionalization of interdigitated microelectrodes with RGO and anti-SDE1 antibodies. We first reacted SiO₂ surface with APTES to provide positively charged amine groups to electrostatically attract negatively charged GO platelets to the sensor surface. We then electrochemically reduced GO to RGO to partially restore semiconductivity to the material. Next, we functionalized RGO surfaces with the heterobifunctional linker, 1-Pyrenebutyric acid N-hydroxysuccinimide ester (PBASE), via π- π stacking of pyrene groups onto RGO. We then allowed the primary amines on anti-SDE1 antibodies to react with the N-hydroxysuccinimide (NHS) ester groups to form stable amide bonds, and thus covalently immobilized the antibodies onto the sensor surface. The remaining RGO surfaces were further blocked with Tween-20 surfactant molecules to prevent any nonspecific binding during assays.*

4.4.1 Device Characterization

Linear sweep voltammograms shown in figure 4.3 suggested complete electrochemical reduction of GO as seen by the loss of the reduction peak at -0.6 V with sequential scans[13]. Scanning electron microscopy (SEM) studies showed that GO platelets self-assembled onto APTES-functionalized SiO_2 surface, forming the RGO channel (FIG. 1). The diameter of RGO platelets ranged from 0.5 µm to 2.0 µm.
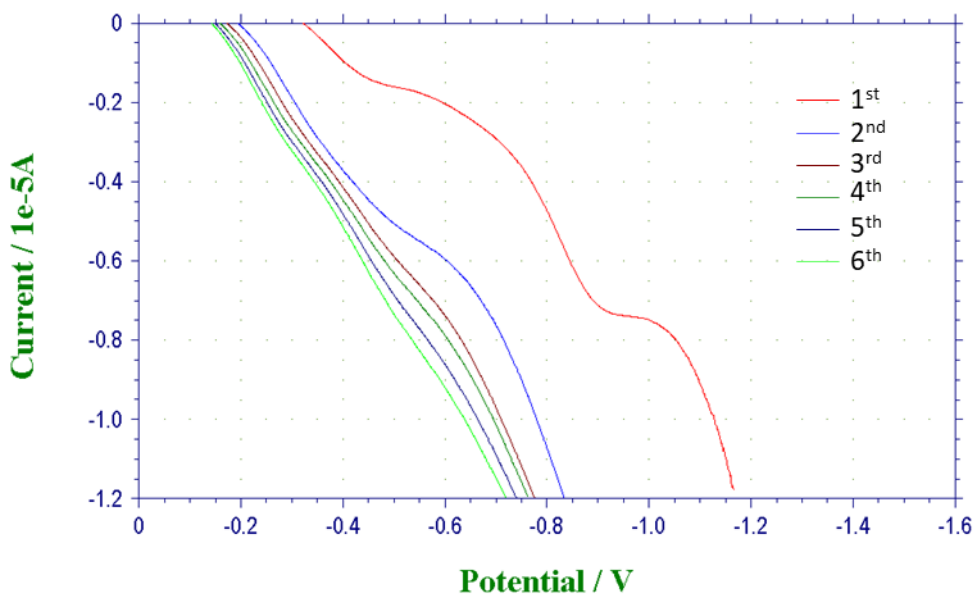
Figure 4.3*: Linear sweep voltammograms for electrochemical reduction of GO as seen by the loss of the reduction peak at -0.6 V with sequential scans. Linear voltage sweeps at the working electrodes were performed from 0 V to -1.6 V (vs. Ag/AgCl electrode) at 100 mV/s scan rate for six cycles in 1X PBS.*
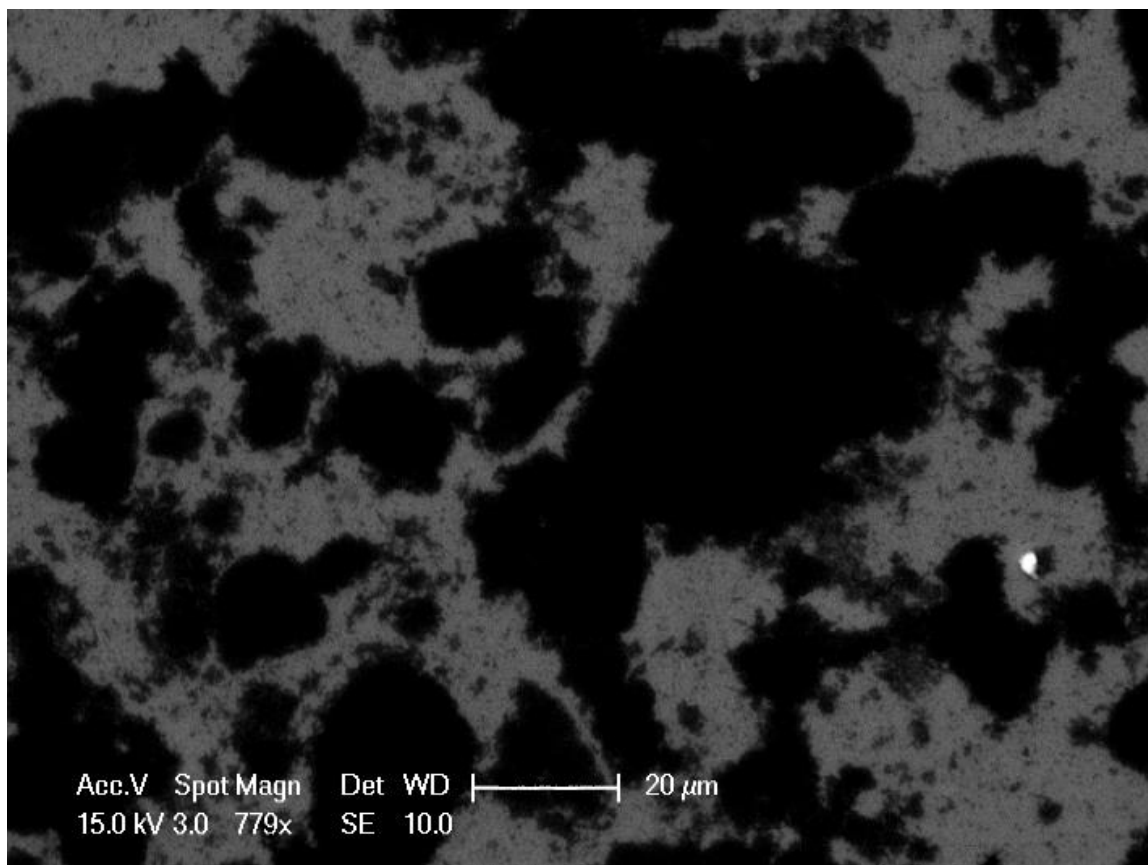
Figure 4.4: SEM image of self-assembled graphene oxide on APTES-modified SiO₂ surface.

Next, to further verify the electrochemical reduction of GO to RGO, we used Raman spectroscopy to examine the removal of oxide groups and restoration of hexagonal carbon network represented in the characteristic D peak, G peak, and 2D peak of pristine graphene and graphene derivatives [7,14]. Raman spectra of GO and RGO (Figure 4.5A) showed the increase in intensity ratio between D (~1350 cm^{-1}) and G (~1600 cm^{-1}) peaks (I_D/I_G) of RGO compared to GO, which corroborates with previously reported Raman studies of GO and RGO[7,13,14]. The decrease in the I_D/I_G ratio after electrochemical reduction suggests the effective restoration of sp^2 carbon bonds and decrease in average sizes of sp^2

domains[14]. The restoration of sp^2 carbon translates to restoration of pi-electrons and thus, electrical conductivity in RGO. Additionally, we observed increases in both the 2D peak (~2690 cm^{-1}) and S3 peak (~2930 cm^{-1}) after electrochemical reduction of GO which suggest enhanced graphitization and lack of charge transfer from removal of impurities. Furthermore, optical micrograph shown in figure 4.5B showed observable differences in coloration between regions of reduced graphene oxide nearer to the gold working electrode compared to unreduced graphene oxide regions far away from the electrodes. While optical properties of RGO has been shown to be tunable based on degree of chemical reduction by hydrazine, electrochemical reduction of GO may also have similar optical effects[15].
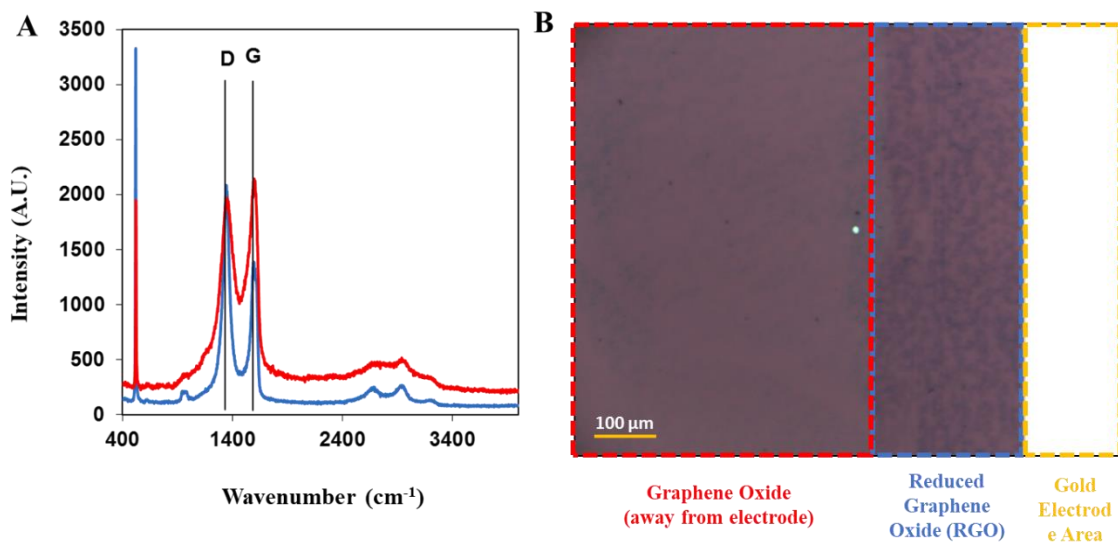
Figure 4.5: *(A) Raman spectra of graphene oxide (red) and electrochemically reduced graphene oxide (blue). (B) Optical micrograph of graphene oxide (red) and electrochemically reduced graphene oxide (blue) regions used for Raman spectroscopic analysis as highlighted in dashed lines.*

We performed electrical characterization by measuring the current across the source and drain electrodes during a potential sweep from -0.1 V to +0.1 V for each

functionalization step which are presented as I-V curves as represented in Figure 4.6. Decreases in the slopes of the IV curves for each additional functionalization step demonstrated the increasing chemiresistive effects of each additional chemical moiety on the RGO device. A combination of charge scattering, electrostatic gating effect, and Schottky barrier effect play a role modulating the electrical properties of graphene and RGO chemiresistive biosensors[10,16–18]. We observed the increase in device resistance, calculated by taking the inverse of the slope of IV curves, for each additional functionalization step as summarized in Figure 4.7 for 14 devices. After electrochemical reduction and anneal of RGO devices, the average resistance for 14 devices were measured to be 2692±909 Ω. During functionalization steps, we observed the largest increase in device resistance after anti-SDE1 pAb functionalization, suggesting high degree of physicochemical changes occurring on the RGO biosensor surface at this step due to successful immobilization of antibodies on the surface. Quenching unreacted NHS-esters from PBASE with ethanolamine did not yield significant change in average device resistance indicating the majority of PBASE linkers have either successfully formed covalent bonds with antibody proteins or have been hydrolyzed during the previous antibody-functionalization step. The final passivation step with tween-20 passivation led to slightly higher average device resistance, indicating some bare RGO sites remained after antibody-functionalization.
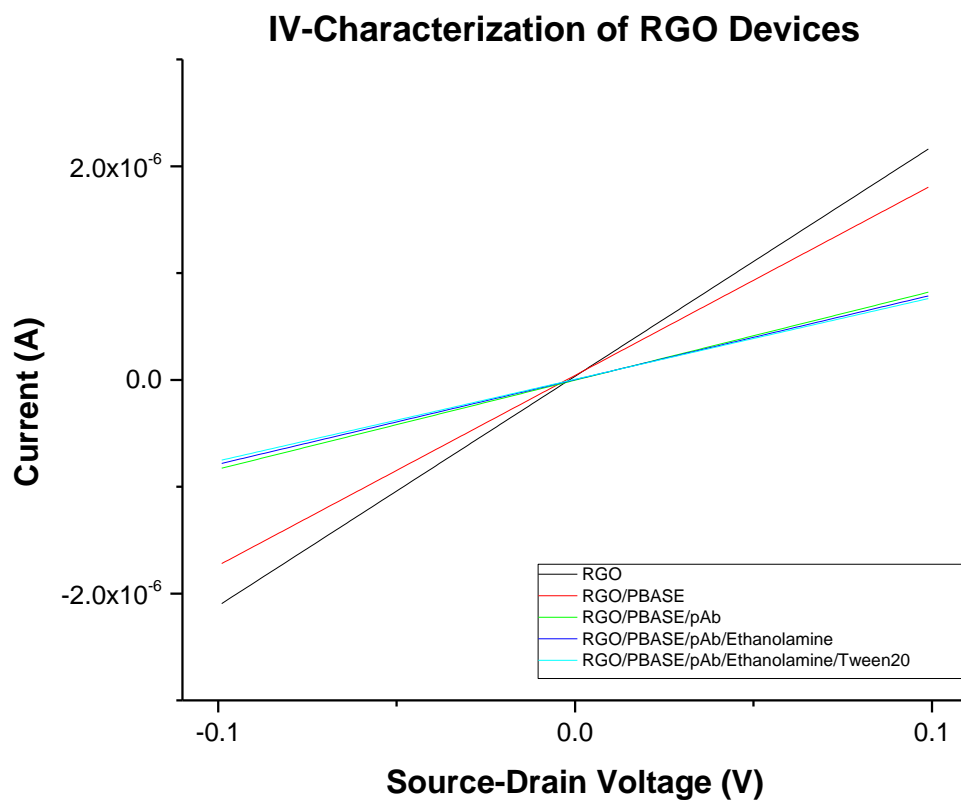
Figure 4.6: *IV characterization of RGO devices at each functionalization step. Potential sweep from -0.1 V to +0.1 V were performed across source and drain electrodes, while current was measured.*

RGO Biosensor Functionalization
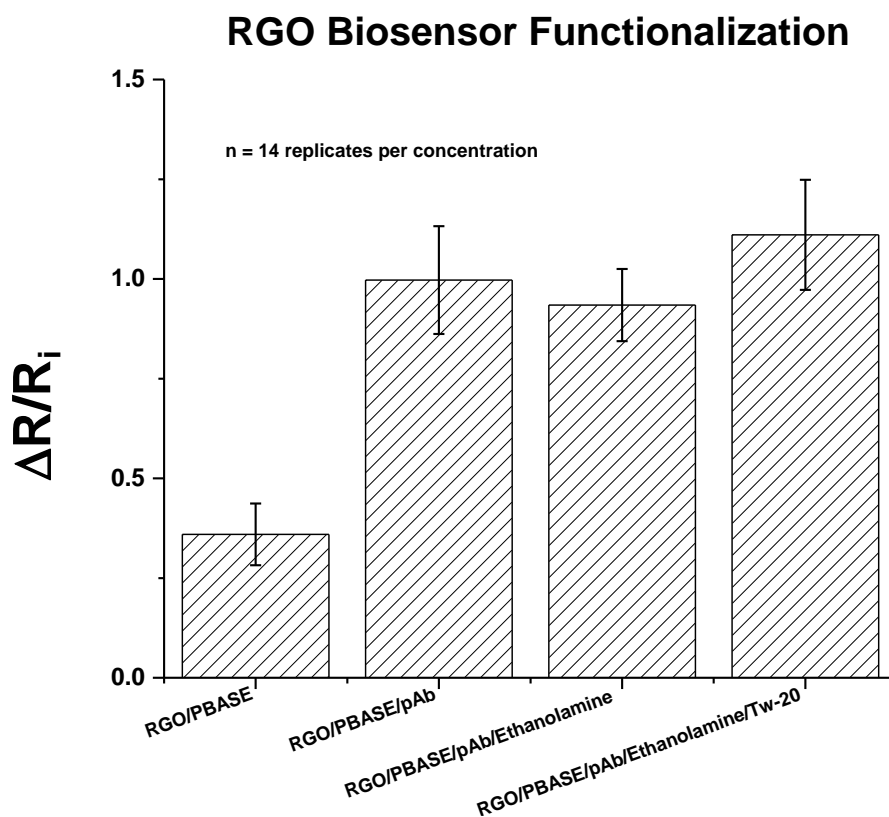
Figure 4.7: *Normalized change in resistance [(R$_f$ – R$_i$)/R$_i$] of 14 RGO devices (n = 14) at each functionalization step. Error bars represent 1 standard deviation.*

4.4.2   Biosensing of SDE1

The electrical properties of RGO are modulated by various mechanisms including electrostatic gating effects, doping effects, Schottky barrier effects, and charge scattering effects[16]. Specific binding of analytes to the antibodies immobilized on the surface of RGO leads to changes in the local electrostatic environment and systematically modulates the electrical properties of RGO, such as electrical resistance/conductance[17,19,20]. By applying a potential and measuring the current between the source and drain electrodes, we then calculated the resistance values that reflect the electrostatic environment at the RGO-

analyte interface[11]. Testing of the fabricated biosensor devices using SDE1 HLB biomarkers show the successful detection of the antigens at various concentrations as shown in Figure 4.8. Buffer controls without SDE1 antigens showed negligible $\Delta R/R_i$ response of -0.00795 ± 0.00743. The devices showed dose-response increases in device resistance with increasing SDE1 concentration. The linear range for the calibration curve was over 3 orders of magnitude starting from SDE1 concentration of 2.4 nM. The limit of detection calculated as 3 times the standard deviation at zero SDE1 concentration was at 2.4 nM.

SDE1 Calibration Curve

n = 14 replicates per concentration

Equation	y = a + b*x		
Weight	Instrumenta		
Residual Sum of Squares	0.04446		
Pearson's r	0.99586		
Adj. R-Square	0.9876		
		Value	Standard Erro
Rf-Ri/Ri	Intercept	0.0251	0.00175
	Slope	0.0240	0.00155

x-axis: SDE1 Concentration (nM)
y-axis: [$\Delta R/R_i$]
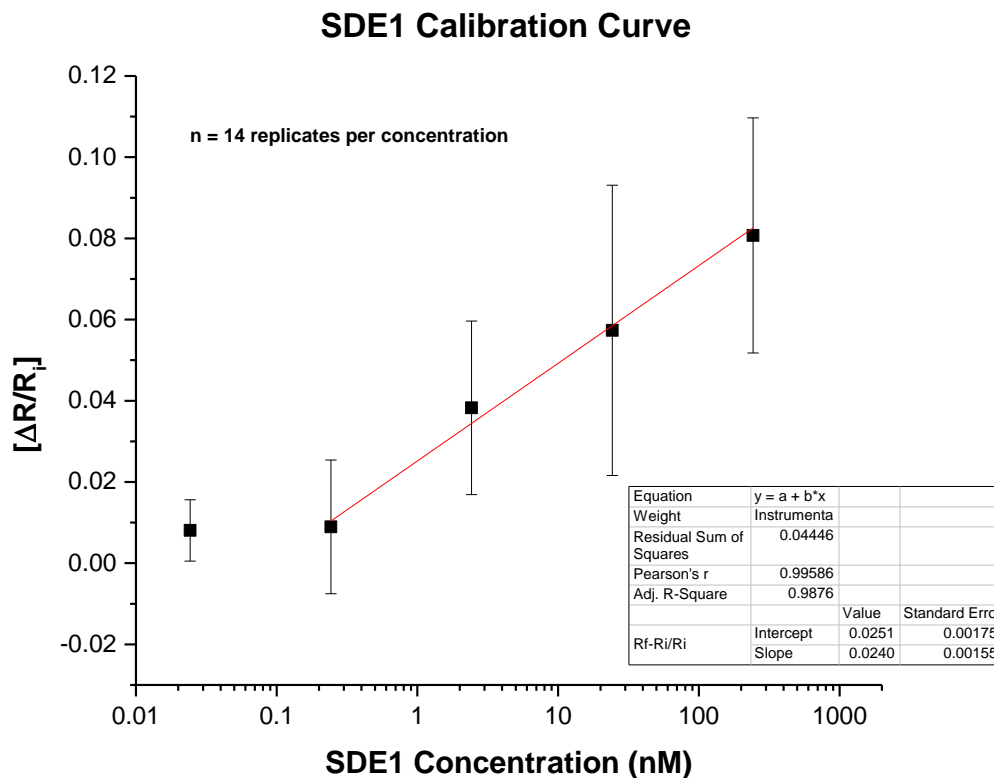
Figure 4.8*: Calibration curve for SDE1 detection in 10 mM PO₄ buffer using rGO-based chemiresistive biosensors. Resistance values at each SDE1 concentration were normalized by [(R_f – R_i)/R_i] of 14 RGO devices (n = 14). R_i is the resistance of the respective biosensor at zero SDE1 concentration.*

4.5   *Conclusion*

In summary, we have demonstrated a quantitative and rapid chemiresitive biosensor for the detection of a biomarker, SDE1, for citrus greening disease. The RGO-based biosensor showed specific binding to the SDE1 biomarker with high sensitivity. The use of a chemiresistor format allows the biosensor to be field-deployable requiring simple instrumentation, which addresses the needs for management of citrus greening disease. In future work, to reduce the magnitude of error bars, additional optimization of device fabrication processes is necessary. Additionally, testing with complex plant sample matrices is required to assess the robustness of the biosensor. Overall, this biosensor platform shows promise for detection of SDE1 biomarkers for HLB disease.

4.5. *References*

1.   Bové, J. M. Huanglongbing: a destructive, newly-emerging, century-old disease of citrus. *Journal of plant pathology* 7–37 (2006).

2.   Gottwald, T. R. Current Epidemiological Understanding of Citrus Huanglongbing *. *Annual Review of Phytopathology* **48,** 119–139 (2010).

3.   Pagliaccia, D. *et al.* A Pathogen Secreted Protein as a Detection Marker for Citrus Huanglongbing. *Frontiers in Microbiology* **8,** (2017).

4.   Irey, M. S., Gast, T. & Gottwald, T. R. Comparison of visual assessment and polymerase chain reaction assay testing to estimate the incidence of the Huanglongbing pathogen in commercial Florida citrus. in *Proc. Fla. State Hortic. Soc* **119,** 89–93 (2006).

5.   Teixeira, D. C. *et al.* Distribution and quantification of Candidatus Liberibacter americanus, agent of huanglongbing disease of citrus in São Paulo State, Brasil, in leaves of an affected sweet orange tree as determined by PCR. *Molecular and Cellular Probes* **22,** 139–150 (2008).

6.   Stankovich, S. *et al.* Synthesis of graphene-based nanosheets via chemical reduction of exfoliated graphite oxide. *Carbon* **45,** 1558–1565 (2007).

7.   Cui, P., Lee, J., Hwang, E. & Lee, H. One-pot reduction of graphene oxide at subzero temperatures. *Chemical Communications* **47,** 12370 (2011).

8.   Hasegawa, M., Hirayama, Y., Ohno, Y., Maehashi, K. & Matsumoto, K. Characterization of reduced graphene oxide field-effect transistor and its application to biosensor. *Japanese Journal of Applied Physics* **53,** 05FD05 (2014).

9.   Tran, T.-T. & Mulchandani, A. Carbon nanotubes and graphene nano field-effect transistor-based biosensors. *TrAC Trends in Analytical Chemistry* **79,** 222–232 (2016).

10.   Liu, F., Kim, Y. H., Cheon, D. S. & Seo, T. S. Micropatterned reduced graphene oxide based field-effect transistor for real-time virus detection. *Sensors and Actuators B: Chemical* **186,** 252–257 (2013).

11.   Tran, T.-T. & Mulchandani, A. Carbon nanotubes and graphene nano field-effect transistor-based biosensors. *TrAC Trends in Analytical Chemistry* **79,** 222–232 (2016).

12.   Zhou, M. *et al.* Controlled Synthesis of Large-Area and Patterned Electrochemically Reduced Graphene Oxide Films. *Chemistry - A European Journal* **15,** 6116–6120 (2009).

13.   Toh, S. Y., Loh, K. S., Kamarudin, S. K. & Daud, W. R. W. Graphene production via electrochemical reduction of graphene oxide: Synthesis and characterisation. *Chemical Engineering Journal* **251,** 422–434 (2014).

14.   Kuila, T. *et al.* Recent advances in graphene-based biosensors. *Biosensors and Bioelectronics* **26,** 4637–4648 (2011).

15.   Shi, H. *et al.* Tuning the nonlinear optical absorption of reduced graphene oxide by chemical reduction. *Opt. Express, OE* **22,** 19375–19385 (2014).

16.   Kim, D.-J. *et al.* Reduced graphene oxide field-effect transistor for label-free femtomolar protein detection. *Biosensors and Bioelectronics* **41,** 621–626 (2013).

17.   Ohno, Y., Maehashi, K. & Matsumoto, K. Chemical and biological sensing applications based on graphene field-effect transistors. *Biosensors and Bioelectronics* **26,** 1727–1730 (2010).

18.   Ohno, Y., Maehashi, K., Yamashiro, Y. & Matsumoto, K. Electrolyte-Gated Graphene Field-Effect Transistors for Detecting pH and Protein Adsorption. *Nano Letters* **9,** 3318–3322 (2009).

19.   Kim, D.-J. *et al.* Reduced graphene oxide field-effect transistor for label-free femtomolar protein detection. *Biosensors and Bioelectronics* **41,** 621–626 (2013).

20.   Zhou, M., Zhai, Y. & Dong, S. Electrochemical Sensing and Biosensing Platform Based on Chemically Reduced Graphene Oxide. *Analytical Chemistry* **81,** 5603–5613 (2009).

Chapter 5

Single-Walled Carbon Nanotube-Based Chemiresistive Biosensor for Detection of SDE1 Biomarker of Citrus Greening Disease in Citrus Plant Tissue

5.1 Abstract

Without a cure in sight, citrus greening disease is the cause of a looming crisis on the multibillion dollar global citrus industry. Thus, it is imperative that disease management strategies address some of the current challenges for accurate, timely, and robust disease detection and diagnosis minimize the spread of disease[1–3]. By adopting a novel detection strategy targeting a secreted protein biomarker, SDE1, we hope to overcome the challenges faced by current detection methods, such as nucleic acid-based and symptom-based which have been found prone to false negatives and mis-diagnoses, respectively[3]. By combining the physical and chemical advantages of carbon nanomaterials like SWNTs with FET and chemiresistive biosensors technologies, we have demonstrated a label-free biosensor platform for the detection of HLB biomarkers. With the dynamic range over 3 orders of magnitude in the low nanomolar to micromolar concentration range, the biosensor platform is a viable tool to add to the list of disease management tool shed.

5.2 Introduction

Citrus greening disease, also known as Huanglongbing (HLB) disease, is posing a worldwide threat to the multi-billions dollar industry[1]. The disease leads to symptoms of rapid tree decline, where fruit production by the infected tree is significantly affected. Some symptoms include small, poorly colored, lopsided and off-tasting fruit, and mottled leaves. The primary mode of transmission of the pathogenic agents is through insect vectors, predominantly by the Asian and African citrus psyllids, *Diaphorina citri* and *Trioza erytreae*, respectively[1,2]. The pathogens responsible for HLB are the *Candidatus* Liberibacter bacterial species, which colonize the phloem tissues of infected plants[1,2,4]. The three species of *Candidatus* Liberibacter responsible for the disease are *Candidatus* Liberibacter asiaticus (*C*Las), *Candidatus* Liberibacter africanus (*C*Laf), and *Candidatus* Liberibacter americanus (*C*Lam). The various species are not constrained to the geographical regions based on their respective names. However, the focus of our work will be on the detection of the Candidatus liberbacter asiaticus (*C*Las) species, which is most globally rampant in Asia and in North America.

As known to date, there are no cures for trees affected with HLB disease; therefore, management of the spread of the disease is focused on removal of the pathogens via eradication of infected trees and vectors[1,3,4]. Thus, timely and accurate detection of infected plants is crucial for disease management; however, detection methods based on disease symptoms and nucleic-acid assays remain unsuccessful. Symptoms-based and qualitative diagnosis of infected plants lack accuracy due to variable latency of symptoms and due to similarities of symptoms with other citrus diseases and nutrient deficiency[4]. Assays for

detection of nucleic acid-based biomarkers of *Ca*. Liberibacter have high rates of false negatives due to uneven distribution of the phloem-colonizing pathogen in infected plants[2,5]. Furthermore, nucleic acid-based assays require laborious sample preparation and are costly and time-consuming, making these tools prohibitive for wide applications for disease management, especially when multiple samples need to be tested from one tree[1]. Therefore, the detection of secreted protein-based biomarkers for the pathogen addresses the performance requirements for accuracy, speed, robustness, and portability. A *C*Las Sec-delivered effector (SDE1) protein, discovered and studied by the Ma Lab, is a promising biomarker candidate for HLB disease[3]. Compared to the phloem-colonizing *C*Las bacteria, their secreted SDE1 proteins are believed to be evenly and systematically distributed throughout the infected trees, which consequently eliminate the need for multiple sampling sites per tree. Thus, by adopting the detection strategy using the SDE1 biomarker, we are able to achieve facile and reliable diagnosis of infected plants by reducing the rate false negatives due to sampling challenges.

In FET-based biosensors utilizing semiconducting SWNTs, the single-layer surface atoms of the carbon nanomaterials are directly exposed to the environment, such that small alterations at the interface result in large changes in electrical properties of the nanomaterials[6]. Furthermore, the nanoscale dimensions of these carbon nanostructures are comparable to the Debye length, the distance of away from the sensor surface where the net electrostatic effects of charged molecules persist, ensuring successful electrical transduction of physical and chemical interactions at the SWNT surface. Biosensors employing an FET architecture and operation differ from conventional three-electrode

electrochemical biosensor setup and operation, which typically has a working electrode, a reference electrode and a counter electrode[7,8]. The three-electrode setup of electrochemical biosensors are commonly utilized for measurement modes such as amperometry and potentiometry. The aforementioned electrochemical methods require electroactive species or biocatalytic elements to generate electrical responses [8,9]. However, FET-based biosensors can yield electrical responses upon affinity-based binding or adsorption of charged biomolecules with the semiconducting (transducer) channel. The electric field generated by charged biomolecules near the interface of the semiconducting material provides electrostatic gating effects on the channel that are resemble the effects from applying a voltage potential is to the gate terminal. Other electrical phenomena can result from such interfacial molecular interactions, such as modulation of the Schottky barrier (where metal-semiconductor junctions are present) and charge scattering. This characteristic highlights the potential of this biosensor architecture for label-free and affinity-based sensing.

Applying the advantages of nanoscale FET-based biosensors using semiconducting SWNTs and incorporating the biomarker strategy using the CLas-specific SDE1 protein, we have developed a novel label-free chemiresistive biosensor platform for the detection of said pathogen. Our biosensor scheme is that of a chemiresistor-type biosensor, a variation of the FET-biosensor architecture, which omits the gate electrode, allowing the modulation of device conductance by the same mechanisms as in traditional FET-based biosensors with the external gating solely by the charged molecules near the interface of the semiconducting channel[10,11]. Changes in electrical properties of the device, such as

conductance or resistance, indicate physical and chemical alterations of the surface properties of the carbon nanomaterials[12]. To impart specificity to our biosensor, we functionalized the SWNTs transducing channel with anti-SDE1 antibodies. The biosensor showed sensitivity and specificity for the SDE1 biomarker in phosphate buffer and citrus plant tissue extracts.

5.3. *Materials and Methods*

5.3.1. Reagents and Materials

All materials and chemicals were purchased from Fisher Scientific unless specified otherwise. Recombinant HLB biomarker, SDE1, and anti-SDE polyclonal antibodies (pAb) were obtained from Dr. Wenbo Ma's laboratory at the University of California-Riverside. 95% 3-Aminopropyl)-triethoxysilane (APTES), 1-Pyrenebutyric acid N-hydroxysuccinimide ester (95%) (PBASE), anhydrous N,N-dimethylformamide (DMF), and ethanolamine were obtained from Sigma Aldrich (St. Louis, Mo, USA). Graphene oxide 5 mg/mL in water suspension was purchased from Stanford Advanced Materials (Irvine, CA, USA). Tween-20 was obtained from Bio-Rad (Irvine, CA, USA). Highly p-doped 4-inch silicon wafers with 300 nm thermal oxide layer were purchased from Ultrasil Corporation (Hayward, CA, USA). 95% semiconducting SWNTs solution supplied at 10 μg/mL in 0.8% sodium cholate and 0.2% sodium dodecyl sulfate was purchased from NanoIntegris, Inc. (Quebec, Canada). SWNTs solution was further diluted in the same surfactant solution to 2.5 μg/mL for device fabrication. 10 mM phosphate buffer (PB) pH

7.4 was prepared from monobasic and dibasic sodium phosphate salts and pH-adjusted with dilute hydrochloric acid and sodium hydroxide.

5.3.2   Device Fabrication

As presented in the scheme in Figure 5.1, we used photolithography and lift-off process for patterning of 10-μm gap gold (Au) microelectrodes onto Si/SiO$_2$ wafer in the cleanroom at the Center for Nanoscale Science and Engineering, University of California, Riverside (UCR). Briefly, we used photolithography with Shipley 1813 positive photoresist to define microelectrodes with 10 μm by 10 μm gap size onto Si/SiO$_2$ wafer. We then used e-beam evaporation to deposit 10 nm of a chromium (Cr) adhesion layer and 100 nm of Au. Finally, we used acetone to remove excess photoresist and Cr-Au layers, leaving multiple patterns of the microelectrodes. After cutting individual chips from the wafers, we cleaned the chips acetone and IPA, then dried devices under a stream of nitrogen.

We first functionalize the surface of the device with a self-assembled monolayer of (3-aminopropyl)triethoxysilane (APTES) which aids in the assembly of SWNT network on the surface of our sensor. After APTES functionalization, a 10 μm by 50 μm rectangular region of APTES overlapping two electrodes was photolithographically patterned by first using Shipley 1813 photoresist to protect the rectangular region, followed by reactive ion etching on an Oxford Plasmalab 100/180 etcher of unprotected surfaces to remove excess APTES outside of the 10 μm by 50 μm regions. We then removed the protective Shipley

1813 photoresist to re-expose 10 µm by 50 µm rectangular region of APTES using an acetone bath, followed by washing with isopropyl alcohol, and drying with nitrogen.

Next, we drop-casted 5 µL SWNT solution onto the patterned APTES region and allowed the droplet to dry in air overnight. The anionic surfactant molecules, which are physisorbed to the SWNTs, are electrostatically attracted to the amino groups of the APTES covered surface, which consequently anchors the SWNTs onto the APTES-functionalized SiO_2 surface[13–15]. Washing the device with distilled water removes excess unbound and weakly bound SWNTs and excess surfactant molecules from the sensor surface. Next, annealing SWNTs in air at 250 °C burns off remaining detergent molecules leaving SWNT surfaces free for further functionalization. Chemical passivation of gold electrodes was achieved by incubating the device with 100 mM 6-mercapto-1-hexanol diluted in anhydrous ethanol (200 proof) for 1 hour at room temperature, followed by rinsing in ethanol and blow-drying under a stream of nitrogen. PBASE linker molecules were functionalized on SWNT surfaces by incubation with 3.0 mg/mL of PBASE reagent in DMF for 1 hour at room temperature. Next, to impart specificity to the biosensor, 20 µL of 50 µg/mL of anti-SDE1 antibody molecules in PB was drop-casted onto the SWNT sensing region and incubated overnight at 4 °C. The biosensor was then blocked with bovine serum albumin at 10 mg/mL in PB for 1 hour. Unreacted succinimidyl esters were chemically quenched by reacting with 100 mM ethanolamine in 10 mM phosphate buffer, pH 8.0. Bare and unfunctionalized SWNT regions were then passivated with 1% w/v of

Tween-20 surfactants for 1 hour. These quenching and blocking steps minimize non-specific binding of biomolecules to our sensor.
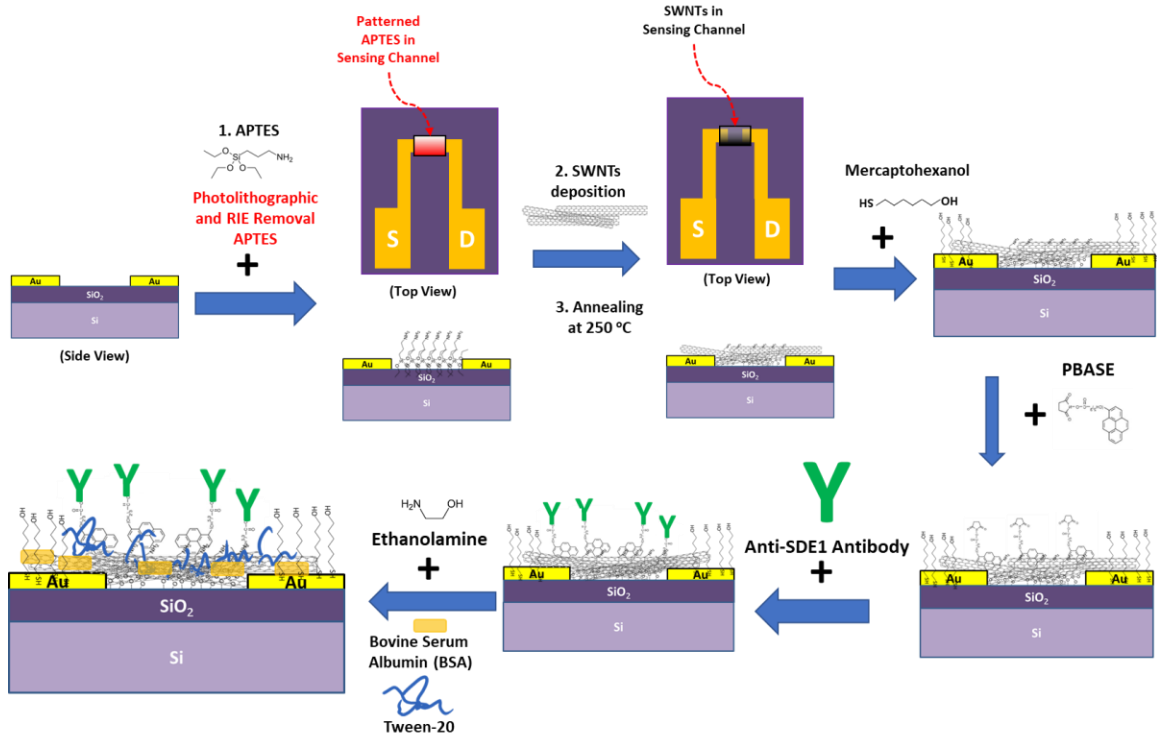
Figure 5.1: *Schematic diagram illustrating fabrication and functionalization process for SWNT-based chemiresistor devices.*

5.3.3 Citrus Plant Sample Preparation

Healthy (uninfected) grapefruit plant tissue samples were provided by the Ma Lab. Briefly, stem samples from young branches were cut into small sections and grounded to fine powder following the protocols from Pagliaccia et al.[3]. Grounded tissue was then suspended in PB at 1.0 g/mL and vortexed to mix. We then obtained the supernatants (i.e. extract) by centrifuging the suspensions at 13,800 x g for 5 minutes. Supernatants were

then syringe-filtered with 0.2-µm membrane pore size to remove large plant debris. For biosensing experiments, supernatants were then diluted in PB to 10% v/v.

5.3.4 Electrical Measurement and Biosensing Protocols

Electrical measurements were performed using a Keithley 2636B source and measurement unit. Measurements were multiplexed across multiple devices using an in-house built multiplexer system based on the Arduino Mega 2560 microcontroller and relay boards. LabVIEW software was used to control measurement instruments and for data acquisition. Current versus time (I-t) measurements were performed at a fixed source-drain potential (V_{SD}) of +0.1 V. I-t measurements were achieved by sequentially measuring each biosensor at 0.5-second intervals using the multiplexer unit. Resistance versus time (R-t) curves values were obtained by dividing the 0.1 V (applied V_{SD}) by each measured I_{SD} value at each time. Current versus voltage (I-V) measurements were obtained by applying a sweeping source-drain potential (V_{SD}) from -0.1 V to +0.1 V with 0.01 V step size, while measuring source-drain current (I_{SD}). Back-gated FET measurements were conducted by using the p-doped silicon as the bottom gate electrode and sweeping the gate potentials (V_{BG}) with a constant V_{SD} bias of 0.1 V and measuring I_{SD} and gate-drain leakage current ($I_{leakage}$).

I-t measurements were used to monitor real-time current responses of each SWNT biosensor to various samples and concentrations of SDE1 protein. Prior to biosensing experiments, a silicone well with pressure sensitive adhesive was placed over the biosensor to prevent overflowing of samples outside the sensing region. Biosensing experiments and measurements were conducted at room temperature in a humid chamber. For SDE1

detection in PB, 15 µL of PB was initially drop-casted gently onto the sensing area. After allowing SWNT biosensor current response to stabilize within 10 to 15 minutes, sequential additions of 1 to 2 µL of samples were pipetted into the 15 µL PB drop with gentle mixing by aspiration with the same micropipette. SDE1 samples in PB with increasing concentrations were sequentially added this way in 15- to 30-minute intervals to allow for stable current responses. For SDE1 detection in plant tissue extract, SDE1 proteins were diluted into 10% plant tissue extract to simulate real samples. Firstly, 15 µL of PB was drop-casted gently onto the sensing area. The sensor was then pre-conditioned to the sample matrix by adding another 15-uL drop of the plant tissue extract (without SDE1 protein) into the droplet with gentle mixing by pipette aspirations. After allowing SWNT biosensor current response to stabilize within 30 minutes, additions of 1 to 2 µL of SDE1 in plant tissue extract were pipetted onto the sensing are with gentle mixing by aspiration with the micropipette. Total SDE1 concentrations were calculated for each sample addition to account for changes in volume of the sample solution on the biosensor.

Calibration curves for multiple biosensors were obtained by averaging normalized resistance changes ($\Delta R/R_i$) at each sample condition for. More specifically, resistance over time measurement for each biosensor was averaged over 30 measurements (approximately 60 seconds intervals) and the resistance changes were calculated using the equation

$$\frac{\Delta R}{R_i} = \frac{R_f - R_i}{R_i} \qquad (1)$$

where R_f is the equilibrated resistance after each addition and R_i is the equilibrated resistance of the initial PB addition and the initial biosensor precondition step for detection of SDE1 in PB and in plant tissue extract, respectively.

5.4 Results and Discussion

5.4.1 Device Characterization

Carbon nanotubes can be considered a 1-dimensional allotrope of carbon, which can be described as a ribbon of graphene comprising sp^2 hybridized carbon atoms with a hexagonal lattice seamlessly rolled into a cylindrical tube[16,17]. Single-walled carbon nanotubes (SWNTs) have one single layer of sp^2 carbon atoms forming the nanotube[16,18]. SWNTs can have either semiconducting or metallic electronic properties depending on their chirality and diameter[19]. Back-gated FET measurements of our SWNT devices confirms p-type semiconductor behavior of SWNTs where the major charge carriers are holes carriers as shown in figure 5.2. This is evident as I_{SD} value increased with more negative gate voltages which p-dopes the semiconducting SWNT channel enhancing the number of hole charge carriers. Conversely, more positive gate voltages n-dopes the SWNT channel, leading to depletion of the major hole charge carriers as seen by lower I_{SD} values[20–22]. Leakage current was shown to be negligible (average $I_{Leakage} = 24 \pm 70$ nA) compared to source-drain current ($I_{SD} > 10^4$ nA) which validated our FET measurement by confirming the lack of current contribution from the gate electrode. Using scanning electron microscopy (SEM) using a Leo SUPRA-55 instrument at the Center for Nanoscale Science and Engineering at UCR, we confirmed the preferential deposition of SWNTs onto

APTES-patterned SiO_2 surface of the biosensor. As shown in Figure 5.3, monodispersed

SWNTs self-assembled onto the 10 μm by 50 μm rectangular APTES region with much

higher density and uniformity than SiO_2 surfaces without APTES.
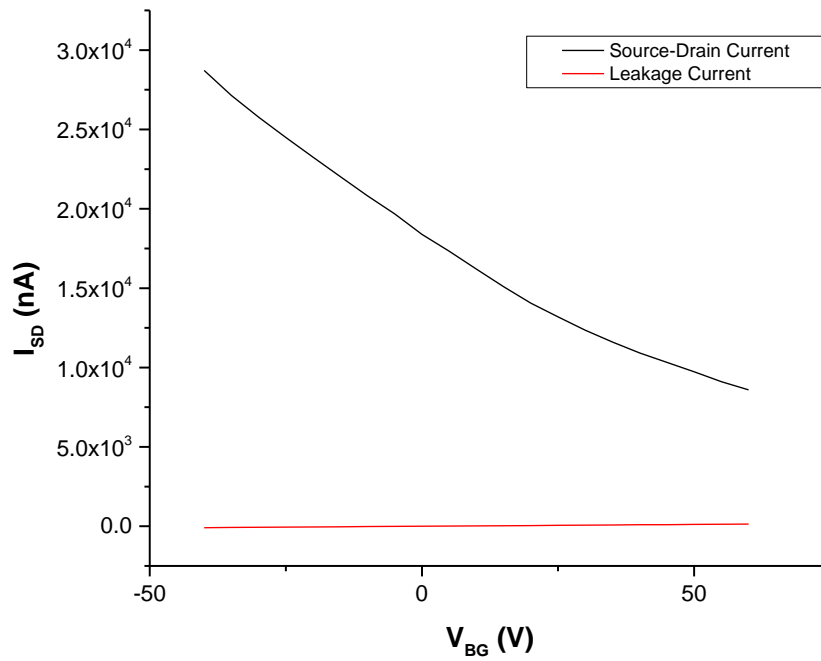
Figure 5.2: *Back-gated FET measurement of SWNT device in air after the annealing step. Measurements were conducted by using the silicon substrate as the bottom gate electrode and sweeping the gate potentials (V_{BG}) from -40 V to 60 V (5.0 V increments) with a constant V_{SD} bias of 0.1 V and measuring I_{SD} and gate-drain leakage current ($I_{leakage}$)*
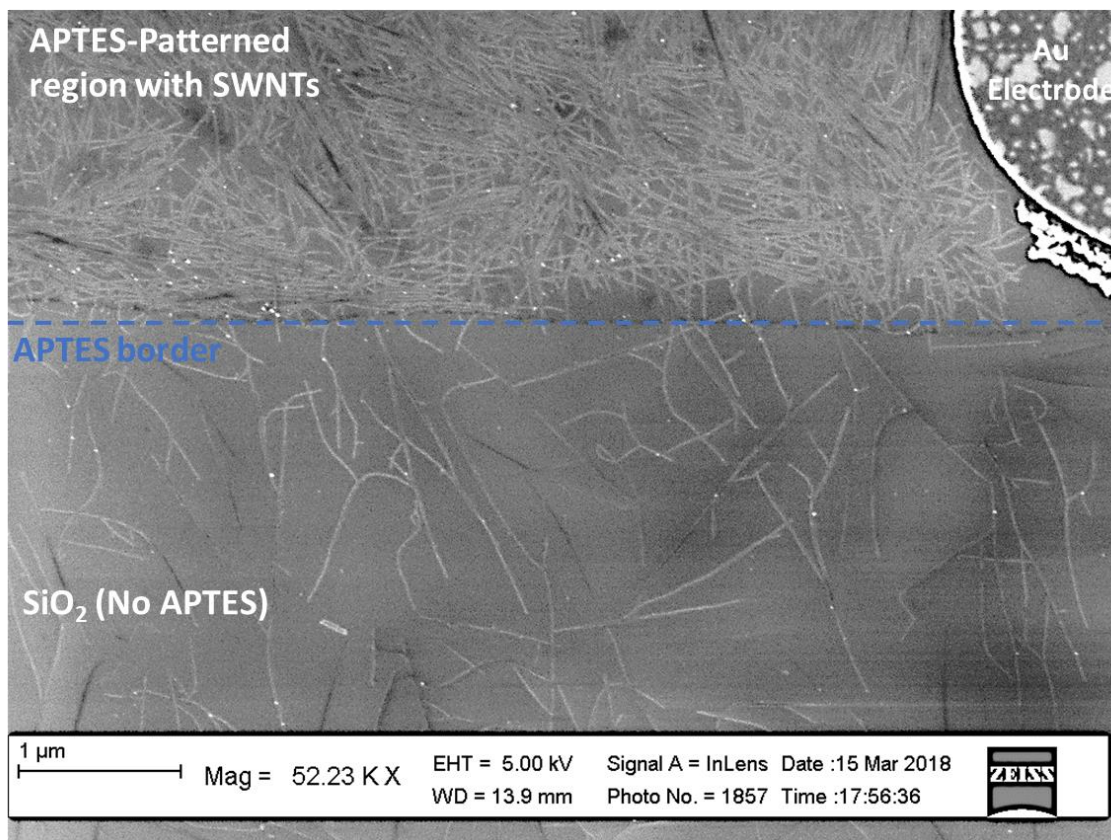
Figure 5.3: SEM image of SWNTs deposited onto APTES-patterned SiO₂ surface with preferential self-assembly on APTES-functionalized areas versus bare SiO₂ areas.

To achieve specific detection of analyte molecules, the SWNTs required functionalization with the biorecognition elements (e.g. antibodies, enzymes, aptamers, and other binding peptides, etc.). Conjugation of SWNTs with the biorecognition molecules is achieved through various chemical means that can be categorized as direct covalent conjugation to the carbon nanostructure or through non-covalent conjugation to the nanostructure [20,23,24]. One major disadvantage of covalent functionalization of SWNTs and graphene is the alteration of electronic structure and properties of the nanotubes due to disruption of carbon sp^2 bonds[24,25]. Therefore, we have opted for the non-covalent

functionalization strategy. Non-covalent conjugation of biomolecules onto sp^2 carbon bond-rich SWNT surfaces typically uses bi-functional linker molecules, such as 1-pyrenebutanoic acid succinimidyl ester (PBASE) used in this work. The π-electron-rich pyrenyl group π-stacks with the carbon nanostructure while the succinimidyl ester group specifically reacts with amine groups on the biorecognition molecule to form an amide bond. After functionalizing the carbon nanomaterials with the desired biorecognition molecules, unreacted chemical moieties and carbon surfaces are chemically quenched and physically blocked—with surfactants, amphipathic polymers, or nonspecific protein, respectively[26]. Chemical quenching and blocking minimize non-specific binding during sensing procedure. We have monitored the various functionalization steps using I-V measurements as shown by IV characteristics of a representative device in Figure 5.4. Due to the sensitivity of the succinimidyl ester of PBASE linkers to hydrolysis, we omitted IV measurement after PBASE functionalization to allow for immediate incubation with the anti-SDE1 antibodies for further bioreceptor immobilization. After antibody conjugation to the SWNT surface via PBASE linker, we observed a large decrease in the slope of the IV measurements (i.e. increase in device resistance) from bare SWNTs. While PBASE linkers have been shown to contribute to changes in p-type SWNT device resistance by electron donation and charge scattering, subsequent biomolecule conjugation to PBASE consistently yield more significant changes in the slopes of IV curves due to the much larger size of protein molecules indicating increased device resistance[27–29]. Subsequent quenching and blocking steps led to additional increase in the device resistance.
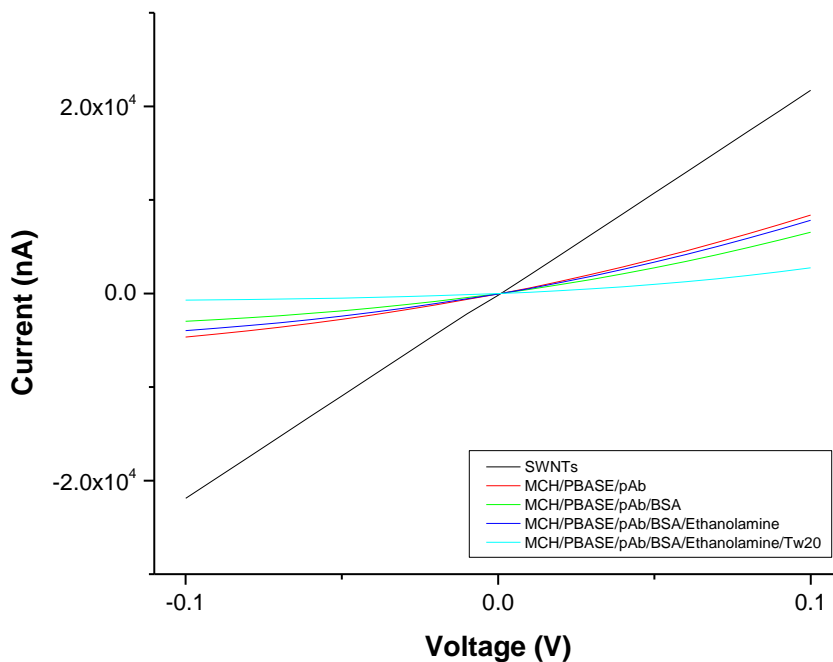
Figure 5.4: IV-Curves of a representative SWNT device at different functionalization steps. Measurements were from -0.1 V to +0.1 V with step size of 0.01 V. Measurements were conducted in 10 mM phosphate buffer pH 7.4.

5.4.2   Detection of SDE1 HLB Biomarker

After SWNT biosensors were functionalized with anti-SDE1 antibodies and blocked, we proceeded to biosensing experiments. Figure 5.5 shows a representative real-time response of a single biosensor for detection of SDE1 HLB biomarkers spiked in simple PB. The sensor response ($\Delta R/R_i$) was normalized to the resistance of the initial addition of 15 μL PB. Each biosensor produced similar electrical responses to the various additions of negative controls samples and SDE1 proteins. From the R-t measurements, we observed that three sequential additions of 1 μL PB (blank controls) produced little to no change in sensor response after allowing for 10 minutes for stabilization from the physical

perturbation. Furthermore, as summarized in Figure 5.6, even after additions of much higher concentrations of bovine serum albumin (BSA) negative controls at 790 nM and 1500 nM, average sensor responses for 9 devices ($\Delta R/R_i = 0.06 \pm 0.03$ and $\Delta R/R_i = 0.07 \pm 0.03$, respectively) were significantly lower compared to sensor responses to 34 nM of SDE1 ($\Delta R/R_i = 0.32 \pm 0.11$). This is indicative of the specificity of our biosensors for SDE1 HLB biomarkers. A calibration curve was generated from the averaged normalized resistance responses of these 9 sensors as shown in Figure 5.7. The data points were fitted to a 4-parameter logistic model using the following function

$$y = \frac{A1 - A2}{\left[1 + \left(\frac{x}{x_0}\right)^p\right]} + A2 \qquad (2)$$

as recommended for ligand-binding assays, where y represents the normalized change in resistance (i.e. sensor response), x is the independent variable (SDE1 concentration), $A1$ is the maximum value of the calibration curve, A2 is minimum value of the calibration curve, x_0 is the concentration at EC_{50}, and p is the slope at $x = x_0$[30–32]. From the calibration curve in Figure 5.7, we observed that the biosensors had a dynamic response range of tens of nanomolar to micromolar concentrations of SDE1 biomarker[30–32]. The limit of detection, based on the signal-to-noise of 3, was estimated to be less than 1 nM of SDE1.

In order simulate detection of the SDE1 HLB protein biomarkers in real plant tissue samples, we have used plant extracts prepared from healthy (uninfected) grapefruit plant tissues as the sample matrix. SDE1 proteins were spiked into the plant extract at various concentrations for biosensor experiment. The biosensors were conditioned by adding 15 µL of healthy plant tissue extract to the 15 µL of PB on the sensing area for 30 minutes

until the sensor response stabilized. By allowing the sensor to equilibrate to the more complex plant extract matrix, we can avoid background responses from the biomolecule-rich extract and reduce their interfering effects. Before proceeding to additions of SDE1-spiked plant extract samples, we verified a stable baseline response by adding another 10 µL of plant extract (without SDE1 proteins) and observed no significant change in normalized sensor response ($\Delta R/R_i = -0.03 \pm 0.05$) from the baseline ($\Delta R/R_i = 0.00 \pm 0.01$) for 5 biosensors (n = 5). Next, we proceed with sequential additions of samples SDE1 antigens spiked in plant extract. Figure 5.8 shows the normalized real-time sensor response for a representative biosensor for detection of SDE1 biomarker in complex plant tissue extract. All biosensors showed similar increase in resistance responses to each addition of SDE1 in plant tissue extract, which is consistent with SDE1 detection in PB. The dose-dependent sensor responses to increasing concentrations of SDE1 biomarker in the presence of plant extract suggests the biosensors are indeed specific to SDE1 HLB biomarkers even in the complex plant tissue matrix. A calibration curve was generated from the averaged normalized resistance responses of these 5 sensors as shown in Figure 5.9. The data points were fitted to a 4-parameter logistic model as recommended for ligand-binding assays with a dynamic response range of few nanomolar to few micromolar concentrations of SDE1 biomarker in plant extract which is similar to that of SDE1 detection in PB [30–32]. The limit of detection, based on the signal-to-noise of 3, was estimated to be 5 nM of SDE1. While the trends for the calibration curves of SDE1 detection in PB and detection in plant extract are positive, we observed that the two calibration curves do not exactly align and have different values for the four parameters A1, A2, x_0, and p fitted

using the 4-parameter logistic function. This may be due some persistent matrix effect of the plant tissue extract. This matrix effect was similarly observed in our previous work described in Chapter 3, "Generation of Anti-SDE1 Antibody and Development of an Enzyme-Linked Immunosorbent Assay (ELISA) for Detection of SDE1 HLB Biomarker." We recall that the indirect competitive inhibition ELISAs for SDE1 detection in buffer and detection in plant extracts yielded calibration curves with similar trends but different values for the four parameters (A1, A2, x_0, and p) used for modeling the curves.

One strategy to account for matrix effects is to use the standard addition method [33–35]. We prepared standard addition solutions of known concentrations of SDE1 proteins in healthy plant tissue extracts mixed with a simulated "unknown" plant extract sample spiked with a theoretical concentration of 29.4 nM as shown in Table 5.1. Applying these samples onto our immunosensors and measuring the normalized $\Delta R/R_i$ we generated a standard addition curve which allowed us to calculate the original concentration of the "unknown" plant extract sample of 26.4 nM, as shown in Figure 5.10. The measured concentration using the standard addition is within 90 percent of the theoretical concentration of the simulated unknown sample. This suggests that the method of standard additions is a viable assay method for mitigating plant extract matrix effects without requiring an external calibration curve.

Upon specific intermolecular interactions between SDE1 molecules with functionalized anti-SDE1 antibodies at the surface of the SWNTs, one or more of the following mechanisms are known to contribute to the modulation of electrical properties (i.e. measured electrical responses) of SWNT-FET biosensors: (1) surface charge-induced

gating effect or electrostatic gating, (2) charge transfer between the biomolecules and the carbon nanomaterials, (3) charge scattering across the carbon nanomaterials, and (4) Schottky barrier modification occurring between the carbon nanomaterials and metal electrodes [6,20,21,36–38]. To elucidate which mechanism(s) contribute to observed sensor responses and the degree to which the mechanism(s) influence our sensor responses requires extensive mechanistic study and modeling. However, through systematic investigations of SWNT-based FET biosensors, Heller et al. had suggested that the two major sensing mechanisms of these biosensors are from electrostatic gating effect and modulation of the Schottky barriers[21].

Figure 5.5*: Normalized real-time chemiresistive response of a representative SWNT biosensor to the addition of increasing SDE1 concentrations spiked in 10 mM phosphate buffer, pH 7.4. Sensor response was normalized to the device resistance at the initial addition of 15 μL PB. Arrows indicate times of sample addition with corresponding total SDE1 concentrations. Real-time measurements were obtained by applying 0.1V potential across the source-drain electrodes while monitoring source-drain current. Resistance values at each time point were calculated by taking the quotient of 0.1V applied potential with measured source-drain current.*
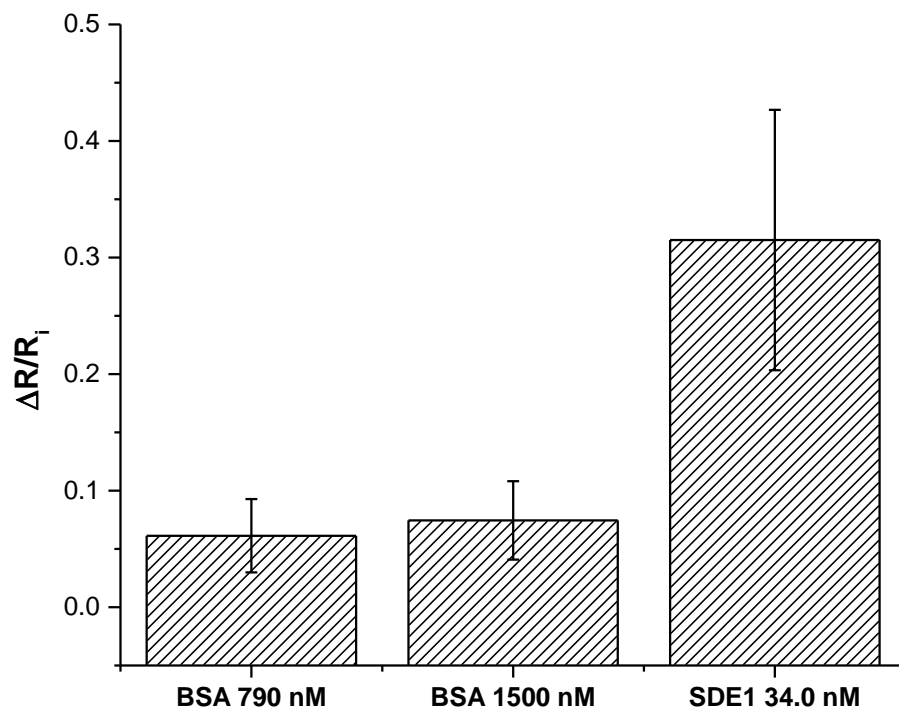
Figure 5.6*: Normalized resistance responses of SWNT biosensors to high concentrations of nonspecific bovine serum albumin (BSA) proteins at 790 nM and 1500 nM compared to much lower concentration of SDE1 antigen. Devices were functionalized with anti-SDE1 antibodies. Each data point represents the average normalized resistance from multiple independent biosensors. Error bars represent ±1 standard deviation from 9 biosensors (n = 9).*

SDE1 Calibration Curve in 10 mM Phosphate Buffer

n = 9 replicates per concentration

Model	Logistic		
Equation	y = A2 + (A1-A2)/(1 + (x/x0)^p)		
Reduced Chi-Sqr	0.00735		
Adj. R-Square	0.9996		
		Value	Standard Error
Delta R/Ri	A1	0.01233	1.95846E-4
	A2	0.84334	0.09086
	x0	115.31675	64.03766
	p	0.42274	0.07008
	EC20	4.34231	0.60907
	EC50	115.31675	64.03766
	EC80	3062.41468	3338.01964

Figure 5.7*: Calibration plot of SDE1 proteins in 10 mM phosphate buffer, pH 7.4. Resistance changes were calculated using the equation* $\frac{\Delta R}{R_i} = \frac{R_f - R_i}{R_i}$ *where* R_f *is the equilibrated resistance after each addition, and* R_i *is the equilibrated resistance of the initial PB addition. Data was fitted using 4-parameter logistic regression analysis. Data points represent the averaged normalized measurements from 9 (n = 9) independent SWNT biosensors. Error bars represent ±1 standard deviation.*
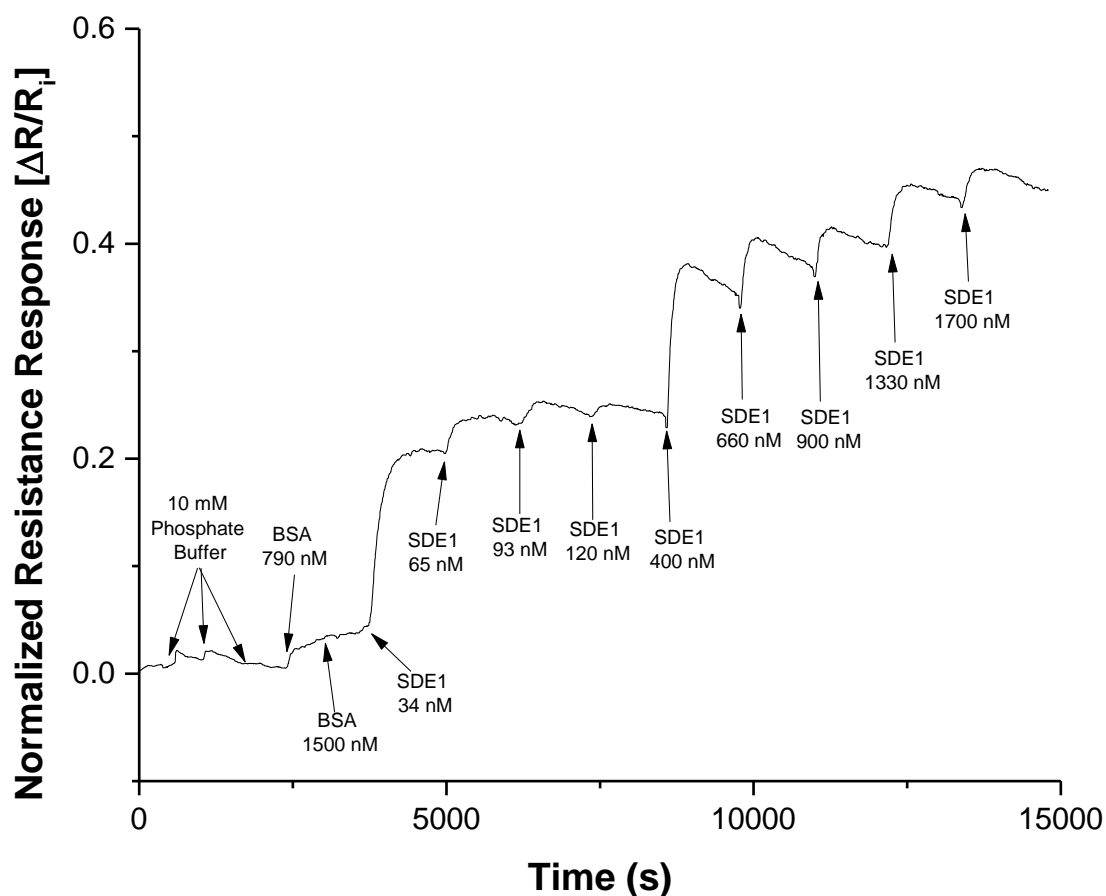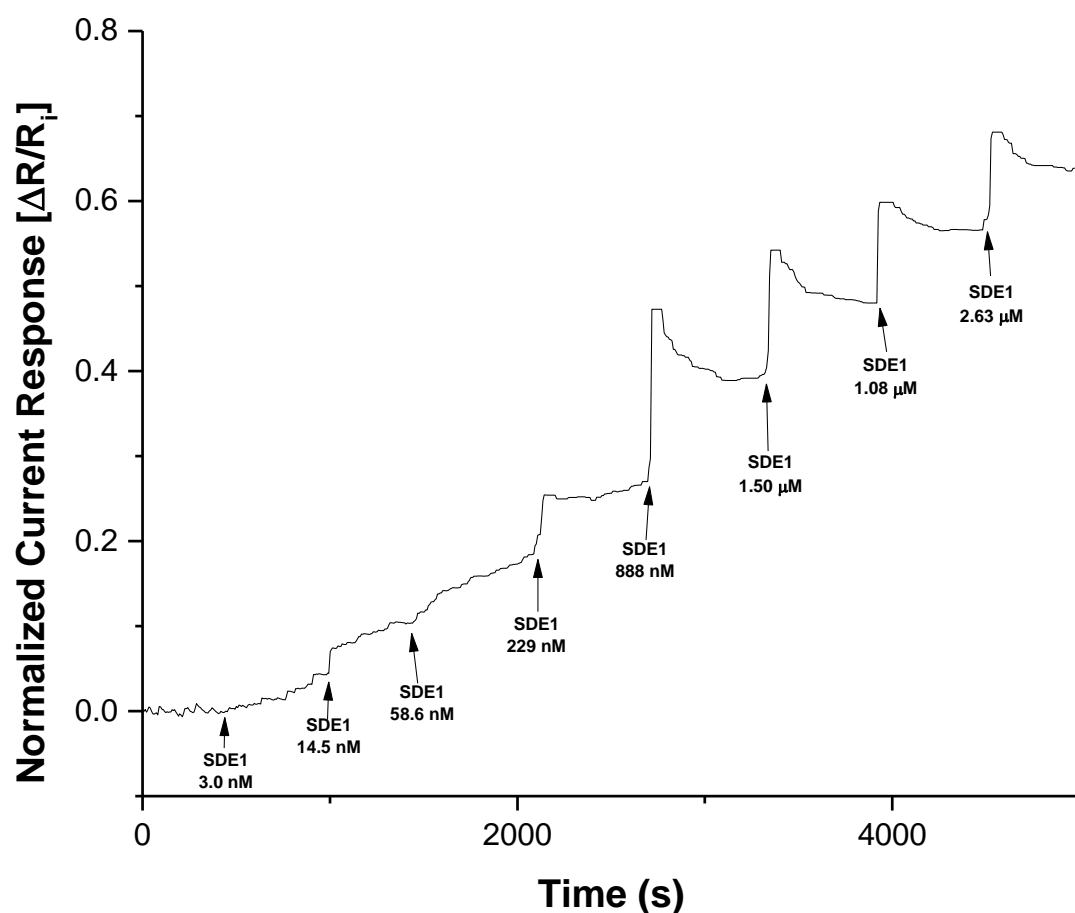
Figure 5.8: Normalized real-time chemiresistive response of a representative SWNT biosensor to the addition of increasing SDE1 concentrations spiked in grapefruit plant tissue extract. Sensor response was normalized to the device resistance after biosensor conditioning with plant tissue extract without SDE1. Arrows indicate times of sample addition with corresponding total SDE1 concentration. Real-time measurements were obtained by applying 0.1V potential across the source-drain electrodes while monitoring source-drain current. Resistance values at each time point were calculated by taking the quotient of 0.1V applied potential with measured source-drain current.

SDE1 Calibration Curve in Plant Tissue Extract

Model	Logistic		
Equation	y = A2 + (A1-A2)/(1 + (x/x0)^p)		
Reduced Chi-Sqr	0.41289		
Adj. R-Square	0.98857		
		Value	Standard Error
	A1	-0.00266	0.00531
	A2	1.57389	1.49029
	x0	9485.20714	28178.27611
Delta R/Ri	p	0.50896	0.10581
	EC20	622.4902	1523.50756
	EC50	9485.20714	28178.27611
	EC80	144531.03775	506933.48796

n = 5 replicates per concentration

Healthy plant extract (Blank):
$\Delta R/R_i$ = -0.001 ± 0.008

LOD ≈ 5 nM SDE1 at 3*SD_{Blank}
($\Delta R/R_i$ = 0.023)

y-axis: $\Delta R/R_i$
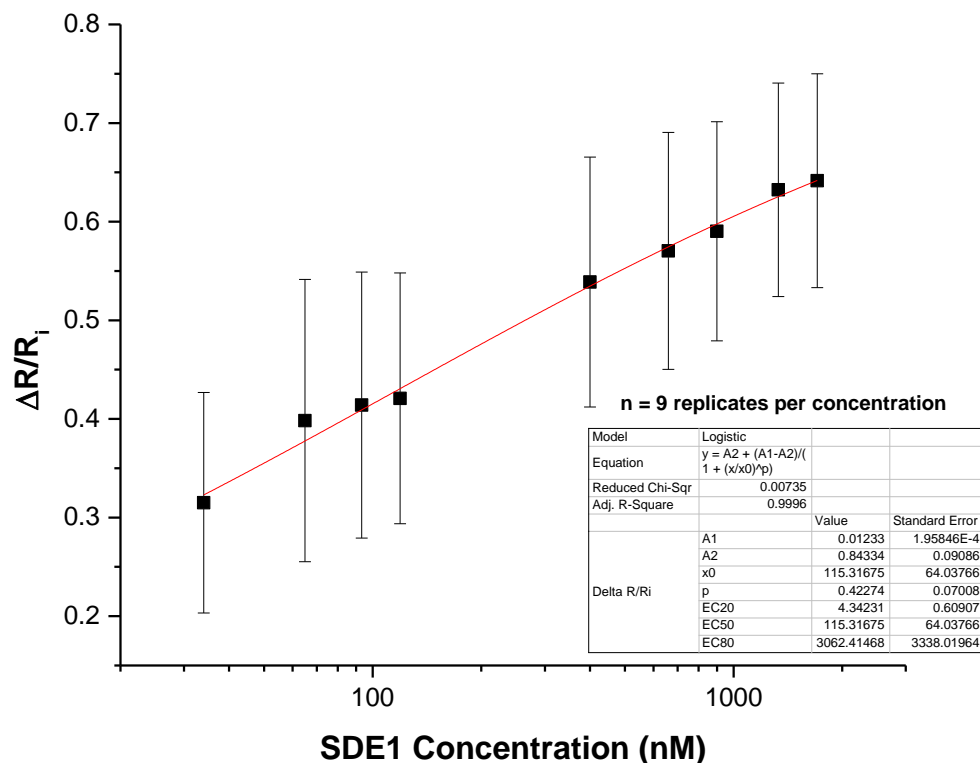
x-axis: **SDE1 Concentration (nM)**

Figure 5.9: Calibration plot of SDE1 proteins in 10 mM phosphate buffer, pH 7.4. Resistance changes were calculated using the equation $\frac{\Delta R}{R_i} = \frac{R_f - R_i}{R_i}$ where R_f is the equilibrated resistance after each addition, and R_i is the equilibrated resistance after device conditioning with healthy plant tissue extract. Data was fitted using 4-parameter logistic regression analysis. Data points represent the averaged normalized measurements from 5 (n = 5) SWNT biosensors. Error bars represent ±1 standard deviation.

| Solution Number	Concentration of the standard addition (nM)	$\Delta R/Ri$	Standard Deviation (n = 5)
1	0	0.032	0.006
2	10	0.050	0.009
3	20	0.062	0.010
4	40	0.085	0.021

Table 5.1: *Data for determining SDE1 concentration in simulated unknown sample by the standard-addition method. Sensor responses and standard deviation values were obtained from 5 individual sensors (n = 5).*

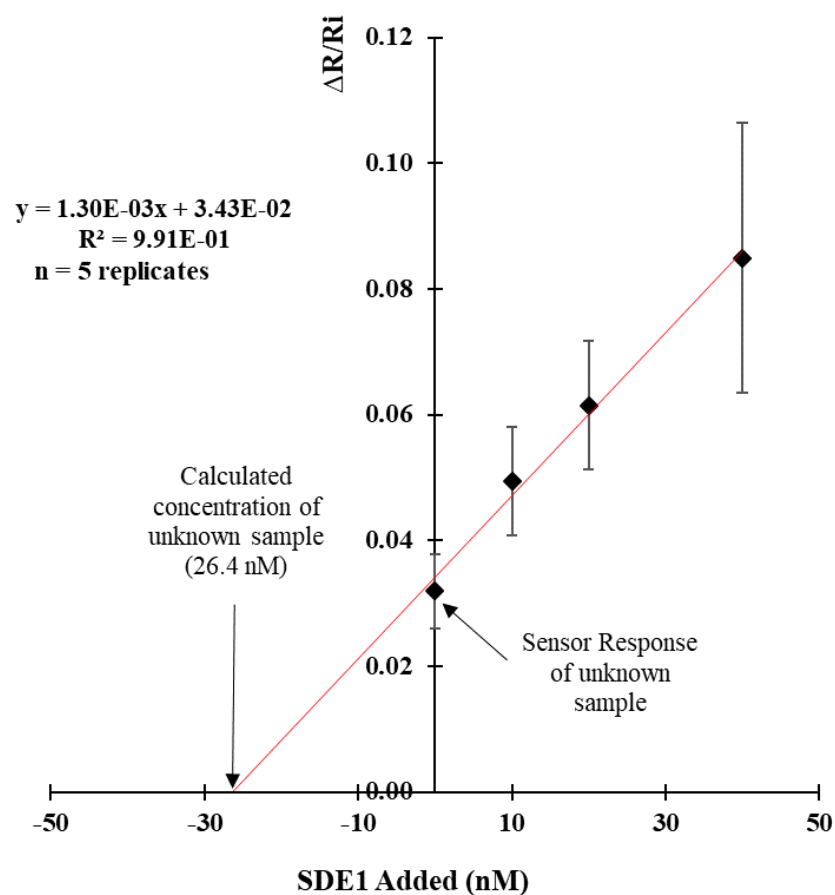**Figure 5.10**: *Determination of SDE1 concentration in simulated "unknown" plant extract sample, with theoretical concentration of 29.4 nM. Calculated SDE1 concentration of 26.4 nM is the absolute value of x-intercept of the fitted regression line in nanomolar. $\Delta R/R_i$ and error bars were obtained from 5 individual sensors at each concentration. Error bars represent one standard deviation.*

5.5 Conclusion

With the looming crisis caused by HLB disease on the multibillion dollar global citrus industry, it is imperative that disease management strategies address some of the challenges associated with accurate, timely, and robust detection and diagnosis of infection to curb the spread of the pathogen and disease[1–3]. By adopting a novel detection strategy based on the secreted protein biomarker, SDE1, we can overcome challenges faced by other detection methods, such as nucleic acid-based and symptom-based which have been found prone to false negatives and mis-diagnoses[3]. By combining the physical and chemical advantages of carbon nanomaterials like SWNTs with FET and chemiresistive biosensors technologies, we have demonstrated a label-free biosensor platform for the detection of HLB biomarkers. With the dynamic range over 3 orders of magnitude in the low nanomolar concentration range, the biosensor platform shows potential for further optimization for field application.

5.6 References

1.   Gottwald, T. R. Current Epidemiological Understanding of Citrus Huanglongbing
*. *Annual Review of Phytopathology* **48,** 119–139 (2010).

2.   Teixeira, D. C. *et al.* Distribution and quantification of Candidatus Liberibacter americanus, agent of huanglongbing disease of citrus in São Paulo State, Brasil, in leaves of an affected sweet orange tree as determined by PCR. *Molecular and Cellular Probes* **22,** 139–150 (2008).

3.   Pagliaccia, D. *et al.* A Pathogen Secreted Protein as a Detection Marker for Citrus Huanglongbing. *Frontiers in Microbiology* **8,** (2017).

4.   Bové, J. M. Huanglongbing: a destructive, newly-emerging, century-old disease of citrus. *Journal of plant pathology* 7–37 (2006).

5.   Irey, M. S., Gast, T. & Gottwald, T. R. Comparison of visual assessment and polymerase chain reaction assay testing to estimate the incidence of the Huanglongbing pathogen in commercial Florida citrus. in *Proc. Fla. State Hortic. Soc* **119,** 89–93 (2006).

6.   Liu, S. & Guo, X. Carbon nanomaterials field-effect-transistor-based biosensors. *NPG Asia Materials* **4,** e23 (2012).

7.   Balasubramanian, K. & Burghard, M. Biosensors based on carbon nanotubes. *Analytical and Bioanalytical Chemistry* **385,** 452–468 (2006).

8.   Thévenot, D. R., Toth, K., Durst, R. A. & Wilson, G. S. Electrochemical biosensors: recommended definitions and classification. *Biosensors and Bioelectronics* **16,** 121–131 (2001).

9.   Lee, C.-S., Kim, S. K. & Kim, M. Ion-Sensitive Field-Effect Transistor for Biological Sensing. *Sensors* **9,** 7111–7131 (2009).

10.   He, Q., Wu, S., Yin, Z. & Zhang, H. Graphene-based electronic sensors. *Chemical Science* **3,** 1764 (2012).

11.   Katz, H. Chemically Sensitive Field-Effect Transistors and Chemiresistors: New Materials and Device Structures. *Electroanalysis* **16,** 1837–1842 (2004).

12.   Tlili, C., Myung, N. V., Shetty, V. & Mulchandani, A. Label-free, chemiresistor immunosensor for stress biomarker cortisol in saliva. *Biosensors and Bioelectronics* **26,** 4382–4386 (2011).

13. Sarkar, A. & Daniels-Race, T. Electrophoretic Deposition of Carbon Nanotubes on 3-Amino-Propyl-Triethoxysilane (APTES) Surface Functionalized Silicon Substrates. *Nanomaterials (Basel)* **3,** 272–288 (2013).

14. Choi, K. H. *et al.* Controlled deposition of carbon nanotubes on a patterned substrate. *Surface Science* **462,** 195–202 (2000).

15. Liu, J. *et al.* Controlled deposition of individual single-walled carbon nanotubes on chemically functionalized templates. *Chemical Physics Letters* **303,** 125–129 (1999).

16. Iijima, S. Helical microtubules of graphitic carbon. *Nature* **354,** 56–58 (1991).

17. Watson, T. J. Carbon-based electronics. *Nature Nanotechnology* **2,** (2007).

18. Odom, T. W., Huang, J.-L., Kim, P. & Lieber, C. M. Atomic structure and electronic properties of single-walled carbon nanotubes. *Nature* **391,** 62–64 (1998).

19. Hu, P. *et al.* Carbon Nanostructure-Based Field-Effect Transistors for Label-Free Chemical/Biological Sensors. *Sensors* **10,** 5133–5159 (2010).

20. Tran, T.-T. & Mulchandani, A. Carbon nanotubes and graphene nano field-effect transistor-based biosensors. *TrAC Trends in Analytical Chemistry* **79,** 222–232 (2016).

21. Heller, I. *et al.* Identifying the Mechanism of Biosensing with Carbon Nanotube Transistors. *Nano Letters* **8,** 591–595 (2008).

22. Ohno, Y., Maehashi, K. & Matsumoto, K. Chemical and biological sensing applications based on graphene field-effect transistors. *Biosensors and Bioelectronics* **26,** 1727–1730 (2010).

23. Sun, Y.-P., Fu, K., Lin, Y. & Huang, W. Functionalized Carbon Nanotubes: Properties and Applications. *Accounts of Chemical Research* **35,** 1096–1104 (2002).

24. Banerjee, S., Hemraj-Benny, T. & Wong, S. S. Covalent Surface Chemistry of Single-Walled Carbon Nanotubes. *Advanced Materials* **17,** 17–29 (2005).

25. Georgakilas, V. *et al.* Functionalization of Graphene: Covalent and Non-Covalent Approaches, Derivatives and Applications. *Chemical Reviews* **112,** 6156–6214 (2012).

26. Ramnani, P., Saucedo, N. M. & Mulchandani, A. Carbon nanomaterial-based electrochemical biosensors for label-free sensing of environmental pollutants. *Chemosphere* (2015). doi:10.1016/j.chemosphere.2015.04.063

27. Ramnani, P., Gao, Y., Ozsoz, M. & Mulchandani, A. Electronic Detection of MicroRNA at Attomolar Level with High Specificity. *Analytical Chemistry* **85,** 8061–8064 (2013).

28. Wasik, D., Mulchandani, A. & Yates, M. V. Point-of-Use Nanobiosensor for Detection of Dengue Virus NS1 Antigen in Adult Aedes aegypti: A Potential Tool for Improved Dengue Surveillance. *Anal. Chem.* **90,** 679–684 (2018).

29. García-Aljaro, C. *et al.* Carbon nanotubes-based chemiresistive biosensors for detection of microorganisms. *Biosensors and Bioelectronics* **26,** 1437–1441 (2010).

30. O'Connell, M. A., Belanger, B. A. & Haaland, P. D. Calibration and assay development using the four-parameter logistic model. *Chemometrics and Intelligent Laboratory Systems* **20,** 97–114 (1993).

31. Findlay, J. W. A. & Dillard, R. F. Appropriate calibration curve fitting in ligand binding assays. *AAPS J* **9,** E260–E267 (2007).

32. Fakanya, W., Tothill, I., Fakanya, W. M. & Tothill, I. E. Detection of the Inflammation Biomarker C-Reactive Protein in Serum Samples: Towards an Optimal Biosensor Formula. *Biosensors* **4,** 340–357 (2014).

33. Harris, D. C. Quantitative Chemical Analysis. 828

34. Ellison, S. L. R. & Thompson, M. Standard additions: myth and reality. *Analyst* **133,** 992 (2008).

35. Andersen, J. E. T. The standard addition method revisited. *TrAC Trends in Analytical Chemistry* **89,** 21–33 (2017).

36. Chen, Z., Appenzeller, J., Knoch, J., Lin, Y. & Avouris, P. The Role of Metal−Nanotube Contact in the Performance of Carbon Nanotube Field-Effect Transistors. *Nano Letters* **5,** 1497–1502 (2005).

37. Byon, H. R. & Choi, H. C. Network Single-Walled Carbon Nanotube-Field Effect Transistors (SWNT-FETs) with Increased Schottky Contact Area for Highly Sensitive Biosensor Applications. *Journal of the American Chemical Society* **128,** 2188–2189 (2006).

38. Ohno, Y., Maehashi, K. & Matsumoto, K. Graphene Biosensor. in *Frontiers of Graphene and Carbon Nanotubes* (ed. Matsumoto, K.) 91–103 (Springer Japan, 2015).

Chapter 6

Conclusion

6.1 Summary

The goal of my work was to develop a quantitative carbon nanomaterial-based chemiresitive/FET-based biosensor for detection of a secretory protein biomarker, SDE1, a novel biomarker for citrus greening disease or Huanglongbing (HLB) disease. Working on a project to develop affinity-based detection methods for a novel biomarker presented several challenges, one of which was the lack of commercially available bioreceptors specific to the newly discovered biomarker. Therefore, one prerequisite for this research was to procure and characterize the quintessential anti-SDE1 antibodies for SDE1 biomarker. In concert with the Ma Lab, we satisfied this prerequisite as described in Chapter 3, where we generated polyclonal antibodies specific to SDE1 biomarkers by immunization of rabbits, affinity-purified the anti-SDE1 antibodies, and evaluated their performances using a high-throughput assay method called enzyme-linked immunosorbent assays (ELISAs). The antibody has been used in various other immunoassay formats such as Western blots and direct tissue imprint assay as recently co-published by our collaborator[1]. Consequently, in developing and optimizing the ELISAs for evaluation of our antibodies, we also conveniently arrived at a potential high-throughput laboratory-based ELISA platform for SDE1 detection in plant samples. Using on a limited number of real infected plant samples and negative control samples provided by our collaborator, we demonstrated the feasibility for this antibody-based detection strategy for *C*Las infected plants in Chapter 3.

After procuring the anti-SDE1 antibodies, we proceeded to integrate the bioreceptor onto electrical biosensors that used the novel semiconducting carbon nanomaterials, reduced graphene oxide (RGO) and single-walled carbon nanotubes (SWNTs), as sensitive electrical transducers. The specific electrical biosensor format that this work focused on was based on a chemiresistor-type architecture, a two-electrode system that operates on sensing principles borrowed from traditional three-electrode field-effect transistor (FET) systems. Omitting the third gate electrode, modulation of electrical characteristics (e.g. conductance or resistance) of a chemiresistor-type device occurs by the same mechanisms as in traditional FET-based biosensors with the external gating solely by the charged molecules near the interface of the semiconducting channel[2,3]. While reviewing FET-based and chemiresistor-based biosensors, I was able to compile a review paper on the topic as shown in Chapter 2. In Chapter 4, we demonstrated detection of SDE1 in phosphate buffer using an RGO-based chemiresistive biosensor functionalized with anti-SDE1 antibodies. In Chapter 5, we investigated SWNTs as an alternative transducer material for a chemiresistive biosensor. Once again, using the anti-SDE1 antibody as the receptor molecule functionalized on the SWNT channel, we demonstrated detection of SDE1 HLB biomarkers in simple phosphate buffer and in complex plant tissue extracts.

6.2 Suggestions for Future Work

For the SDE1 biomarker to be useful as a true biomarker for HLB disease diagnosis, further efforts for biomarker validation is needed. One important aspect of biomarker validation is to develop a systematic and reliable method for sample acquisition and

characterization. Also, to facilitate more reproducible immunoassay and biosensor for future development, we need to transition away from polyclonal antibodies, and instead invest efforts to generate higher affinity monoclonal antibodies, possibly through mouse hybridomas or phage-display techniques.

While the biosensors developed here showed promise, additional device characterization and mechanistic study is needed to further understand the sensing mechanism(s). Additionally, large-scale sensor fabrication process should be investigated and optimized to reduce inter-device variability. By reducing variability, we can achieve higher performing biosensor platforms with higher sensitivity. I would like to investigate other electrical biosensor designs and geometries to tune the biosensor performance to obtain more robust devices. For field-deployable applications, a reliable measurement system is required for mobile chemiresistive and/or FET measurements.

6.3 References

1.   Pagliaccia, D. *et al.* A Pathogen Secreted Protein as a Detection Marker for Citrus Huanglongbing. *Frontiers in Microbiology* **8,** (2017).

2.   He, Q., Wu, S., Yin, Z. & Zhang, H. Graphene-based electronic sensors. *Chemical Science* **3,** 1764 (2012).

3.   Katz, H. Chemically Sensitive Field-Effect Transistors and Chemiresistors: New Materials and Device Structures. *Electroanalysis* **16,** 1837–1842 (2004).